

<https://doi.org/10.15388/vu.thesis.600>

<https://orcid.org/0000-0003-1596-0664>

VILNIUS UNIVERSITY

CENTER FOR PHYSICAL SCIENCES AND TECHNOLOGY

Matas Rudzikas

Investigation of Optical and Electrical Characteristics in Photovoltaic Devices Colored by the Functional Metal Oxide Coatings

DOCTORAL DISSERTATION

Natural Sciences,
Physics (N 002)

VILNIUS 2024

The dissertation was prepared between 2017 and 2024 at the Center for Physical Sciences and Technology (FTMC).

Academic supervisor – Dr. Arūnas Šetkus (Center For Physical Sciences And Technology, Natural sciences, Physics, N 002).

Dissertation Defense Panel:

Chairman – Prof. Habil. Dr. Vidmantas Gulbinas (Center For Physical Sciences And Technology, Natural Sciences, Physics, N 002).

Members:

Dr. Maxim Guc (Catalonia Institute for Energy Research, Natural Sciences, Physics, N 002),

Prof. Dr. Vygintas Jankauskas (Vilnius University, Technological Sciences, Material Engineering, T 008),

Dr. Vincas Tamošiūnas (Vilnius University, Technological Sciences, Material Engineering, T 008),

Prof. Dr. Pranciškus Vita (Vilnius University Natural Sciences, Physics, N 002).

The dissertation shall be defended at a public meeting of the Dissertation Defense Panel at 10:00 (hour)/ on 29th of May 2024 in A101 auditorium (Center for Physical Sciences and Technology). Address: Saulėtekis av. 3, Vilnius, Lithuania. Tel. +37061592859; e-mail: matas.rudzikas@gmail.com

The text of this dissertation can be accessed at the libraries of the Center for Physical Sciences and Technology and Vilnius University, as well as on the website of Vilnius University:

www.vu.lt/lt/naujienos/ivykiu-kalendorius

<https://doi.org/10.15388/vu.thesis.600>

<https://orcid.org/0000-0003-1596-0664>

VILNIAUS UNIVERSITETAS
FIZINIŲ IR TECHNOLOGIJOS MOKSLŲ CENTRAS

Matas Rudzikas

Optinių ir elektrinių charakteristikų
tyrimas fotovoltiniuose elementuose,
nuspaltvuose funkcinėmis skaidrių
oksidų dangomis

DAKTARO DISERTACIJA

Gamtos mokslai,
Fizika (N 002)

VILNIUS 2024

Disertacija rengta 2017–2024 metais VMTI Fizinių ir technologijos mokslų centre.

Mokslinis vadovas – dr. Arūnas Šetkus (Fizinių ir technologijos mokslų centras, gamtos mokslai, fizika, N 002).

Gynimo taryba:

Pirmininkas – Prof. habil. dr. Vidmantas Gulbinas (Fizinių ir technologijos mokslų centras, gamtos mokslai, fizika, N 002).

Nariai:

Dr. Maxim Guc (Katalonijos energetikos tyrimų institutas, gamtos mokslai, fizika, N 002);

Prof. dr. Vygintas Jankauskas (Vilniaus universitetas, technologijos mokslai, medžiagų inžinerija, T 008);

Dr. Vincas Tamošiūnas (Vilniaus universitetas, technologijos mokslai, medžiagų inžinerija, T 008);

Prof. dr. Pranciškus Vita (Vilniaus universitetas, gamtos mokslai, fizika, N 002);

Disertacija ginama viešame Gynimo tarybos posėdyje 2024 m. gegužės mėn. 29 d. 10:00 val. (Fizinių ir technologijos mokslų centre) A101 auditorijoje. Adresas: Saulėtekio al. 3, Vilnius, Lietuva, tel. +37061592859; el. paštas: matas.rudzikas@gmail.com.

Disertaciją galima peržiūrėti Fizinių ir technologijos mokslų centro, Vilniaus universiteto bibliotekose ir VU interneto svetainėje adresu:

www.vu.lt/lt/naujienos/ivykiu-kalendorius.

PADĖKA

Pirmiausia noriu padėkoti darbo vadovui Arūnui Šetkui už didelę kantrybę, motyvaciją, skirtą laiką, bei pastangas siekiant išmokyti mane būti geresniu fiziku bei mokslininku.

Dėkui Aleksandrui G. Uliašinui už idėjas, motyvaciją ir kitokią pagalbą atliekant tyrimus su dvigubomis antiefleksinėmis dangomis bei ruošiant pirmąją publikaciją.

Ačiū chemikei Jolantai Donėlienei už pagalbą aiškinantis cheminius, bei fizikinius procesus vykstančius zolių gelių tirpaluose, jų formavimo ir dengimo metu.

Galiausiai noriu padėkoti tėvams, draugams ir merginai Gabrielei už palaikymą, kantrybę ir tikėjimą šiame gana netrumpame ir nelengvame, tačiau įdomiame bei padėjusiame augti gyvenimo etape.

TABLE OF CONTENTS

1. INTRODUCTION.....	11
1.1 Objectives and tasks	15
1.2 Scientific novelty.....	16
1.3 Author’s contribution	17
1.4 Dissertation structure.....	18
1.5 Author’s publication list.....	20
1.6 Defensive statements	22
2. LITERATURE REVIEW	23
2.1 Anti-reflective coatings	23
2.2 Sol-gel solution theory (for Bragg reflector structures)	24
2.3 Dip coating deposition technique	26
2.6 Colorimetry	30
3. METHODOLOGIES USED IN THE RESEARCH.....	34
3.1 Transfer matrix method (for 1D optical simulations).....	34
3.2 SCAPS software (for 1D electrical simulations).....	36
3.3 PV lighthouse simulation tool (for 1D optical simulations).....	36
3.4 Calculation of Maximum Possible J_{sc} and J_{sc} Loss (for tandem simulations):	37
3.5 Calculation of carrier generation profile (for tandem simulations)	37
3.6 Sample characterization methods	38
4. FUNCTIONAL METAL OXIDE COATINGS FOR THE FORMATION OF DOUBLE LAYER ANTI-REFLECTIVE COATINGS ON PHOTOVOLTAIC STRUCTURES – THE EFFECT OF THICKNESS	43
4.1 Simulation model (for ITO/SiN _x :H DLARCs).....	43
4.2 Simulation: anti-reflective coating thickness on color (for ITO/SiN _x :H DLARCs)	44
4.3 Sample preparation (magnetron sputtering)	45
4.4 Experimental realization of ITO/SiN _x :H DLARCs	46
4.5 Solar module made using solar cells with ITO/SiN _x :H DLARC	48

4.6 Colorimetric analysis of ITO/SiN _x :H DLARCs	49
4.7 Summary	52
5. FUNCTIONAL METAL OXIDE COATINGS FOR THE FORMATION OF DOUBLE LAYER ANTI-REFLECTIVE COATINGS ON PHOTOVOLTAIC STRUCTURES – THE EFFECT OF REFRACTIVE INDEX	53
5.1 Simulation details (for ITO/SiN _x :H DLARCs)	53
5.2 Simulation results (for ITO/SiN _x :H DLARCs)	54
5.3 Colorimetric analysis (for ITO/SiN _x :H DLARCs)	55
5.3 Summary (for ITO/SiN _x :H DLARCs).....	58
6. FUNCTIONAL METAL OXIDE COATINGS FOR THE FORMATION OF BRAGG REFLECTOR STRUCTURES FOR PHOTOVOLTAIC CELLS	60
6.1 Simulation model	60
6.2 Simulation results	62
6.3 Sample production.....	63
6.4 Experimental realization of Bragg reflector structure	64
6.5 Feasibility of the technology for mini-PV panels.....	66
6.7 Sensitivity of color to the deviations in refractive index and thickness .	70
6.8 Scalability of the technology	72
6.9 Summary	73
7. FUNCTIONAL COATINGS FOR COLORING OF TANDEM CELLS: DIGITAL MODEL CALCULATIONS	75
7.1 Simulation methodology	75
7.2 Setting the tandem cell simulation parameters	77
7.3 Monolithic Kesterite/Silicon tandem optimization (in brief)	80
7.4 Sensitivity of tandem solar cell electrical characteristics to the variation of Al ₂ O ₃ anti-reflective coating thickness.....	83
7.5 Colorimetry and tandem viability for BIPV	84
7.6 Summary	86
8. SANTRAUKA	88

8.1 Įžanga	88
8.2 Funkciniai skaidrūs oksidai dviguboms anti-atspindinčioms dangoms fotovoltinėse struktūrose formuoti – sluoksnio storio įtaka	92
8.2.2 Bandinių ruošimas (magnetroninis dulkinimas).....	94
8.2.3 Bandiniai su dvigubomis ITO/SiN _x :H antirefleksinėmis dangomis....	94
8.2.4 Technologijos su dvigubomis ITO/SiN _x :H antirefleksinėmis dangomis tinkamumas saulės moduliams	95
8.3 Funkciniai skaidrūs oksidai dviguboms anti-atspindinčioms dangoms fotovoltinėse struktūrose formuoti – sluoksnio lūžio rodiklio įtaka.....	99
8.3.1 Optiniai modeliavimai (for ITO/SiN _x :H DLARCs)	99
8.3.2 Kolorimetrinė analizė (dviguboms antirefleksinėms dangoms su ITO/SiN _x :H)	100
8.3.3 Skyriaus apibendrinimas	103
8.4 Funkciniai skaidrūs oksidai Bragg reflektorių struktūroms fotovoltiniams saulės elementams formuoti	104
8.4.1 Modeliavimo metodika.....	104
8.4.2 Simuliacijos rezultatai	105
8.4.3 Bandinių ruošimas.....	106
8.4.4 Eksperimentinis fotovoltinių struktūrų su Bragg reflektoriais realizavimas.....	107
8.4.6 Spalvos jautrumas funkcinių oksidų lūžio rodiklio ir storio nuokrypiams	110
8.4.7 Apibendrinimas	112
8.5 Funkciniai skaidrūs oksidai tandeminiams saulės elementams spalvoti: skaitmeniniai modeliavimai	112
8.5.1 Modeliavimo metodika.....	113
8.5.2 Tandeminio saulės elemento elektrinių charakteristikų jautrumas antirefleksinės Al ₂ O ₃ dangos storio kitimui	113
8.5.3 Kolorimetrinė analizė ir tinkamumas į pastatus integruotai fotovoltikai	114
8.5.4 Apibendrinimas	115
9. CV OF THE DISSERTATION CANDIDATE.....	117

10. BIBLIOGRAPHY 119

NOMENCLATURE

1D	one dimensional
3D	three-dimensional
ARC	anti-reflective coating
BIPV	building integrated photovoltaics
CB	conduction band
CIE	the International Commission on Illumination
CRM	critical raw materials
CV	valence band
DBR	distributed Bragg reflector
DLARC	double layer anti-reflective coating
E-beam	electron beam
eDOS	Effective density of states
EVA	ethylene vinyl acetate
FWHM	full width at half maxima
ITO	indium doped tin oxide
PECVD	plasma enhanced chemical vapor deposition
PERC	passivated emitter and rear contact
PV	photovoltaic
PVD	physical vapor deposition
REF	reference
RGB	red, green and blue
sRGB	standard RGB
RF	radio frequency
SEM	scanning electron microscopy
SLARC	single layer anti-reflective coating
SRH	Schockley-Read-Hall (recombination)
TBOT	titanium butoxide (precursor)
TEOS	tetraethyl orthosilicate (precursor)
TMM	the transfer matrix method

1. INTRODUCTION

A photovoltaic (PV) solar cell is a device converting electromagnetic radiation coming from the Sun into electricity. Nowadays, solar energy is one of the fastest growing renewable energy sources [1]. Importantly, this field holds huge potential in fighting against climate change or addressing humanity's increasing energy demand, as it can provide more energy than we need. According to the estimation made by M. Perez and R. Perez, in the next 30 years solar energy potential is 8300 Terawatt-years (TWyr/y) (authors assumed energy conversion efficiency of 20% and realistic use of area), while consumption needed would be around 660 TWyr/y, what is about 12 times less [2].

Despite projections indicating potential growth, current PV share from global energy consumption remains at only around 2% [1] (data from 2022). One prospective market for PV applications is building-integrated photovoltaics (BIPV). It has such advantages as having an energy source closer to the user, reducing energy transmission costs, excluding the need for additional area, and implementing (nearly) zero-energy buildings. However, the expansion of this market faces limitations due to the predominant aesthetical appearance of PV solar cells available in the market, which are commonly blue or black. Consequently, there is a growing demand for colored PV products to harmonize with the colors of old towns, various building elements, or to realize other architectural ideas.

The report from PV sites identifies five crucial characteristics for BIPV: (1) low cost, (2) aesthetics, (3) long lifetime, (4) product flexibility, and (5) high efficiency [26]. Therefore, in further literature analysis, focus will be put on these aspects (if published works contain such information).

The visual appearance of a photovoltaic device depends on its reflectance spectra. The properties of such spectra can be relatively easily altered by adjusting the thickness of a single anti-reflective coating (SLARC) of the solar cell. For Silicon solar cells, which cover around 92-95% of whole PV market [3], this is usually a layer of hydrogenated silicon nitride ($\text{SiN}_x\text{:H}$) deposited on the top of silicon by plasma enhanced chemical vapor deposition (PECVD) [4]. Historically, the primary focus of commercial PV has been on efficiency and longevity. Consequently, the optimization of the anti-reflective coating thickness aimed at performance has resulted in a blue or black color. Nevertheless, this color alteration holds the potential to yield almost any other color. The variation of SLARC thickness is considered one of the simplest approaches to color modification and potentially can be cheap, as existing manufacturing equipment can be used [5]. However, as it interferes with

manufacturing process, laser ablation needs to be adjusted for ablating $\text{SiN}_x\text{:H}$ with different thicknesses, while maintaining its passivating properties [6–8]. A more sophisticated coloring approach is deposition of additional metal oxide forming a double layer anti-reflective coating (DLARC) on the commercial solar cell, leaving the cell production process intact [9,10]. The use of DLARC only requires layer optimization for light trapping properties, without the need to be optimized for passivation [4]. Besides, this way also the yield can be enhanced, as utilization of double or triple anti-reflective coatings can be more efficient [6,7]. Y. Chen carried out a research for the solar cells with $\text{MgF}_2/\text{SiN}_x\text{:H}$, $\text{SiO}_2/\text{SiN}_x\text{:H}$ and $\text{Al}_2\text{O}_3/\text{SiN}_x\text{:H}$ DLARCs [8]. Authors concluded that DLARC is more flexible to modulate colors compared to SLARC while still guaranteeing good passivation quality without significant optical generation loss. Moreover, Minghua Li et. al reported experimental results for multi-crystalline solar cells with $\text{SiO}_2/\text{SiN}_x\text{:H}$ DLARC [9]. Researchers obtained 4 different colors with different SiO_2 thicknesses of 84 (greyish yellow), 136 (purple), 190 (deep blue), 220 (green) nm using e-beam evaporation technique. Resulting relative change in efficiency was +0.6, -0.7, -4.5 and -2.6%. However, authors also stated that the SiO_2 layer is not the best choice for DLARC cells because its refractive index is very similar to ethylene vinyl acetate (EVA) ($n \approx 1.5$) that is mostly used for the module encapsulation in the PV industry [11]. Therefore, the effect shown in the work could be neglected after lamination. Same team one year later reported more detailed theoretical analysis with employing SiO_xN_y instead of SiO_2 to mitigate the mentioned drawback of their previous work [10]. In this approach, the $\text{SiN}_x\text{:H}$ (the refractive index $n = 2.05$ and the thickness $d = 80$ nm) was covered with a varying thickness of the SiO_xN_y film ($n = 1.8$). The resulting cells have no additional current density improvement with increasing SiO_xN_y thickness, but obtained colors were quite similar to the case of SLARC.

Even more elaborate solution could be realized using multilayer coatings called distributed Bragg reflectors (DBRs) [12]. These structures consist of periodic stacks of high and low refractive index material and can be finely tuned to exhibit high reflectance within a selected wavelength interval, while having low reflectance outside its range [13]. Similarly, the intentional selection of the structure parameters allows the desired color effects of the reflected light to be obtained. Due to these reasons, DBR coloring can be considered a more flexible method, compared to previously described SLARCs and DLARCs. Besides, it is worth noting that, in cases like this, efficiency loss is inevitable, as the reflection peak maxima increases (in most cases) compared to anti-reflective coatings (ARCs), resulting in higher loss

but improved aesthetical properties. B. Bläsi et al. demonstrated that quite homogeneous and bright colors on large surface area of 1 m² size textured glass could be achieved with energy loss less than 6% [14]. In their study researchers utilized 7 TiO₂/SiO₂ layers (4 high refractive index, 3 low refractive index) deposited with PVD lab coater. Similarly, A. Soman et al. employed Silicon Nitride and Silicon oxynitride bilayer stacks [15]. Coatings were applied on the top of the commercial solar cell of 5x5 cm using radio frequency plasma enhanced chemical vapor deposition (PECVD). Resulting efficiency loss ranged from 19 to 41% compared to reference case of commercial solar cell with blue color. Notably, researchers even produced a white coating, what is challenging due to the requirement to obtain flat reflectance spectra. Another article published by group represented by Z. Xu et al. used 5 bilayers of TiO₂ and SiO₂ deposited on glass with magnetron sputtering technique [16]. The loss in efficiency was from 16.3 to 28.4% (relative), depending on the color. However, all these implementations of DBR technology were realized on expensive magnetron sputtering or chemical vapor deposition (CVD) technologies.

Some other coloring solutions include: mica pigment [17], plasmonic coatings [18], quantum dot solar cells [19], liquid crystals [20]), semitransparent solar cells [21,22].

This implies that, despite the existence of various coloring techniques, there is still room for improvement, particularly in terms of cost efficiency, scalability, and commercial viability. Certain technologies described above employ expensive deposition techniques [14–16], some of them experience high efficiency losses [15,16], have limited coloring possibilities [17,18], or experience low homogeneity [18] Meanwhile, other technologies have presented results in the early stages on small sizes [19,23] or face challenges in scalability [22]. This work addresses and proposes improvements to these issues (or some of them), as elaborated in subsequent paragraphs.

Therefore, the aim of this work was to explore cost-effective methodologies for modification of solar cell color by applying functional metal oxides and employing combined simulations with experiments while using commercial solar cells as a baseline.

As a first step of this work, simple interference-based colorization of Si based solar cells and panels employing ITO/SiN_x:H double layer antireflective coatings was analyzed by means of simulations and then realized experimentally. Indium Tin Oxide (ITO) emerges as a promising candidate for such a layer owing to its stability and ease of modification of its refractive index through stoichiometry and adjustments in film crystalline structure [24]. Furthermore, with high electrical conductivity, ITO becomes highly appealing

for the formation of a DLARC as it holds the potential to not only reduce resistance loss in the contacts but also facilitate busbar soldering after the deposition of ITO. What is more, ITO deposition is used in the glass industry for large area deposition of the IR reflection, EMC shielding or other electro-optical coatings, thus could be easily adapted for solar cell coloring.

As a second step of this work, a more elaborate solution is proposed using distributed Bragg reflectors. This approach offers distinct advantages over colored solar cells with double-layer anti-reflective coatings (DLARCs). Notably, coatings applied to a glass substrate enable the entire surface to be colored, extending beyond individual solar cells. Besides, color brightness could be expected to be higher in such structures, as tuning of DBRs allow to obtain higher reflection peaks compared to SLARCs [25]. Unlike in the published articles employing this technology, in this work structure is optimized for lower number of periods of high and low refractive layer stacks and experimentally realized with sol-gel solutions deposited using dip coating technique. The sol-gel technique holds potential advantages in terms of cost-effectiveness and scalability when compared to the costly vacuum-based deposition technologies. This work also involves a more detailed colorimetric analysis (compared to other works) and evaluation of sensitivity of color to the deviations in characteristic parameters (refractive index and thickness) from the optimal case of Bragg's condition.

The final part of this work was dedicated to coloring of tandem solar cells, what was absent in the literature. Some additional reasons are detailed in the further text.

A noticeable increase of interest of research groups and industry in tandem solar cells can be observed [26]. Such increase is especially accelerated by the fast approach of silicon commercial solar cells towards their maximum efficiency. Currently, such efficiencies in industry are already around 25-26%, with the average being at 24% [11]. While Shockley-Queisser limit for silicon is around 32% [27], and practical limit is just above 27%, considering factors such as extrinsic recombination loss, optical loss, and resistive loss [28]. This is only 1-2% away from the current maximum industrial efficiencies. Hence, similarly as for the single junction solar cells there will be increasing need for colored tandem cells in such markets as building integrated photovoltaics (BIPV) [29–31].

While currently the highest obtained silicon based tandem efficiency belongs to perovskite/silicon, achieving 33.9% at a small scale ($\sim 1 \text{ cm}^2$) and 28.6% ($\sim 258 \text{ cm}^2$) at a larger scale [32], perovskites still face stability issues [33]. Another promising technology is based on the kieserite family of compounds. These materials offer notable advantages, as they exhibit

excellent stability and do not rely on critical raw materials (CRM) as defined by the European Commission [34]. When used in photovoltaics, these materials are also called kesterites, because of the name of their (desired) crystalline structure. Kesterite material is a quaternary compound having a similar structure to commercial $\text{Cu}(\text{In,Ga})(\text{S,Se})_2$ (CIGSSe) technology, where two indium or gallium atoms are replaced with one tin and one zinc atom resulting in $\text{Cu}_2\text{ZnSn}(\text{S,Se})_4$ [35]. Moreover, their band gap can be precisely tailored by alloying with anionic substitutions of Se or S or cationic substitutions of Si, Ge, and Sn within a range from 0.88 to 2.22 eV.

Yet, colored solutions are not published for tandem solar cells to our knowledge. This suggested simulating kesterite/silicon tandem solar cells with an idea to evaluate their colorimetric properties as it is becoming more and more relevant. For this, pure germanium kesterite $\text{Cu}_2\text{ZnGe}(\text{S,Se})_4$ was employed. Its refractive index spectra were incorporated with a band gap ranging from 1.52 to 2.02 eV via sulfur/selenium alloying ($\text{Cu}_2\text{ZnGe}(\text{S}_x\text{Se}_{1-x})_4$ or CZGSSe) [36] to determine the optimal kesterite thickness and a bandgap, what was absent or not fully realized in prior research. To explore the impact of individual modifications, a stepwise approach was adopted to improve the kesterite structure. Finally, evaluation of colorimetric properties for the tandem device by varying Al_2O_3 anti-reflective coating thickness was demonstrated.

1.1 Objectives and tasks

1.1.1 Objectives

Explore cost-effective methodologies for modification of solar cell color by applying functional metal oxides, employing combined simulations with experiments while using commercial solar cells as a baseline.

1.1.2 Tasks

1. Theoretical analysis and experimental implementation of functional coatings to be made by incorporating ITO on the top of commercial silicon solar cells to create double-layer anti-reflective coatings (DLARC). This involves investigating the impact of two critical parameters – thickness and refractive index – on the optical and electrical characteristics of solar cells, with a particular emphasis on the color aspect. Additionally, assessing the viability and acceptability of the proposed technology for integration into solar panels.
2. Exploring the optimal design of functional metal oxide coatings to create a Bragg reflector structure intended for application in photovoltaics (PV).

Then, experimentally realizing the optimized structure on glass substrates using the sol-gel dip coating technique and thoroughly characterizing its optical (including color) and electrical properties. Subsequently, demonstrating its suitability for integration into PV panels and performing a comparative analysis of its characteristics. Finally, investigating the sensitivity of color characteristics to deviations in refractive index and thickness from the optimal case of Bragg's condition.

3. Investigating the potential of two-terminal tandem solar cells with silicon as the bottom sub-cell through simulations. Analyzing the coloring possibilities of these devices and assessing their impact on the electrical properties of the structure. Comparing these characteristics with characteristics obtained using coloring methods described in 2 previous tasks and evaluating its viability for building-integrated photovoltaics (BIPV).

1.2 Scientific novelty

Our group was first for using ITO as a part of double anti-reflective coating formed by the deposition of this oxide on the top of commercial silicon solar cell. Using simulations the effect of refractive index of DLARC on optical characteristics and color was first time analyzed. Novel solar cells were made using magnetron sputtering technique with varying ITO thicknesses. Then such cells were employed for producing PV mini modules, what was not present in prior research. Finally, a much more detailed colorimetric analysis was performed emphasizing comparison between laminated and non-laminated solar cells.

In the next part of the work, an innovative Bragg reflector structure is presented, which was optimized for lower and uneven number of high and low refractive index material stacks compared to the other works. Using simulations, it was proved that uneven and even numbered metal oxide structures have similar characteristics and therefore a simpler solution was favored for easier experimental realization. First time, this structure was experimentally realized for PV using a potentially cheap sol-gel dipping technique. Besides, in this work a more detailed colorimetric analysis was performed and Bragg reflector technology was compared to other coloring technologies using characteristic parameters from CIE color space: xyY and color purity parameter. Finally, a sensitivity of color to refractive index and thickness deviations from the optimal case of Bragg's condition was presented, what was absent in the prior works.

In the third part of the work, first time coloring of a two terminal tandem solar cell was analyzed using simulation employing kesterite as a top sub-cell and silicon as a bottom sub-cell. In the first part of this section partial optimization of kesterite sub cell was performed. For this, a wider range kesterite refractive index spectra were incorporated with a band gap from 1.52 to 2.02 eV via sulfur/selenium alloying ($\text{Cu}_2\text{ZnGe}(\text{S}_x\text{Se}_{1-x})_4$ or CZGSSe) [36] to determine the optimal kesterite thickness and a bandgap, compared to a maximum of 1.6 eV band gap employed in previous works [35]. Besides, a state of the art PERC silicon solar cell with 24% of efficiency was used as a bottom device [4], while most of other works used older silicon devices [38,39]. Finally, the coloring of such tandem structure was investigated by the variation of thickness of functional metal oxide coating of Al_2O_3 from 0 to 300 nm and its effect on optical and electrical characteristics of the PV device. Also, characteristic colorimetric parameters were compared with other coloring techniques and viability to be used in building integrated photovoltaics analyzed.

1.3 Author's contribution

Abstract contributions are detailed according to Contributor Roles Taxonomy [40].

Most of the work was done by the author of this work: conceptualization, methodology (measurements: spectrometer, profilometer, solar simulators), software (simulations using OPAL 2 by PV Lighthouse [41], simulations using transfer matrix method implemented with c++ and python programming languages, simulations using SCAPS, script for merging two J-V curves of both sub-cells for tandem simulations, calculation of calorimetric data using Bentwin+ software by Bentham, setting simulation parameters for tandem simulations using REF cells, optimization of kesterite/silicon tandem), validation, formal analysis (colorimetric analysis, optical and electrical solar cell characteristic data analysis), investigation (overall experiment planning, sample preparation and cleaning, laser cutting of multi-crystalline solar cells, solar cell soldering/lamination, sol-gel solution preparation, dipping experiments, sample annealings), resources (most of recourses planned and provided), data curation (selection of simulation data from the literature: refractive indexes, work functions, doping etc.), writing—original draft preparation (most of the writing for all of the published articles and solely for thesis), writing—review and editing (most of the writing for all of the published articles and solely for thesis), visualization (almost all of the figures and schemes, except several detailed in the work).

Ellipsometry measurements were performed, and refractive index spectra computed by Ernesta Bužavaitė-Vertelienė and Zigmās Balevičius (TiO₂, SiO₂ and glass).

SEM measurements were done by Cedric Leuvre from Institut de Physique et de Chimie des Matériaux de Strasbourg (UMR CNRS) during a 1-month secondment in the latter institution.

Alexander Ulyashin from SINTEF (Oslo) was the author of the idea to use ITO for double layer anti-reflective coatings on commercial solar cells. He helped a lot with preparing the first article: conceptualization, planning the experiment, analysis of the results, editing, validation, supervision.

Marit Stange from SINTEF (Oslo) was helping me to do magnetron sputtering of ITO layers with different sputtering durations. Depositions were done at SINTEF during a 1-month secondment there.

Juras Ulbikas was the author of the initial idea to use Bragg reflectors for solar cell coloring. Also responsible for receiving funding for some projects related to this work.

Jolanta Donėlienė helped me working on coloring based on Bragg reflectors: preparing sol-gel solutions, dip coating, investigation, writing – review and editing. However, most of the work was done by the author of this thesis.

Arūnas Šetkus (supervisor) helped with most parts of the work: conceptualization, planning of the experiments, methodology, validation, investigation, supervision, review and editing, formal analysis.

1.4 Dissertation structure

Dissertation is divided into 7 chapters:

1. INTRODUCTION,
2. LITERATURE REVIEW,
3. METHODOLOGIES USED IN THE RESEARCH,
4. FUNCTIONAL METAL OXIDE COATINGS FOR THE FORMATION OF DOUBLE LAYER ANTI-REFLECTIVE COATINGS ON PHOTOVOLTAIC STRUCTURES – THE EFFECT OF THICKNESS,
5. FUNCTIONAL METAL OXIDE COATINGS FOR THE FORMATION OF DOUBLE LAYER ANTI-REFLECTIVE COATINGS ON PHOTOVOLTAIC STRUCTURES – THE EFFECT OF REFRACTIVE INDEX,
6. FUNCTIONAL METAL OXIDE COATINGS FOR THE FORMATION OF BRAGG REFLECTOR STRUCTURES FOR PHOTOVOLTAIC CELLS,

7. FUNCTIONAL COATINGS FOR COLORING OF TANDEM CELLS: DIGITAL MODEL CALCULATIONS.

In the introduction section, state of art solar cell coloring results are presented, with the novelty highlighted. Besides, here other important dissertation details are introduced: objectives, tasks, authors contribution, dissertation structure, publications, conferences and defensive statements.

In the second chapter ("Literature review"), the most relevant literature is examined. It is comprised of 3 sub-paragraphs: anti-reflective coatings (ARCs), sol-gel theory and colorimetry. In the first one, the analysis focuses on the reflectance characteristics of solar cells, as they play an essential role in this work. Starting from the Fresnel equations, the reduction of reflectance in silicon solar cells is explained and different anti-reflective coating types are detailed. In the second sub-paragraph, sol-gel theory is explained, that was used for the experimental realization of Bragg reflectors in 6th section of this work. While in the 3rd sub-section the colorimetry theory is presented with the most important characteristic parameters and their formulas to evaluate color quantitatively.

In the third section, the methodologies employed in this work are introduced. Those that were most frequently utilized are described in higher detail, and vice versa. Along with them simulation methodology is explained in detail as it was an essential part of this work.

The results are presented starting from the fourth chapter, where functional coatings based on double-layer anti-reflective coatings (DLARCs) are presented. These DLARCs were created on commercial solar cells by adding indium-doped tin oxide (ITO) as a top layer, utilizing both optical simulations and experimental implementations. In the fourth paragraph, emphasis was placed on exploring the impact of thickness variations on DLARC characteristics. Initially demonstrated through simulations, this effect was further validated experimentally by varying the thickness of the ITO layer. Next, characterization of these structures was performed. Moving to the fifth paragraph, the analysis shifted to the influence of the refractive index, considering a range of achievable values for ITO. Two defensive statements were formed from these paragraphs.

In the sixth section a different coloring idea is presented. In this case multilayered low and high refractive index coatings called Bragg reflectors were analyzed using simulations and realized experimentally. Using simulations this structure was optimized and then metal oxide layers deposited using sol-gel dipping technique. Later characterization followed and a 3rd defensive statement formed.

The final section of this work was designated to coloring of 2 terminal tandem structures. This seemed as the most logical continuation of previous results as currently tandem solar cells are under extensive research to replace single junction silicon solar cells. Therefore, in 7th section 2 terminal tandem kesterite/silicon solar cells were simulated using SCAPS and transfer matrix methods for the electrical and optical simulations (respectively). Firstly, structure was optimized, and then anti-reflective coating added as a final step. Finally colorimetric analysis was performed with variation of ARC thickness and 4th defensive statement formed.

1.5 Author's publication list

1.5.1 Publications

Publications on the topic of the dissertation in ISI journals:

- [P1] M. Rudzikas, A. Šetkus, M. Stange, J. Ulbikas, A. Ulyashin, Simple interference based colorization of Si based solar cells and panels with ITO/SiNx:H double layer antireflective coatings, *Sol. Energy.* 207 (2020) 218–227. <https://doi.org/10.1016/j.solener.2020.06.091>.
- [P2] M. Rudzikas, J. Donėlienė, E. Bužavaitė-Vertelienė, Z. Balevičius, C. Leuvrey, A. Šetkus, Design and investigation of Bragg reflector based structures for BIPV cell colorization by sol-gel dipping technology, *Sol. Energy.* 250 (2023) 285–294. <https://doi.org/10.1016/j.solener.2022.12.028>.
- [P3] M. Rudzikas, S. Pakalka, J. Don, Exploring the Potential of Pure Germa Kesterite for a 2T Kesterite / Silicon Tandem Solar Cell : A Simulation Study, *MDPI Mater.* (2023) <https://doi.org/10.3390/ma16186107>.

Publications not included into the dissertation:

- [N1] V. Bukauskas, S. Kaciulis, A. Mezzi, A. Mironas, G. Niaura, M. Rudzikas, I. Šimkiene, A. Šetkus, Effect of substrate temperature on the arrangement of ultra-thin TiO₂ films grown by a dc-magnetron sputtering deposition, *Thin Solid Films.* 585 (2015). <https://doi.org/10.1016/j.tsf.2015.04.007>.
- [N2] J. Doneliene, M. Rudzikas, S. Rades, I. Dörfel, B. Peplinski, M. Sahre, F. Pellegrino, V. Maurino, J. Ulbikas, A. Galdikas, V.D. Hodoroba, Morphology and structure of TixOy nanoparticles generated by

- femtosecond laser ablation in water, *Mater. Res. Express.* 5 (2018). <https://doi.org/10.1088/2053-1591/aaba56>.
- [N3] J. Doneliene, E. Fataraitė-Urbonienė, M. Rudzikas, S. Pakalka, N. Dančova, J. Ulbikas, Effect of precursor nature and sol-gel synthesis conditions on TiO₂ aerogel's structure, *Molecules.* 26 (2021). <https://doi.org/10.3390/molecules26165090>.
- [N4] T. Paulauskas, V. Pačebutas, A. Geižutis, M. Kamarauskas, M. Drazdys, M. Rudzikas, R. Kondrotas, A. Naujokaitis, I. Nevinskas, B. Šebeka, V. Strazdienė, A. Krotkus, Performance analysis of GaAsBi/InGaAs heterostructure for III-V multi-junction solar cells, *Sol. Energy Mater. Sol. Cells.* 248 (2022) 1–22. <https://doi.org/10.1016/j.solmat.2022.112013>.
- [N5] T. Paulauskas, V. Pačebutas, V. Strazdienė, A. Geižutis, J. Devenson, M. Kamarauskas, M. Skapas, R. Kondrotas, M. Drazdys, M. Rudzikas, B. Šebeka, V. Vretenár, A. Krotkus, Performance assessment of a triple-junction solar cell with 1.0 eV GaAsBi absorber, *Discov. Nano.* 18 (2023). <https://doi.org/10.1186/s11671-023-03865-x>.
- [N6] Saulius Pakalka; Jolanta Donelienė; Matas Rudzikas; Kęstutis Valančius; Giedrė Streckienė, Development and experimental investigation of full-scale phase change material thermal energy storage prototype for domestic hot water, *J. Energy Storage.* (2024). <https://doi.org/10.1016/j.est.2023.110283>.

1.5.2 Conferences attended on the topic of the dissertation

- [C1] Matas Rudzikas, Arūnas Šetkus, Marit Stange, Juras Ulbikas. Alexander G. Ulyashin, Simple color modification of commercial solar cells with ITO/SiN_x double layer coatings, *Fiztech 2019*, Vilnius, Lietuva.
- [C2] Matas Rudzikas, Arūnas Šetkus, Iš tirpalo formuojamų metalų oksidų sluoksnių optinių savybių priklausomybės nuo technologijos tyrimai ir praktinis taikymas fotovoltiniuose elementuose, *Fiztech 2020*, Vilnius, Lietuva.
- [C3] Matas Rudzikas, Arūnas Šetkus, Marit Stange, Juras Ulbikas. Alexander G. Ulyashin, Colorization of Si based solar cells and panels using double layer coatings, *PVSEC 2020*, Online.
- [C4] Matas Rudzikas, Jolanta Donelienė. Juras Ulbikas, Ernesta Bužavaitė-Vertelienė, Zigmas Balevičius, Arūnas Šetkus, Characterisation of colored glass plates with bragg lattice structure formed from sol-gel

solutions, ADVANCED MATERIALS AND TECHNOLOGIES 2021, Palanga, Lithuania.

- [C5] M. Rudzikas, A. Šetkus, N. Curmei, D. Serban, J. Donėlienė, J. Ulbikas, Alexander G. Ulyashin, Sol-gel method for double layer coated colored silicon solar cells, EU PVSEC 2021, Online.
- [C6] M. Rudzikas, J. Donėlienė, J. Ulbikas, A. Šetkus, Sol-gel Coated Bragg reflector Structures for Colored PV, Silicon PV 2022, Konstanz, Germany (attended online).
- [C7] M. Rudzikas, J. Donėlienė, S. Pakalka, A. Šetkus, A simulation study of pure germanium kesterite to be used for 2t kesterite/silicon tandem cell, EU PVSEC 2023, Lisbon, Portugal.

1.6 Defensive statements

First defensive statement. Thickness variation of ITO or similar metal oxide from 0 to 240 nm as a part of double layer anti-reflective coating formed on the top of the commercial silicon solar cell enables the adjustment of cell's color palette from blue to brown. This modification is associated with a relatively low current density loss of up to 8%, and post-lamination color purity decreases by 82% for blue and 71% for green PV panels.

Second defensive statement. Tuning the refractive index of ITO used in double layer anti-reflective coatings of silicon solar cells on the top of $\text{SiN}_x\text{:H}$ produces lower, blue-shifted and narrower reflection peaks in the surface reflection spectrum when the ITO refractive index is lower (1.8 at 632 nm) compared to a higher refractive index (2.07 at 632 nm). This leads to comparable hues and color purity and a higher color brightness for higher ITO refractive index.

Third defensive statement. Optimal design of Bragg reflector structure for coloring of solar panels using TiO_2 and SiO_2 metal oxides consists of only 3 layers formed on the glass substrate (glass/ TiO_2 / SiO_2 / TiO_2) and results in 2-3 times higher brightness compared to the panels with colored commercial solar cells. The tolerable technological deviations from the color related numbers to be indistinguishable by human eye are +/- 0.05 for the refractive index spectrum and less than approximately +/- 2% for the thickness.

Fourth statement. ARC thickness variation of Al_2O_3 from 0 to 300 nm allows modification of reflectance spectra and therefore also color of kesterite/silicon monolithic tandem solar cells with efficiency loss of less than 2% relative. Such modification is restricted by low color purity (compared to single junction solar cells) and hues are limited to brownish and purplish (and their mix).

2. LITERATURE REVIEW

2.1 Anti-reflective coatings

Plain silicon has a reflectance spectrum of around 30%, which is a significant optical loss for a solar cell. To mitigate such loss, anti-reflective coatings (ARCs) are employed in solar cells (and texturization added). This is a single or multiple thin layers (from tenths to hundreds of nm thick) that are designed to reduce reflection. Reflection is minimum when layer optical thickness equals quarter of wavelength. Usually in PV devices ARC thickness is set to have minimum at around 600 nm, where solar cells have highest quantum efficiency values [42]. While for the deposition plasma enhanced chemical vapor deposition (PECVD) is used [43]. However, by using double layer coatings with $\lambda/4$ design, with growing indices from air to silicon, the minimum in reflection is broader in wavelength.

Electromagnetic wave propagating in multilayered structure undergoes multiple reflections and transmissions as it is shown in Figure 1. As anti-reflective coatings are less thick than the coherence length of light (which is typically less than $30 \mu\text{m}$ [44]), it results in constructive and destructive interference pattern. It can be described analytically using Fresnel's equations [45]:

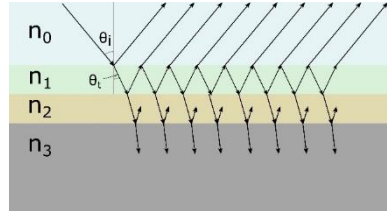


Figure 1. Electromagnetic wave paths in DLARC structure, where n_0 – air, n_1 and n_2 – 1st and – 2nd antireflective coating and n_3 – substrate.

$$r_{\perp} = \frac{\tilde{n}_i \cos \phi_i - \tilde{n}_{i+1} \cos \phi_{i+1}}{\tilde{n}_i \cos \phi_i + \tilde{n}_{i+1} \cos \phi_{i+1}} \quad (1)$$

$$r_{\parallel} = \frac{\tilde{n}_{i+1} \cos \phi_i - \tilde{n}_i \cos \phi_{i+1}}{\tilde{n}_{i+1} \cos \phi_i + \tilde{n}_i \cos \phi_{i+1}} \quad (2)$$

Here r_{\perp} and r_{\parallel} are Fresnel reflection coefficients for perpendicular and parallel polarized light (s-polarized and p-polarized), ϕ_i and ϕ_1 are incidence angle and refracted beam angle (shown in Figure 1).

Often only a perpendicular light beam is considered with metal oxide coatings having little or no absorption. This allows to simplify the equations ($\phi_i = 0, k = 0, k$ – extinction coefficient):

$$r = r_{\perp} = r_{\parallel} = \frac{n_{i+1} - n_i}{n_{i+1} + n_i} \quad (3)$$

From this reflection coefficient can be easily calculated:

In order to calculate reflection amplitude, which is the sum of all partial reflections, we need firstly to add them. For SLARC this results in the following formula:

$$r = \frac{r_1 + r_2 e^{-i\delta}}{1 + r_1 r_2 e^{-i\delta}}; \quad (4)$$

$$\delta = \frac{2\pi}{\lambda} nd; \quad (5)$$

Where δ is phase change between two subsequent layers. By multiplying reflectance amplitude with its complex conjugate, we can obtain reflectance coefficient:

$$R = \frac{r_1^2 + r_2^2 + 2r_1 r_2 \cos\delta}{1 + r_1^2 r_2^2 + 2r_1 r_2 \cos\delta}; \quad (6)$$

Besides, optimal refractive index for SLARC also can be easily calculated ($n_s > n_1$) [7]:

$$n_1 = \sqrt{n_0 n_s} \quad (7)$$

Here n_s – is a refractive index of a substrate.

In case of DLARC, reflection amplitude gets much more complicated, shown in our first article [46]. While optimal refractive indexes for DLARC using quarter wavelength stacks is [47]:

$$\frac{n_1}{n_2} = \sqrt{\frac{n_0}{n_s}} \quad (8)$$

It should be noted that there are other anti-reflective coating types, like gradient, porous, biomimetic photonic nanostructures, ARC gratings [48]. However, they are more complicated and less relevant for this work, therefore not detailed in this paragraph.

2.2 Sol-gel solution theory (for Bragg reflector structures)

For the preparation of Bragg reflectors in the 6th section of this work, sol-gel solutions were employed. This selection was favored for the cost effectiveness and scalability of this method [49–51].

The term "sol-gel" has evolved over time, and now it can simply be referred to as the formation of solid materials from liquid precursors. Sol can be described as a colloidal solution of amorphous, crystalline, or polycrystalline nanoparticles, traditionally obtained through the hydrolysis and condensation of alkoxide precursors (although not exclusively) [52]. A gel is a particular three-dimensional network of a solid in a liquid, typically formed by the aggregation of nanoparticles present in the sol. If covalent

bonds form among them, the process is irreversible, whereas weak Van der Waals or hydrogen bonding results in a reversible process. The structure of the gel network strongly depends on the size and shape of the sol particles [53]. Gels can be classified into five groups: (a) colloidal, (b) metal-oxane polymer, (c) metal compounds, (d) polymer network I and (e) polymer network II (Figure 2) [49]. However, this is just one of the most used classifications, as there is currently no universally accepted categorization.

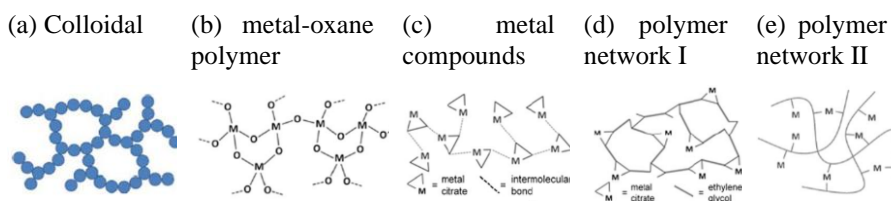


Figure 2. Classification of gels according to the work by A. E. Danks, S. R. Hall and Z. Schnepp (used with permission) [49].

Agglomeration of sol particles aims to reduce their interlayer energy by decreasing the surface area-to-volume ratio, and it occurs due to Van der Waals forces [53]. Various additives are employed to prevent agglomeration.

Usually, various metal nitrides, chlorides, and acetates are employed as precursors for such solutions, which are soluble in water or alcohol solvents. Several main types of precursors can be distinguished:

- Inorganic compounds: nitrates, sulfates, chlorides;
- Metal-organic compounds: acetates, carbonates, butoxides, oxalates, alkoxides, $\text{Cu}(\text{hfac})_2$;
- Organometallic compounds: polymeric sols, particle sols, emulsions.

In this work only results with metal-organic precursors are presented, therefore only theory related with these precursors will be presented.

Key stages in the formation of sol-gels:

1. Formation of sol (dispersed system with a dispersed phase of solid particles in the range of 10-100 nm) through hydrolysis and partial condensation with alkoxides. During hydrolysis, a metal alkoxide reacts with water, replacing one or several -OR groups with hydroxyl (M-OH) or oxide compounds.
2. Formation of the gel through polycondensation reactions, creating metal-oxo-metal or metal-hydroxide-metal bonds;
3. Aging – a process during which the gel network is formed. Aging often leads to a reduction in the volume of the solution due to the removal of the solvent;

4. Drying of the gel to form a dense xerogel, resulting in a deformed pore structure or an aerogel (e.g., by supercritical drying method);
5. Removal of surface M-OH groups by heating.

2.3 Dip coating deposition technique

Dip coating technique was used for the deposition of Bragg reflector structures from sol-gel solutions due to its high repeatability, high homogeneity, low material waste and easy obtainable thin films. One of alternatives was spin-coating which is a common method in research community, however it is not scalable. Another possibility would be spray pyrolysis (ultrasonic), but its challenging to make thin film and homogeneous films, therefore dip coating was favoured. It should be noted that spray pyrolysis technique was employed in the progress of this work, however it was dropped after some time, as no successful films were prepared. Therefore, only results using dip coating will be presented in the dissertation.

The dip coating system consists of a withdrawal platform with a fixing point for substrate that can move relative to the vessel: into the liquid solution and out of it. Usually the substrate is fixed vertically, immersed and pulled out of the liquid at a constant speed (Figure 3). Although dip coating deposition is quite easy, the physics and chemistry involved in this process is rather complex. During the immersion process at least six forces drive the formation of the film: gravity, the viscous drag force between the liquid and the substrate, the meniscus surface tension force, the inertia force of the liquid at the boundary between the formed coating and the liquid, the surface tension force gradient, and the (dis)conjoining pressure force [54].

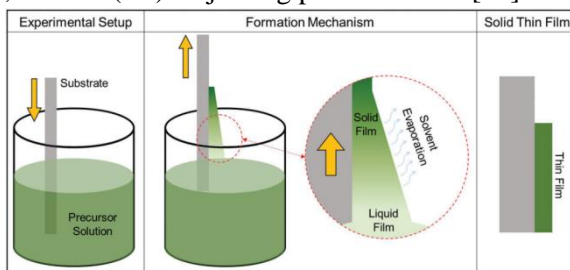


Figure 3. A scheme of dip coating process (used with a permission from the work from Colm Glynn and Colm O'Dwyer [55]).

To achieve uniform layers, it is important to use the solvent, which has a low surface tension and can be sufficiently volatile and fluid. Alcohols meet these conditions and thus are frequently used in this process.

Depending on the deposition speed, two main coating regimes can be distinguished: capillary/evaporation and drain/evaporation [55]. The capillary

regime happens at slow withdrawal speeds, while the drain regime occurs at high speeds. It is important to note that the layer thickness increases with an increase in withdrawal speed in the drain regime, while in the capillary regime, it is the opposite.

The thickness of the layer in the dipping process primarily depends on the withdrawal speed. However, other parameters are also important, including the precursor solution concentration, temperature, angle between the substrate and the vertical (if applicable), and withdrawal acceleration (if applicable).

Landau proposed a model to determine the thickness of the coated layer, applicable in the fast withdrawal regime [55]:

$$h_0 = 0,94 \frac{(U_0 \eta)^{2/3}}{\sqrt[6]{\gamma \sqrt{\rho g}}}, \quad (9)$$

where: U_0 is the withdrawal speed, η is the viscosity, γ is the surface tension, ρ is the density, and g is the gravitational acceleration. The model considers Newtonian fluids, and evaporation is assumed to be negligible. The slow withdrawal speed regime is not detailed as it is not relevant to this work.

2.4 Magnetron sputtering deposition technique

Magnetron sputtering is one of thin film formation techniques [56]. A scheme of its working principle is depicted in Figure 4. An electric field is established between the cathode (at the bottom) and the anode (the top). Perpendicular to it, a magnetic field is created near the target surface in such a way that its lines curve towards the sample surface. At the bottom, the target of the material that is being vaporized is placed, while at the top, a substrate is fixed on which the material layer will be deposited.

Electrons when subjected to an electric and magnetic field move in spirals around the lines of the magnetic field, as depicted in the image. When gas are (usually argon) introduced in a chamber they are ionized due to atom-electron collisions and directed towards the cathode. This way plasma is formed above the target. Upon colliding with the target, argon ions displace atoms from its material. The neutral target atoms move straight towards the substrate. In order for them to reach the substrate they need a considerable mean free path. Hence, magnetron sputtering requires a relatively high vacuum on the order of 10^{-6} torr.

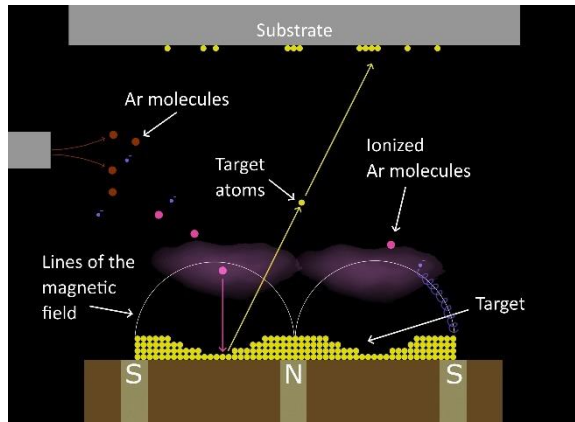


Figure 4. The scheme of the magnetron sputtering process.

Magnetron sputtering has an advantage over regular ion sputtering in terms of higher vaporization rate because electrons are concentrated in a smaller space, resulting in a faster ionization process [57].

To vaporize non-conductive layers (such as metal oxides), variable voltage is required. For this, Radio Frequency (RF) Sputtering is used allowing to alternate the electric field at radio frequencies. This is employed to prevent the accumulation of charge on not conductive types of sputtering target materials (or oxides). Over time, such charge buildup can result in arcing into the plasma, generating droplets that create quality control issues on thin films. In extreme cases, it may even lead to the complete cessation of atom sputtering, thus terminating the entire process.

The properties of the vaporized layer depend on pressure, temperature, vaporization time, gas ratio (in case of reactive sputtering), and material constants.

2.5 Solar panel lamination

Meier Icolam 18/11 membrane laminator was used for the lamination of PV mini panels.

In the production of crystalline silicon solar modules, a vacuum lamination step is employed to integrate the components of the module into a single entity. Throughout this process, encapsulation materials are bonded together by heating them to a temperature range of 120-150°C for 7 to 15 minutes (with a potential extension for thicker glass exceeding 2-4 mm).

Typically, a flat laminator is utilized, and its schematic is depicted in Figure 5. Two chambers are present in such a laminator: upper and lower, and they are interconnected through a membrane. Both can be independently

evacuated, and the module lay-up is typically heated in the lower chamber using a heating plate. The heating plate is connected to the module through so-called pins, facilitating a more gentle and homogeneous heat transfer (compared do direct heat transfer) to prevent glass warping initiated temperature differences between the front and bottom glass of the PV panel.

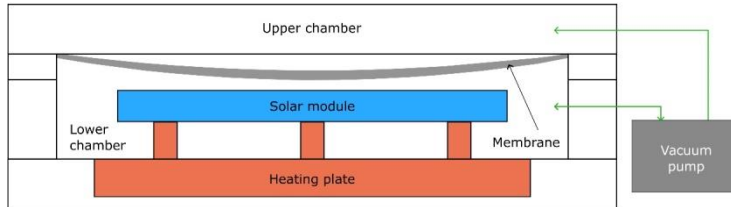


Figure 5. A diagram of the flat-bed laminator with its main components: the membrane that separates the upper and lower chambers (grey), solar module (blue), the heater (red), a vacuum pump (grey), space surrounding the module – the lower chamber, and the space above the membrane - the upper chamber.

The lamination process consists of three main steps [58] (typical lamination working diagram is depicted in Figure 6):

1. In the upper chamber, the space is evacuated before placing the components forming the module stack onto the laminator on the heating plate. Then the lower chamber is vacuumed over a certain period of time to remove air, preventing the formation of bubbles. Simultaneously, the temperature of the laminator is raised to the required level for the polymerization reaction to take place (or for thermoplastics to melt). As the temperature rises, the elastomer softens and liquefies.
2. In the second step, when the required temperature is reached, the polymerization reaction occurs. This is a reaction occurring at elastomer or thermoplastic elastomer materials which chemically crosslink after certain temperatures, causing irreversible solidification and adhesion to glass. Ethylene vinyl acetate is one of such materials and most popular for use in PV panels, as it accounts for up to around 72% of whole encapsulation market (even around 83%, including POE mixed with EVA) [11]. During this process, the upper chamber is ventilated (while maintaining the lower chamber in a vacuum), creating a pressure of up to 100 kPa on the module. This compression enhances the adhesion of the solidified EVA to the glass.
3. The final step is the cooling of the module. In some cases, modules are cooled in the air, in some other cases cooling is performed in laminator with special cooling mode or alternatively, a separate space or device is used, creating specific cooling conditions.

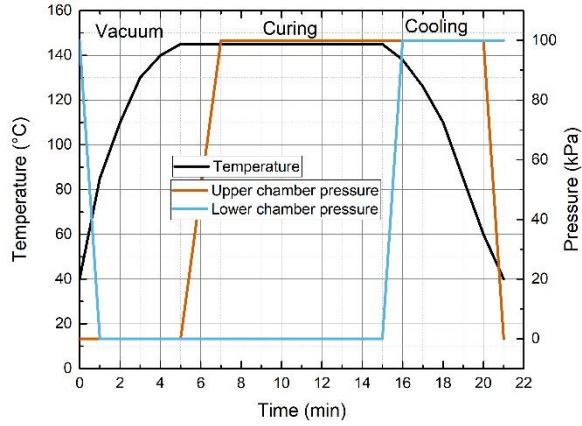


Figure 6. Typical laminator working diagram. Temperature is displayed with black curve, upper chamber pressure in red, lower chamber pressure in light blue.

Important to note that for each laminator and each different module or material, it is necessary to individually adjust the lamination conditions to achieve optimal results: a fast process and a high-quality PV module.

2.6 Colorimetry

2.6.1 CIE color space and its colorimetry parameters

The International Commission on Illumination (CIE) established a method in 1931 to connect the visible spectra to the perceived colors by the human eye. This connection is now known as the CIE 1931 XYZ color space, which is depicted in Figure 7 (b).

To determine the relationship between the incident spectra and the perceived colors, the tristimulus values of X, Y, and Z are computed. These values correspond to the response of different receptor cells in the human eye, as defined by the CIE's three color matching functions: $\hat{x}(\lambda)$, $\hat{y}(\lambda)$ and $\hat{z}(\lambda)$ (shown in Figure 7 (a)). Collectively, these functions are referred to as the standard observer, representing an individual with average vision, described in numerical terms. The tristimulus values X, Y, and Z are calculated by integrating the product of three spectra: reflectance or transmittance, irradiance of the source and the receptor cell response.

$$X = k \int_{\lambda_1}^{\lambda_2} I(\lambda) \cdot S(\lambda) \cdot \hat{x}(\lambda) d\lambda \quad (10)$$

$$Y = k \int_{\lambda_1}^{\lambda_2} I(\lambda) \cdot S(\lambda) \cdot \hat{y}(\lambda) d\lambda; \quad (11)$$

$$Z = k \int_{\lambda_1}^{\lambda_2} I(\lambda) \cdot S(\lambda) \cdot z(\lambda) d\lambda; \quad (12)$$

$$k = \frac{100}{\int_{\lambda_1}^{\lambda_2} I(\lambda) \cdot y(\lambda) d\lambda}; \quad (13)$$

where $I(\lambda)$ is the irradiance of the source ($W \cdot m^{-1} \cdot nm^{-1}$) (D65 illuminant is CIE standard for 6500 K light [60]), $S(\lambda)$ is reflected or transmitted spectra (nm^{-1}), λ_1 and λ_2 are 380 and 780 nm respectively, covering the entire photopic region.

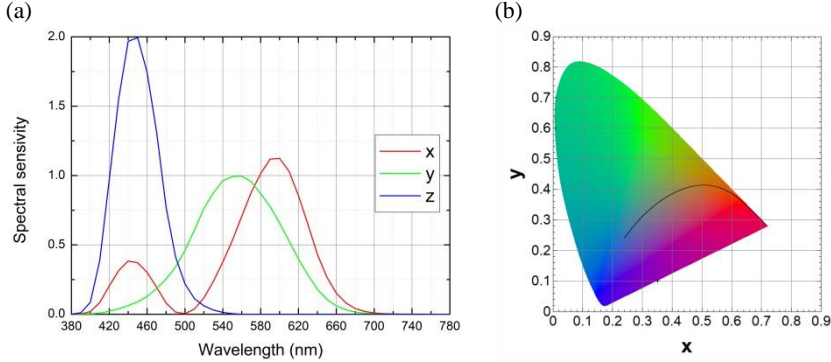


Figure 7. CIE 1931 standard observer color matching functions for 10 deg. View (a). CIE 1931 color space chromaticity diagram (b).

To more convenient representation, the tristimulus values are frequently converted into alternative color spaces since the three-dimensional (3D) space is not always practical. An instance of such conversion is the xyY gamut, in which the variables x and y correspond to chromaticity (hue and saturation), while Y corresponds to brightness. This enables the depiction of chromaticity on a single xy plane while maintaining a fixed Y value. The relationships between the variables x and y and the tristimulus variables can be expressed as follows:

$$x = \frac{X}{X + Y + Z}; \quad (14)$$

$$y = \frac{Y}{X + Y + Z}. \quad (15)$$

The xyY space is specifically designed to exhibit a gradient of increasing color saturation from the white point positioned at the center of the color space, towards the boundaries. At the edges, colors become monochromatic [5].

Using xyY space it is possible to calculate color purity – a parameter like color saturation. It is a ratio between distance from the illuminant (in this case

D65) (Figure 8 point N) to a point of interest (Figure 8 point O) divided by a distance between illuminant and the opposite point at loci of fin shaped xyY space (Figure 8 point D).

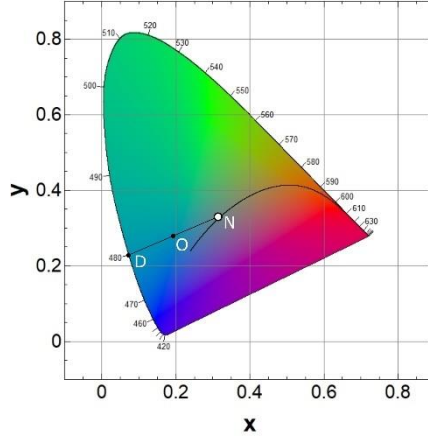


Figure 8. Scheme of calculation of dominant wavelength and excitation purity.

The formula for calculating of excitation purity is as follows:

$$p_e = \frac{NO}{ND} = \frac{x_0 - x_N}{x_D - x_N} = \frac{y_0 - y_N}{y_D - y_N}. \quad (16)$$

2.6.1 CIELAB color space and color difference threshold parameter ΔE

In the context of applying colored PV technologies in BIPV (Building-Integrated Photovoltaics), it is essential to consider how manufacturing process affects color. As this thesis is in field of physics (not technology) the sensitivity of color of functional oxide layers to the two main parameters: refractive index and thickness was analyzed. Although, it was not explored how these two parameters could be modified through the deposition process.

For this analysis, the CIELAB color space was employed as it is relatively perceptually uniform. Color variations were assessed using a parameter defined by the CIE International Standard called ΔE [61]. In the year 2000, certain non-uniformities in this color space were corrected and these corrections were utilized in this work. The formula for ΔE_{00} is shown below:

$$\Delta E_{00} = \sqrt{\left(\frac{\Delta L'}{k_L S_L}\right)^2 + \left(\frac{\Delta C'}{k_C S_C}\right)^2 + \left(\frac{\Delta H'}{k_H S_H}\right)^2 + R_T \left(\frac{\Delta C'}{k_C S_C}\right) \left(\frac{\Delta H'}{k_H S_H}\right)}, \quad (17)$$

where

$$S_L = 1 + \frac{0.015(\bar{L}' - 50)^2}{\sqrt{20 + (\bar{L}' - 50)^2}} \quad (18)$$

$$S_C = 1 + 1.045\bar{C}', \quad (19)$$

$$S_H = 1 + 1.045\bar{C}'T, \quad (20)$$

$$T = 1 - 0.17\cos(\bar{h}' - 30^\circ) + 0.24\cos(2\bar{h}') + 0.32\cos(3\bar{h}' + 6^\circ) - 0.2\cos(4\bar{h}' - 63^\circ) \quad (21)$$

$$R_T = -\sin(2\Delta\theta)R_C, \quad (22)$$

$$\Delta\theta = 30^\circ + \exp\left\{-\left[\frac{\bar{h}' - 275^\circ}{25^\circ}\right]^2\right\}, \quad (23)$$

$$R_C = 2 \sqrt{\frac{(\bar{C}')^7}{(\bar{C}')^7 + 25^{7'}}} \quad (24)$$

\bar{L}' and $\Delta L'$ - arithmetic mean and difference of the CIEDE2000 CIELAB lightness of two colour stimuli (respectively).

\bar{C}' and $\Delta C'$ - arithmetic mean and difference of the CIEDE2000 CIELAB chroma of two colour stimuli (respectively).

\bar{H}' and $\Delta H'$ - arithmetic mean and difference of the CIEDE2000 CIELAB hue of two colour stimuli (respectively).

\bar{h}' and $\Delta h'$ - arithmetic mean and difference of the CIEDE2000 CIELAB hue angle of two colour stimuli (respectively).

T - T-function for hue weighting.

R_T, R_C - rotation function, chroma dependence of rotation function (respectively).

S_L, S_C, S_H - lightness, chroma and hue weighting functions (respectively).

$\Delta\theta$ - hue dependence of rotation function.

k_L, k_C, k_H - parametric factors for lightness, chroma and hue (respectively).

The threshold for color difference is divided into five sections, following the classification proposed by W. Mokrzycki and M. Tatol [62]:

- $0 < \Delta E < 1$: The difference is not noticeable to the observer.
- $1 < \Delta E < 2$: Only experienced observers can detect the difference.
- $2 < \Delta E < 3.5$: Even unexperienced observers notice the difference.
- $3.5 < \Delta E < 5$: A clear difference in color is noticeable.
- $5 < \Delta E$: The observer perceives two distinct colors.

It's important to mention that this classification was based on the author's own experiments and is not metrologically approved. To our

knowledge, the CIE (International Commission on Illumination) does not provide a similar classification. Thus, in this article, the suggestion of W. Mokrzycki and M. Tatol was adopted as a starting point, and a visual comparison was also conducted with the sRGB portrait.

3. METHODOLOGIES USED IN THE RESEARCH

3.1 Transfer matrix method (for 1D optical simulations)

To perform optical simulations on a multilayered structure, the Abeles transfer matrix method (TMM) was utilized. This method employs 2x2 matrices to describe the amplitude and phase properties of the electromagnetic wave for each layer and interface within the structure. To facilitate the application of this method, a Python package developed by Steven J. Byrnes was employed [63].

The Abeles transfer matrix method is based on the changes in the electric field between the incident wave and the one that has passed through the layer of material(s):

$$\begin{pmatrix} E_0^+ \\ E_0^- \end{pmatrix} = M \begin{pmatrix} E_{m+1}^+ \\ E_{m+1}^- \end{pmatrix}. \quad (25)$$

Here E_0^+ is an electric field of incoming wave from the left, E_{m+1}^+ is an electric field of (transmitted + reflected) wave moving to the right, E_0^- is (reflected + transmitted) wave coming from the right, E_{m+1}^- coming wave from the right, M – transfer matrix, m – layer numbering from the top ($0, 1, 2, \dots, m+1$).

The transfer matrix describing the changes of the phase and the amplitude at the junction and in the material layer (respectively):

$$M_m = \begin{pmatrix} \exp(-i\delta_{m-1}) & r_{m-1} \exp(-i\delta_{m-1}) \\ r_{m-1} \exp(i\delta_{m-1}) & \exp(i\delta_{m-1}) \end{pmatrix}; \quad (26)$$

Number of junctions and layers is usually not the same in the multilayered structure, therefore it is convenient to decompose this matrix into the matrix of permeability and transmission:

$$T_m = \frac{1}{t_m} \begin{pmatrix} 1 & r_{m-1} \\ r_{m-1} & 1 \end{pmatrix}; \quad (27)$$

$$P_m = \begin{pmatrix} \exp(-i\delta_{m-1}) & 1 \\ 1 & \exp(i\delta_{m-1}) \end{pmatrix}; \quad (28)$$

Then, the final matrix is obtained combining all the matrices describing each layer and each interface:

$$M = T_{01}P_1T_{12}P_2T_{23} \dots T_{m+1}. \quad (29)$$

Subscripts show the number of layers in which light propagates (transmission matrix) or the number of the layers before and after the interface that it passes (permeability matrix). r and t are Fresnel coefficients for reflection and transmission (respectively) and are equal to (for p and s polarized light, respectively):

$$r_m = \frac{\tilde{n}_m \cos(\phi_m) - \tilde{n}_{m+1} \cos(\phi_{m+1})}{\tilde{n}_m \cos(\phi_m) + \tilde{n}_{m+1} \cos(\phi_{m+1})}; \quad (30)$$

$$r_m = \frac{\tilde{n}_{m+1} \cos(\phi_{m+1}) - \tilde{n}_m \cos(\phi_m)}{\tilde{n}_{m+1} \cos(\phi_{m+1}) + \tilde{n}_m \cos(\phi_m)}. \quad (31)$$

where, \tilde{n} is complex refractive index, ϕ – incidence angle, o δ - phase change between two subsequent layers:

$$\tilde{n} = n + ik; \quad (32)$$

$$\delta_m = \frac{2\pi}{\lambda} \tilde{n}_m d_m \cos(\phi_m). \quad (33)$$

Equation (25) represents general situation with 2 waves coming from both sides of the multilayered structure. However usually wave comes only from one direction, therefore E_{m+1}^- can be excluded:

$$\begin{pmatrix} E_m^+ \\ E_m^- \end{pmatrix} = \frac{M}{t_f} \begin{pmatrix} E_{m+1}^+ \\ E_{m+1}^- \end{pmatrix} \rightarrow \begin{pmatrix} E_m^+ \\ E_m^- \end{pmatrix} = \frac{M}{t_f} \begin{pmatrix} E_{m+1}^+ \\ 0 \end{pmatrix}. \quad (34)$$

In this equation t_f is a result of multiplication of all Fresnel coefficients of transmission. This simplification allows simple calculation of transmission and reflection coefficients. After matrix multiplication equation system looks like this:

$$E_m^+ = \frac{M_{11} E_{m+1}^+}{t_f}; \quad (35)$$

$$E_m^- = \frac{M_{21} E_{m+1}^+}{t_f}. \quad (36)$$

Then transmission and reflection coefficients are equal to:

$$t = \frac{E_{m+1}^+}{E_m^+} = \frac{t_f}{M_{11}}; \quad (37)$$

$$r = \frac{E_m^-}{E_m^+} = \frac{M_{21}}{M_{11}}. \quad (38)$$

3.2 SCAPS software (for 1D electrical simulations)

Electrical part of solar cell was simulated using SCAPS (version 3.3.10) - a 1D solar cell simulation software, which was developed at the Department of Electronics and Information Systems (ELIS) of the University of Gent, Ghent, Belgium [20].

Software allows to construct thin film or crystalline silicon solar cell with a maximum number of 7 layers. Important to note that reflection is not included in the software, only absorption from the file or from model (calculated using material band gap and thickness). Within the software standard semiconductor equations are solved - Poisson equation and continuity equation for electrons and holes with the drift-diffusion approximation [42]:

$$\nabla \cdot \epsilon \vec{E} = q(n_0 - p_0 + N_A - N_D); \quad (39)$$

$$\nabla \cdot \vec{J}_n = q \left(G_n - R_n - \frac{\partial n}{\partial t} \right); \quad (40)$$

$$\nabla \cdot \vec{J}_p = q \left(G_p - R_p - \frac{\partial p}{\partial t} \right). \quad (41)$$

In formulas \vec{E} - is electric field, n and p - are electron and hole concentrations, N_D and N_A - donor and acceptor concentrations, \vec{J}_n ir \vec{J}_p - electron and hole current densities, G - optical carrier generation rate, R - thermal carrier generation rate.

Tandem cell simulation is partially supported in software, however limited to same 7 layers, therefore in this work tandem was simulated as 2 separate sub-cells and then connected artificially with special python script (ideal connection considered). Supported recombination mechanisms are band-to-band, Auger and SRH.

3.3 PV lighthouse simulation tool (for 1D optical simulations)

„OPAL 2” is an optical simulator available at the PV Lighthouse website free of charge[41]. It can be used to simulate the front surface of a photovoltaic solar cell. Structure of maximum of 5 layers over the substrate can be constructed from the material database (or custom refractive index spectra can be added) to calculate transmission through the coatings to the substrate, absorption in thin films and reflection from the whole structure. Layers used in simulation can be textured or plain and light can come in any angle and polarization.

Software uses Ray tracing and Fresnel equations to calculate reflection, transmission and absorption [41]. Optical loss is quantified as lost generation

current. For the calculation of this current authors suggest 1 of 4 light trapping schemes. In this work, the model 4 was selected as it has the fewest assumptions [65].

$$Z = 4 + \frac{\ln(n^2 + 4(1 - n^2)\alpha W e^{-4\alpha W})}{\alpha W} \quad (42)$$

$$A = \frac{A = 1 - e^{-4\alpha W}}{1 - \left(1 - \frac{1}{n^2}\right) e^{-4\alpha W}}. \quad (43)$$

Where Z – is a parameter that defines the light trapping - optical path length enhancement factor, A – absorption, W – substrate thickness, α – absorption coefficient, n – refractive index.

3.4 Calculation of Maximum Possible J_{SC} and J_{SC} Loss (for tandem simulations):

In the 7th section of this work, tandem calculations were performed. Using the transfer matrix method overall reflectance and absorbance in each of the layers of the multilayered structure was calculated for the evaluation of how much these spectra effects solar cell's electrical characteristics. In some cases, it can be loss (parasitic loss for example in ITO or because of reflectance) or gain (for example absorbance in absorber layers). J_{SC} values were calculated using equation below (EQE is not included as SCAPS does not generate EQE when the carrier generation is imported—not calculated inside):

$$J_{SC}(loss, gain) = q \int_{\lambda_1}^{\lambda_2} A(\lambda) \Phi_0(\lambda) d\lambda, \quad (44)$$

3.5 Calculation of carrier generation profile (for tandem simulations)

Carrier generation profiles for tandem simulations were calculated for solar cell absorber layers (silicon and pure germanium kesterite – $Cu_2ZnGe(S,Se)_4$ using absorption spectra obtained from transfer matrix calculations. These profiles were later used for SCAPS calculations.

The carrier generation profile can be calculated using an equation from the book by A. Luque and S. Hegedus [42]:

$$G(x) = (1 - s) \int_{\lambda_1}^{\lambda_2} (1 - R(\lambda)) \Phi_0(\lambda) \alpha(\lambda) e^{-\alpha x} d\lambda, \quad (45)$$

where s - metal grid coverage ratio (considered 0), $R(\lambda)$ - absorption, $\Phi_0(\lambda)$ - photon flux from solar AM1.5g spectrum, $\alpha(\lambda)$ - absorption coefficient, x - layer thickness. Solar spectrum AM1.5g was taken from NREL [66].

The absorption coefficient was calculated from the imaginary part of refractive index spectrum using:

$$\alpha(\lambda) = \frac{2\pi k(\lambda)}{\lambda} \quad (46)$$

Photon flux spectrum was calculated from irradiance spectrum:

$$\Phi_0(\lambda) = I(\lambda) \frac{\lambda}{hc}. \quad (47)$$

However, one modification was added to the equation (45) regarding specifics of this work. It was assumed, that instead of $I-R(\lambda)$, absorbance $A(\lambda)$ spectrum can be used, as it is calculated using optical simulations with transfer matrix method in multilayered structure. Thus, such modification resulted in:

$$G'(x) = (1 - s) \int_{\lambda_1}^{\lambda_2} A(\lambda) \Phi_0(\lambda) \alpha(\lambda) e^{-\alpha x} d\lambda, \quad (48)$$

Besides, to make sure, that all the light was absorbed lengthwise (in x axis), normalization was performed. For this, firstly the short circuit current density was calculated by the integration of the obtained carrier generation profile and then multiplied with elementary charge:

$$J'_{sc} = q \int_{x_1}^{x_2} G'(x) dx. \quad (49)$$

While full short circuit current density is obtained using:

$$J_{sc}(full) = q \int_{\lambda_1}^{\lambda_2} A(\lambda) \Phi_0(\lambda) d\lambda, \quad (50)$$

Then, final generation profile is calculated by multiplication of $G'(x)$ with a ratio of these two short circuit current densities:

$$G(x) = G'(x) \frac{J_{sc}(full)}{J'_{sc}} \quad (51)$$

3.6 Sample characterization methods

3.6.1 Optical spectroscopy

The Bentham PVE 300 spectrometer was employed to measure the optical and electric properties, specifically the reflectance spectra and Quantum efficiency. Principal scheme of such equipment is shown in Figure 9.

A combination of xenon and halogen lamps are utilized as a light source in this spectrometer, and a controlled swing-away mirror is employed to switch between the two. The rationale behind using multiple light sources is to achieve a higher and more stable output. After the swing away mirror, the light passes the monochromator, and comes out as a monochromatic beam

with wavelengths ranging from 300 to 1750 nm. Bentham monochromators employ diffraction gratings for wavelength dispersion. Subsequently, the light passes through the slit (custom shaping the beam), travels through a mirror system, and reaches the integrating sphere (shown in Figure 10). The incident light hits the surface at an 87-degree angle from the surface normal. The integrating sphere is coated with barium sulphate, a highly diffusely reflecting material. It is termed so because light impinging on the sphere walls is reflected in all directions, effectively "averaging" the light over the surface of the sphere walls. This design ensures that the detector detects the same signal independent of its position. In reality, some light may still exit from the entrance and reflectance port.

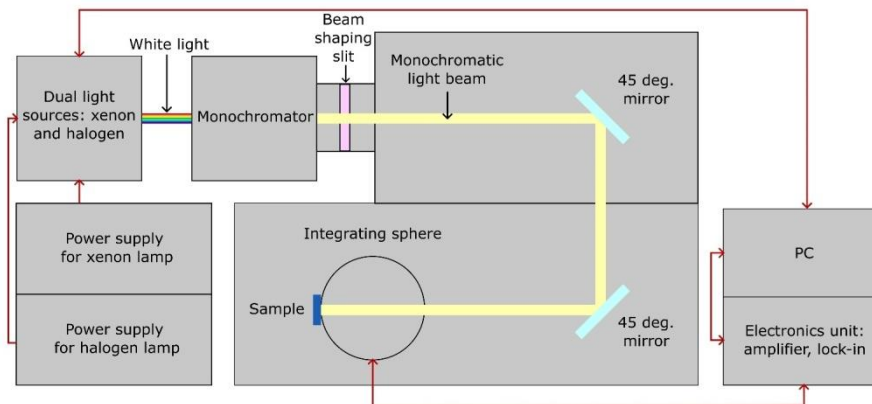


Figure 9. Principal scheme of reflectance measurement with a spectrometer.

In the case of quantum efficiency measurements, integrating sphere is not used, but beam is directed on sample and signal from the solar cell contacts is connected to the electronics unit. Besides, temperature control is employed for such measurement. For low level recording detection lock-in is used.

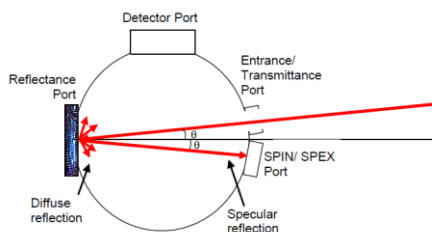


Figure 10. Scheme of an integrating sphere. Sample is shown in blue color (in reflectance mode). In transmittance mode, sample is place at entrance and reflectance port is covered with highly reflective surface. Figure taken from the equipment manual and used with permission [67].

3.6.2 J-V measurements under the light

The measurement of mini solar panel J-V characteristics was performed using the Pasan Highlight 3 A+ class simulator. Solar cells were characterized using A class solar simulator QuickSun 120CA. These measurements were done under standard conditions (1000 W/m² irradiance, 25 °C temperature, and AM1.5G solar spectrum) according to IEC 61215 standard. Both simulators are pulse type (not continuous).

For the clarity of solar simulator classification, characteristics of each class are detailed in Table 1 [68].

Table 1. Solar simulator classification characteristics [68].

Classifications	Spectral Match	Non-uniformity of irradiance	Temporal instability of irradiance	
			Short term instability	Long term instability
A+	0.875-1.125	1%	0%	1%
A	0.75-1.25	2%	0.5%	2%
B	0.6-1.4	5%	2%	5%
C	0.4-2	10%	10%	10%

Principal scheme of solar simulator is depicted in Figure 11. Main components of such equipment are a light source (usually a xenon lamp), sample holder, temperature sensor, electronic load, flash generator, PC and monitor cell. All the system is controlled using PC and designed software.

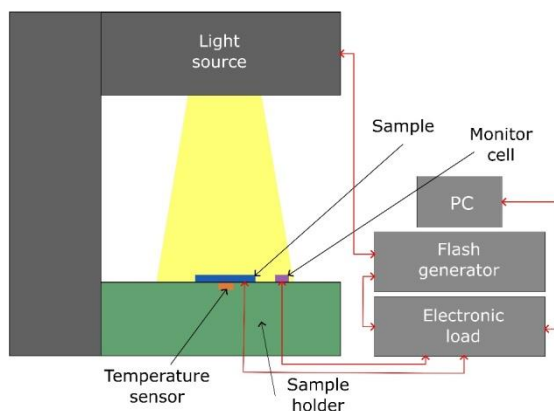


Figure 11. Schematic diagram of solar simulator with its main components: light source, sample holder, temperature sensor, electronic load, flash generator, PC, monitor cell.

Solar simulators are employed to simulate natural sunlight for repeatable and precise indoor testing of the J-V characteristics of PV cells or modules. This allows for the comparison of results obtained from different laboratories.

The J-V measurement involves varying the electrical load and measuring the resulting current with the light being turned on. In pulse simulators, the lamp is turned on at a specific moment when irradiance is closest to 1000 W/m². To determine this moment, a monitor cell is employed. This miniature cell is measured in a certified laboratory, and its current values are associated to irradiance levels. The typical light pulse duration for a pulse solar simulator is approximately 10 ms, requiring the measurement of the entire J-V curve within this interval (which is usually much shorter).

After the measurement irradiance and temperature compensation is performed on the obtained J-V curve. Then characteristic parameters are taken from the data or computed: J_{SC} (short circuit current density), V_{OC} (open circuit voltage), J_{MPP} (current density at maximum power point), V_{MPP} (voltage at maximum power point), P (power), FF (fill factor), η (efficiency), R_S (series resistance), R_{SH} (shunt resistance). Fill factor and efficiency are calculated as follows:

$$FF = \frac{J_{MPP}V_{MPP}}{J_{SC}V_{OC}}; \quad (52)$$

$$\eta = \frac{P}{P_{in}} \quad (53)$$

Here, P_{in} is the incoming power of irradiance (1000 W). R_S and R_{SH} can be calculated by fitting J-V curve with double diode equation [69]:

$$J = J_L + J_{01} \left(\exp\left(\frac{q(V - JR_S)}{kT}\right) - 1 \right) - J_{02} \left(\exp\left(\frac{q(V - JR_S)}{2kT}\right) - 1 \right) - \frac{V + JR_S}{R_{SH}} \quad (54)$$

3.6.3 Procedure for determination of Bragg reflector thickness

For each sol-gel solution used for metal oxide coatings for Bragg reflector structures, a relation between technological parameters of the dipping process and the resulting layer properties was needed for creating an optical filter with desired characteristics. For this, layers of single TiO₂ and SiO₂ were deposited at various speeds (40, 60, 80, and 100 mm/min.). Then, samples were firstly characterized by the spectrometer (reflectance measurements) and subsequently numerical simulation was used to approximate the latter reflection spectra in order to obtain sample thickness. Linear fitting was applied to obtain the required relationship between thickness and dipping speed data and is depicted in the Figure 12.

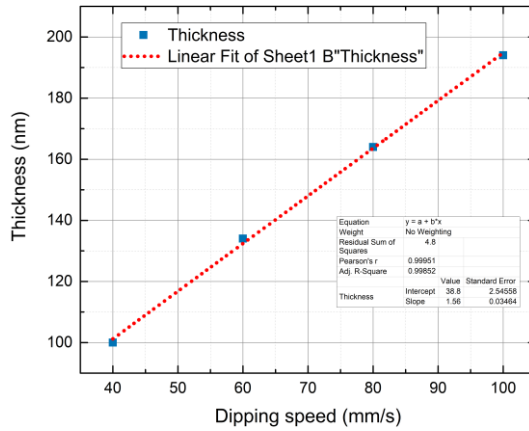


Figure 12. Example of fitting procedure to determine the correlation between dipping speed and the obtained layer thickness for SiO₂ solution.

3.6.4 Stylus profilometry (for ITO thickness determination)

ITO/Glass samples were characterized using a Dektak 150 Stylus profiler equipped with a stylus having a 5 μm tip with 45° angle.

Firstly, the sample is positioned on a high-precision stage and scan parameters: length, speed, accuracy (depending on measured object scale) and stylus force are selected in the software. When the scan routine is initiated, the tower assembly descends, making a contact between the stylus tip and the sample surface. Measurements are taken electromechanically, wherein the sample is moved beneath a diamond-tipped stylus. Within a constant force regime, a defined force is sustained through a feedback loop. As the stylus traverses the sample, any deviations in stylus position resulting from changes in surface morphology are detected via an optical mirror system.

4. FUNCTIONAL METAL OXIDE COATINGS FOR THE FORMATION OF DOUBLE LAYER ANTI-REFLECTIVE COATINGS ON PHOTOVOLTAIC STRUCTURES – THE EFFECT OF THICKNESS

In this section the results of coloring photovoltaic structures employing double layer anti-reflective coatings (DLARCs) formed by the deposition of ITO layer on the top of commercial multi-crystalline silicon solar cell are presented. Model simulation and experimental implementation were used for investigating the effect of thickness on the optical and electrical properties of the proposed structure using ITO/SiN_x:H DLARCs. Then, cells are characterized using a solar simulator and a spectrometer. Later, two different samples with 2 different colors were selected for testing their acceptability for use in solar panels. Finally, a detailed CIE colorimetry analysis is presented. Results of this section allowed to formulate the first defensive statement.

4.1 Simulation model (for ITO/SiN_x:H DLARCs)

Optical simulations were performed using a freeware optical simulation tool named “OPAL 2” made by “PV Lighthouse” [41,70]. Software described in more detail in section: “3.3 PV lighthouse simulation tool (for 1D optical simulations)”.

Structure under interest is depicted in Figure 13. It should be noted that electrical contacts were not accounted for simulations.

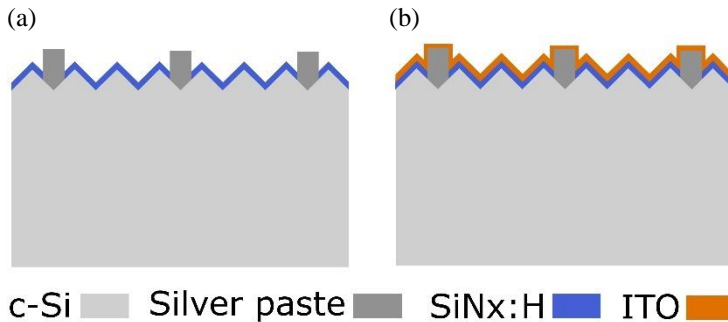


Figure 13. Double layer anti-reflective coating structure (b) formed on the top of the commercial silicon solar cell (a).

Simulation parameters were set like this:

- All layers were textured with upright random pyramids and characteristic angle of 54.74%;
- crystalline Silicon substrate thickness - 200 μm;
- AM1.5g solar spectrum;

- hydrogenated silicon nitride ($\text{SiN}_x\text{:H}$) is used as a first anti-reflective coating and its thickness is set to 80 nm with refractive index spectrum taken from Duttagupta et al. [71];
- ITO refractive index spectrum was taken from Holman et al. [72], deposited with magnetron sputtering. This index is named ITO4 (2.07 at 632nm).

4.2 Simulation: anti-reflective coating thickness on color (for ITO/ $\text{SiN}_x\text{:H}$ DLARCs)

Simulations in this section were performed to evaluate the effect of thickness on solar cell reflection characteristics.

As a first step, ITO4 thickness was varied and its effect on optical characteristics of solar cell was observed. Its values were changed from 0 to 200 nm in a step of 50 nm. Results are displayed in Figure 14.

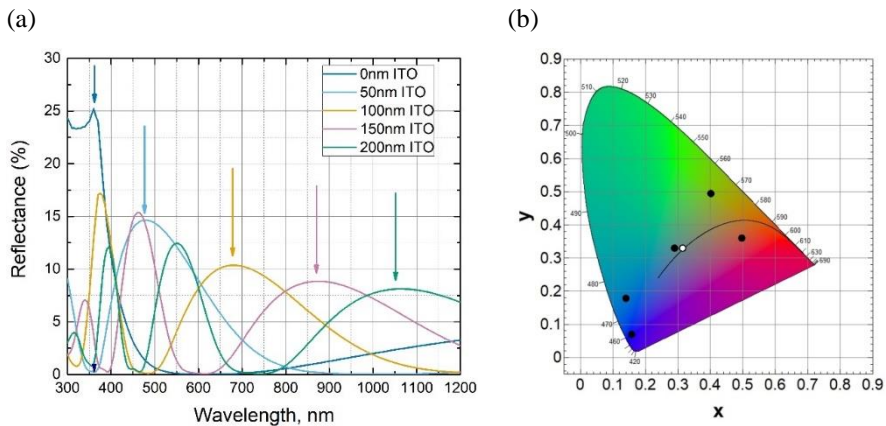


Figure 14. Reflectance characteristics of simulated solar cells with varying thickness of DLARC with ITO4 from 0 to 200 nm in a step of 50 nm (a). Representation of CIE coordinates (black circles) calculated from reflectance spectra with different ITO thicknesses. White dot – D65 illuminant [73].

A strong red shift of reflection maxima from around 350 to 1050 nm can be observed in the latter graph (a) with a change of ITO thickness from 0 to 200 nm, as shown with an arrow. Besides, multiple peaks appear with an increase in metal oxide thickness, making it 3 peaks for ITO thickness of 200 nm. Each of these peaks has a decreasing maxima height with an increase of its wavelength.

Variation of reflection characteristics can be directly associated to variation of human perception of color. For this, CIE parameters were calculated and depicted in CIE color space (Figure 14b). 5 points are shown with black dots, while with white dot the light source is marked (D65 illuminant [73]). Each of the points is separately located in a fin shaped CIE

space. It is evident that different colors can be obtained by easy variation of layer thickness. Specifically, these colors would be blue, greenish blue, green, greenish yellow, red. It could be concluded that intentional thickness variation of thickness of ITO allows modification of color of a photovoltaic device. As a next step, such structures were realized experimentally.

4.3 Sample preparation (magnetron sputtering)

RF magnetron sputtering was used for the deposition of thin ITO layers on Si based solar cells with standard $\text{SiN}_x\text{:H}$ ARC. The depositions were done at room temperature. For deposition RF magnetron power was $P=100$ W and the pressure of the process gas (Ar) in the deposition chamber was $p=5 \cdot 10^{-3}$ mbar. An ITO target with a diameter of 10 cm served as a sputtering source.

Multi-crystalline solar cells were utilized as substrates for ITO deposition in order to form DLARCs. For this purpose, M1 size solar cells with dimensions 157.5×157.5 mm, 4 busbars and efficiency of 18.4% were cut to 4 equal parts (78.38 mm x 78.38 mm), as illustrated in Figure 15. Thin white horizontal and thicker white vertical lines are silver paste contacts (fingers and busbars respectively).

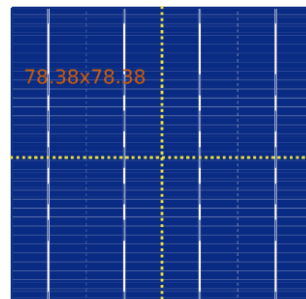


Figure 15. Commercial 18.4% polycrystalline solar cell with cutting track marked in yellow and resulting cell dimensions.

The deposition duration was systematically varied from 225 s to 2362.5 s, with increments of 112.5 s, to achieve ITO films with varying equidistant thicknesses. Along with the solar cell samples, glass pieces were placed for thickness determination (but not for all durations). The experimental correlation between the deposition duration and film thickness was established using a special calibration routine. The thickness of ITO layers in ITO/glass reference structures was measured using the Dektak 150 contact stylus profilometer. Then, the measured thickness was linearly fitted to generate the calibration diagram, as depicted in Figure 16. It should be noted that the deviations of thickness could be caused by the measurement accuracy of the stylus profiler or thickness deviations in films.

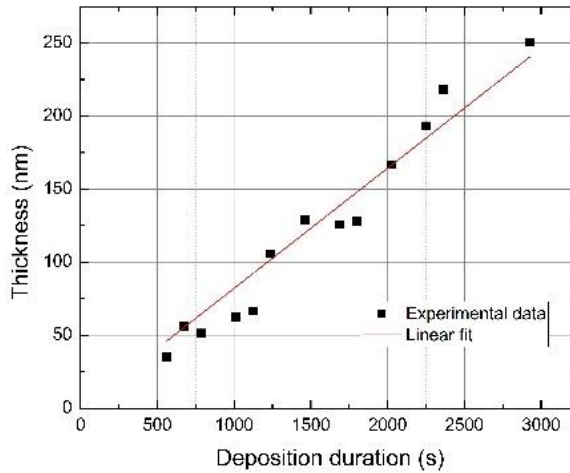


Figure 16. Measured (data points) and linearly fit (red line) data of ITO thickness dependence on the deposition time.

4.4 Experimental realization of ITO/SiN_x:H DLARCs

It was shown via simulations that an increase of ITO thickness affects solar cell visual appearance. Consequently, ITO layers were deposited by the magnetron sputtering with different thickness achieved by variation of deposition duration from 225 s to 2362.5 (with exceptional sample of 2918.9 s) to obtain different colored solar cells. In addition to deposition on multi-crystalline solar cells, ITO was also deposited on glass using the same deposition durations for ITO thickness determination.

In the Figure 17 an image with a typical series of samples with ITO/SiN_x DLARC formed on commercial multi-crystalline silicon solar cells is presented. Difference in thickness between adjacent samples in the series was approximately 9.25 nm, as determined by the calibration diagram in Figure 16. It should be noted that tenths or hundredths are only used for right scaling (9.25·21=194.5, while 9·21=189 nm), but not to describe the accuracy of thickness determination method. Bright and vivid color palette can be easily noticed by visual inspection. A gradual change of color from blue to green can be traced from upper left sample without any ITO to bottom 3rd from left (green) with 185nm of ITO. While the last sample – brown is exceptional with 240 nm of ITO. What is more, it is worth noting that color homogeneity is very high for all of the samples with relatively high surface area (78.38 mm x 78.38 mm).

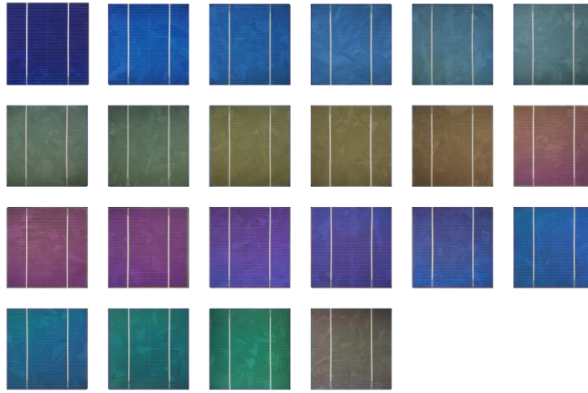


Figure 17. Colored multi-crystalline solar cells with increasing ITO DLARC thickness in steps of 9.25 nm from 18.5 till 194.25 nm (from top left blue sample row-wise till green). First sample is a reference one and the last one – brown is exceptional with 240.5 nm of ITO.

Electrical characteristics were measured for each cell utilizing an A class solar simulator, with the outcomes illustrated in Figure 18. Current density absolute and relative values are shown in part (a), while fill factor values are shown in (b) depending on ITO layer thickness. Each point is measured 3 times. Notably fill factor has huge deviations for different ITO thicknesses. Values range from around 67% to 77%. This suggested that either the measurement or ITO conductivity is not consistent with the varying functional oxide thickness. Therefore, current density and not efficiency was analyzed further in this section to avoid the influence of fill factor.

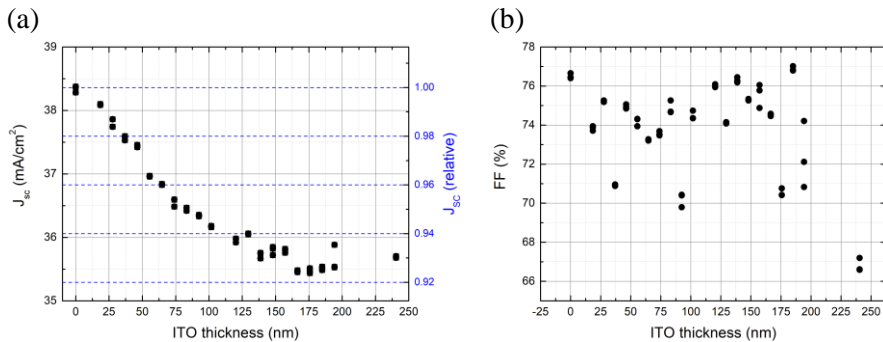


Figure 18. Short circuit current densities (a) and fill factors (b) of multi-crystalline solar cells with varying ITO thickness. Relative J_{sc} values are displayed in right Y axis of figure (a).

A gradual decrease in J_{sc} within an increase of ARC thickness can be noticed, while the lowest recorded value is nearly 8%. This is a relatively low loss, considering power loss of other coloring technologies (5-50%), what was described in 1. INTRODUCTION section. ITO thickness for the short circuit

current density minimum is around 175 nm. After the minimum value a slight increase in J_{SC} can be observed. This trend is in accordance to other works using different single or double layer anti-reflective coatings [5,8–10].

4.5 Solar module made using solar cells with ITO/SiN_x:H DLARC

In this section, acceptability of the proposed idea of DLARCs for PV panels is presented. Having in mind varying fill factor values, presented previously, new samples were produced while avoiding the deposition of ITO on silver paste contacts (using a special mask). For this, 6 new green cells were produced with a 184.5 nm thick ITO layer on top of the same commercial multi-crystalline solar cells. Using these green and reference blue cells two panels were manufactured and are illustrated in Figure 19. Sample without ITO is reference – blue colored. Layered material structure of laminated PV panel is demonstrated in Figure 20. Such structure contains: glass, ethylene-vinyl-acetate (EVA), solar cells, EVA, glass.



Figure 19. Glass/glass solar panels made using 6 green (185 nm ITO) and blue (0 nm ITO, reference) sequentially connected cells.

These mini panels were characterized using A+ class solar simulator, corresponding J-V curves are depicted in Figure 21 and extracted electrical parameters are listed in Table 2.

The results in Table 2 indicate an 8.83% difference in power between these two modules. In the green module, the power loss was primarily attributed to the short circuit current (I_{SC}) (-3.54%) and the reduction in fill factor (FF) (-4.73%), with only a minor impact on V_{OC} (-0.74%). This low influence on V_{OC} can be expected since the ITO deposition was performed without interference with the *pn* junction of the cell.

Furthermore, a decrease in shunt resistance of 17% is observed. This may indicate some current flow via the edges of the cell caused by the presence of a conductive ITO. This suggests improving the deposition process by adding a small frame around the cell for insulation of the cell edges before ITO deposition. Furthermore, the series resistance of the green solar module did not exhibit any improvement in charge collection with an increase in the conductive area. This could be attributed to the significantly lower conductivity of the ITO films compared to the cell busbars.

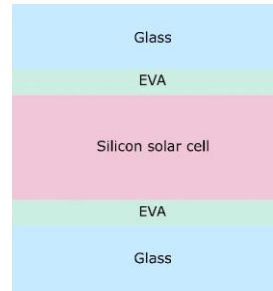


Figure 20. Layered material structure of laminated PV panel.

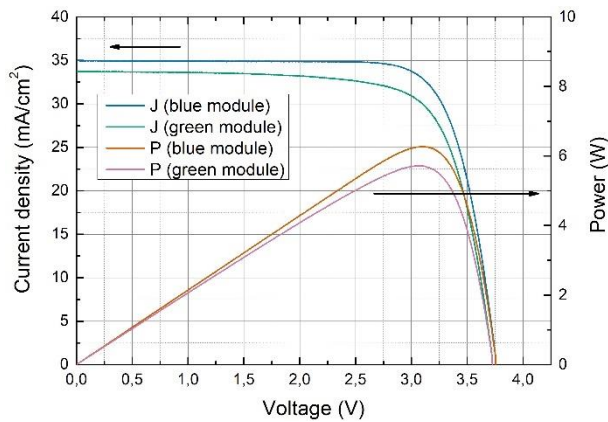


Figure 21. Measured J-V characteristics of blue and green module using solar cells with 0 and 185 nm ITO, respectively.

Table 2. Electrical parameters of blue and green mini modules extracted from J-V characteristics.

	V_{OC} , V	I_{SC} , A	V_{MAX} , V	I_{MAX} , A	P_{MAX} , W	FF, %	R_s , Ω	R_{SH} , Ω	Eff, %
Blue	3.77	2.15	3.10	2.03	6.27	77.6	0.18	345.6	17.19
Green	3.74	2.07	3.06	1.87	5.72	73.9	0.20	287.8	15.68
Δ , %	-0.74	-3.54	-1.10	-7.79	-8.83	-4.73	11.0	-16.72	-8.78

4.6 Colorimetric analysis of ITO/SiN_x:H DLARCs

Next, colorimetric analysis was performed in order to evaluate these characteristics and the possibility to use such solar cells in building integrated photovoltaics (BIPV). For this analysis only experimental reflectance spectra were used. The CIE diagram was drawn as a function of ITO thickness and is presented in Figure 22. A series of samples with increasing thickness of ITO films in the Double Layer Anti-Reflective Coating (DLARC) structures are

represented by a dotted line (connecting data points), traceable in the area around the white point (D65 illuminant). The sample without an ITO film is represented by a rectangle in the diagram (zero point), while the highest thickness value was indicated by the arrow (last point). Laminated and not laminated samples are connected with arrows (green arrow – green sample, blue – blue sample), photographs of these samples are shown in Figure 19.

Important thing to notice that the CIE diagram is designed in a way, that colors are purer further from the light source (marked as a white point with black outline) and are monochromatic in the edges of fin shaped CIE space, while near the white point they are the opposite.

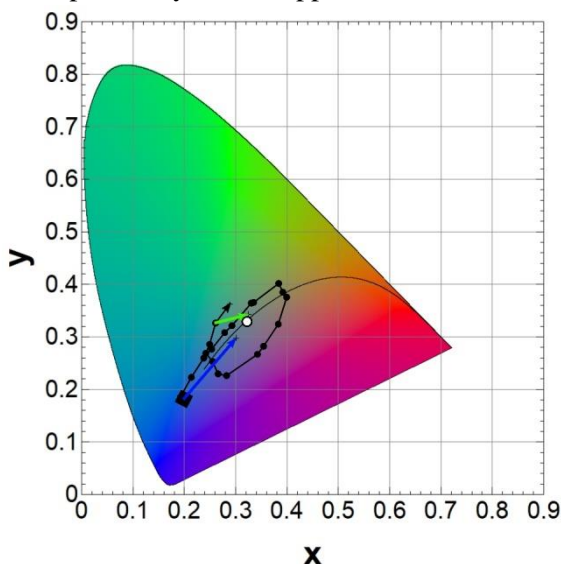


Figure 22. CIE diagram of colorimetry parameters calculated from experimental reflectance data of multi-crystalline SiNx:H/ITO DLARCs. Difference between color for non-encapsulated and encapsulated cells is shown by blue and green arrows for blue and green modules respectively. D65 illuminant is shown as a white point with black outline.

In Figure 22 it can be seen that all data points go in ellipse-like shape with hues changing from blue to purple and then again from blue to green (colors repeat). Points are getting closer and further from the white point meaning color purity is changing periodically. What is more, equidistant points (within deposition uncertainty) with different ITO thicknesses (with 9.25 nm between the adjacent samples) are not equidistant in CIE curve. They look a bit randomly distributed along the black line connecting those data points. What is more, data points for the laminated samples gets much closer

to the white point (D65 illuminant [73]) after lamination – meaning becoming less pure.

In order to compare these numbers numerically, color purity parameter was calculated using equation (16) according to CIE [74] (as described in section “2.6.1 CIE color space and its colorimetry parameters”).

In Figure 23, the color purity data is depicted. A periodic change of the latter parameter can be observed for DLARC-colored multi-crystalline solar cells, similarly to that seen in the CIE diagram. Purity values change from approximately 10 to 60%. Besides, as with the CIE diagram, a decrease in purity is evident in laminated samples. The loss is a bit higher for the blue panel and equals 82% and is around 71% for the green panel.

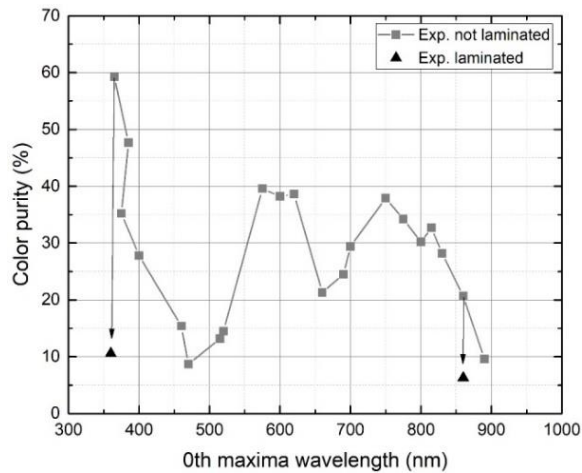


Figure 23. Color purity dependence on 0th order reflectance maxima position of reflectance spectra for experimental laminated (black) and not laminated (grey).

Additionally, in Figure 24, the reflectance spectra of laminated and non-laminated samples are shown. It can be noticed that after lamination, the height of reflectance maxima decreases, resulting in a flatter spectrum. This observation also explains the previous statement about purity. As theoretically, the highest purity would be for monochrome samples, flatter curves mean less pure.

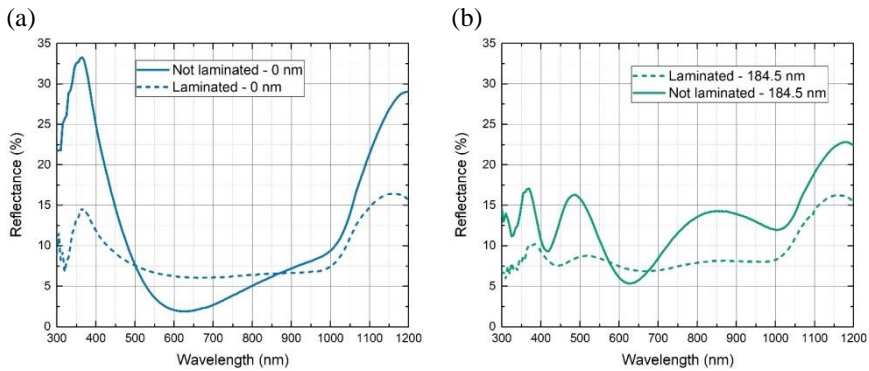


Figure 24. Comparison of reflectance spectra of laminated and non-laminated blue (a) and green (b) solar cells. Blue cells are with 0 nm of ITO and green are with 184.5 nm of ITO (according to the calibration diagram in Figure 16).

4.7 Summary

In the previous section, results of functional coatings made using indium doped tin oxide as a double layer anti-reflective coating for silicon solar cells are presented. Via optical simulations it was demonstrated that thickness variation of such or similar metal oxide red shifts reflectance spectrum also modifying its aesthetic appearance and color. Method was realized experimentally using commercial multi-crystalline solar cells, where ITO was deposited on the top of hydrogenated silicon nitride ($\text{SiN}_x\text{:H}$) anti-reflective coating with magnetron sputtering technique. A wide palette from blue to purple was obtained with high layer homogeneity. J-V measurements showed loss in short circuit current density up to 8%. As a next step, 2 mini panels using 2 types of samples (6 cells for each) were laminated to show the acceptability of the proposed technology for PV panels. Finally, colorimetric analysis was performed, and it was demonstrated that color purity changes periodically with the increasing thickness of metal oxide and it decreases almost twice after sample is laminated. Results indicate that such coatings could be used in BIPV, as a wide and homogeneous color palette was obtained with relatively low current density loss.

Results from this section allowed to formulate the first defensive statement.

First defensive statement. Thickness variation of ITO or similar metal oxide from 0 to 240 nm as a part of double layer anti-reflective coating formed on the top of the commercial silicon solar cell enables the adjustment of cell's color palette from blue to brown. This modification is associated with a relatively low current density loss of up to 8%, and post-lamination color purity decreases by 82% for blue and 71% for green PV panels.

5. FUNCTIONAL METAL OXIDE COATINGS FOR THE FORMATION OF DOUBLE LAYER ANTI-REFLECTIVE COATINGS ON PHOTOVOLTAIC STRUCTURES – THE EFFECT OF REFRACTIVE INDEX

The analysis performed in section 4 included only 1 parameter - ITO layer thickness - for double layer anti-reflective coatings (DLARC). This allowed to obtain different colored solar cells, however for the optimization of the structure second parameter is necessary – refractive index. Pour and Shafai, have demonstrated that the refractive index of ITO can be intentionally changed from $n = 1.69$ to $n = 2.1$ at 632 nm by the modification of the stoichiometry and the crystalline structure of the film [24].

Therefore, in this section previous work was extended to evaluate refractive index effect on efficiency and color of DLARC. In the first subsection some additional simulation details are presented. Then, firstly refractive index effect on current and then on color are analyzed. Finally, all results are summarized, and a second defensive statement is stated.

5.1 Simulation details (for ITO/SiN_x:H DLARCs)

For optical simulations same tool “OPAL 2” from PV Lighthouse [41,70] was used as in the previous section, with same parameters except for some additional ITO refractive indexes added. Software described in more detail in section: “3.3 PV lighthouse simulation tool (for 1D optical simulations)”.

Refractive indexes of SiN_x:H and all ITO’s spectra are detailed in Table 3 and depicted in Figure 25. ITO refractive indexes were selected according to the work by Pour and Shafai [24], who demonstrated that the refractive index of ITO can be intentionally changed from $n = 1.69$ to $n = 2.1$ at 632 nm by the modification of the stoichiometry and the crystallinity of the film. Therefore, selection was done trying to cover the range of these indexes (1.73-2.07 at 632 nm).

Table 3. ITO’s refractive index data and references.

Name	Refractive index*	Deposition technique	Reference
ITO1	1.73	magnetron sputtering	Holman et al. [72]
ITO2	1.8	magnetron sputtering	Holman et al. [72]
ITO3	1.87	commercial	Moerland and Hoogenboom [75]
ITO4	2.07	magnetron sputtering	Holman et al. [72]

* - Refractive index at 632 nm

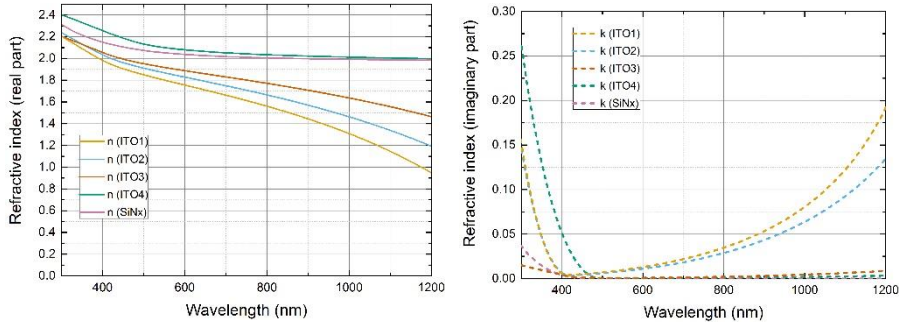


Figure 25. Real (a) and imaginary part (b) of refractive index spectrum of $\text{SiN}_x\text{:H}$ (pink) and 4 ITO: ITO1 (1.73 at 632 nm), ITO2 (1.8 at 632 nm), ITO3 (1.87 at 632 nm), ITO4 (2.07 at 632nm) [72,75].

5.2 Simulation results (for ITO/ $\text{SiN}_x\text{:H}$ DLARCs)

Two distinct thicknesses of Indium Tin Oxide (ITO) were selected to calculate the refractive index impact on the reflection characteristics of the solar cell: 100 and 200 nm. The corresponding spectra are presented in Figure 26.

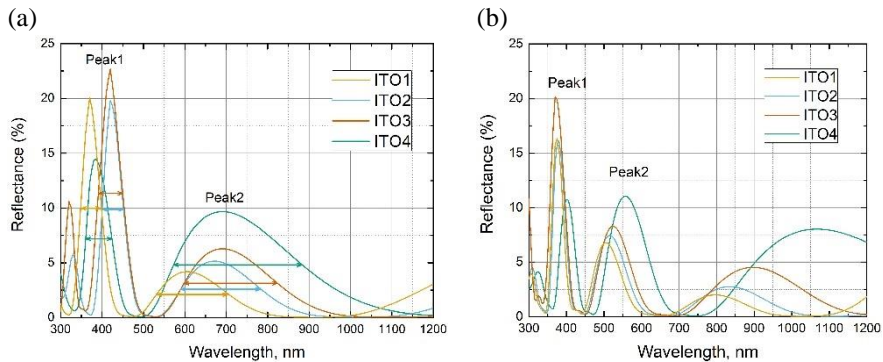


Figure 26. Simulated reflection characteristics for DLARC structures formed using different ITOs with 100 (a) and 200 nm (b) thicknesses.

In the latter figure it can be clearly seen that there is a shift of reflection peak named peak2 in respect to its wavelength. For the higher refractive index spectra peaks2 are red shifted compared to the lower refractive index spectra. In case of 100 nm ITO, the shift for peak2 from ITO4 to ITO1 is around 85 nm, while in case of 200 nm ITO DLARC it is around 50 nm. This peak can be expected to result in color deviations, to be discussed further in the text. Full width at half maxima (FWHM) were computed for two peaks (shown in the Figure 26) of all structures. Results are listed in

Table 4.

Table 4. Full width at half maxima of peak1 and peak2 of reflection spectra calculated for ITO1, ITO2, ITO3 and ITO4 with thicknesses 100 and 200 nm.

	FWHM for 100 nm ITO		FWHM for 200 nm ITO	
	Peak1	Peak2	Peak1	Peak2
<u>SiN_x:H/ITO1</u>	49.9	175.5	33.6	81.3
<u>SiN_x:H/ITO2</u>	51.15	185.12	35.7	86.38
<u>SiN_x:H/ITO3</u>	59.13	225.05	42.27	92.13
<u>SiN_x:H/ITO4</u>	63.22	309.27	45.15	110.6

It is evident that spectra with lower refractive index can be associated with lower FWHM values. For 100 nm thick structure FWHM values vary from 50 to around 63.2 for peak1 and from 175.5 to 309.3 for peak2 increasing for increasing refractive index values. While for 200 nm thick ITO double layer anti-reflective coating FWHM of peak1 varies from 33.6 to 45.2 and for peak2 from 81.3 to 110.6 also increasing for increasing refractive index values. Besides, lower reflectance maxima height is obtained for lower refractive index spectra for peak2. Although, no clear tendency is visible for peak1 related to maxima height. In the next section the effect of these differences on color will be analyzed.

5.3 Colorimetric analysis (for ITO/SiN_x:H DLARCs)

For the colorimetric analysis, DLARC thickness was varied from 0 to 210 nm for 4 different ITO's refractive index spectra. Then CIE parameters (xyY) were calculated for all these reflectance spectra.

When comparing the simulation results in Figure 27, it can be inferred that available color hues for the different ITO/SiN_x:H DLARCs are very similar. Although, here is a small shift of all ellipse-like shape (made of connected data points) towards lower part (reddish, purple) of fin shaped CIE space, when changing ITO refractive index spectrum from lower to higher (ITO1 < ITO2 < ITO3 < ITO4). In the case of color relation to thickness, there is a higher difference between the samples. The last point of curve is marked with an arrow, where the sample with ITO1 would result in green color, while the sample with ITO4 would result in yellowish color. In terms of 0th order maxima this results in a 300 nm shift.

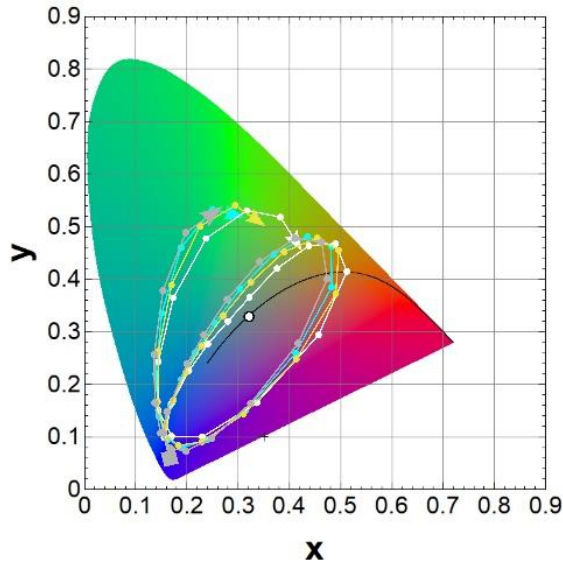


Figure 27. CIE diagram of colorimetry parameters calculated from simulated reflectance spectra of $\text{SiN}_x\text{:H/ITO1}$ (grey), $\text{SiN}_x\text{:H/ITO2}$ (light blue), $\text{SiN}_x\text{:H/ITO3}$ (yellow) and $\text{SiN}_x\text{:H/ITO4}$ (white) DLARC's (a). D65 illuminant is shown as a white point with black outline.

This data was converted to sRGB scale to compare colors visually and is depicted in Figure 28. 4 different sRGB scales for 4 different ITO refractive indexes with varying ITO thickness are displayed in this graph. The lowest spectrum represents ITO1 and then they go up numerically increasing to the uppermost being ITO4. x axis is discrete, built in 10 nm steps. Note: all graphs are made a little lighter (25% transparent on white background) for a clearer view and comparison.

Notably, the colors appear quite similar, as deduced from the CIE graph earlier (Figure 27). A slightly higher color clarity could be identified for the upper spectrum (ITO4) compared to the lower (ITO1). Additionally, a noticeable shift in hues is observed depending on the thickness of the ARC. The bottommost picture with structure employing ITO1, exhibits a green hue with a thickness of around 200-210 nm, whereas the uppermost with ITO4 shows a green hue with a thickness of around 180 nm, indicating a difference of 20-30 nm. Furthermore, in contrast to the preceding paragraph, it is noteworthy that ITO4, with a 210 nm thick ITO layer, results in a brownish color rather than a yellowish one.

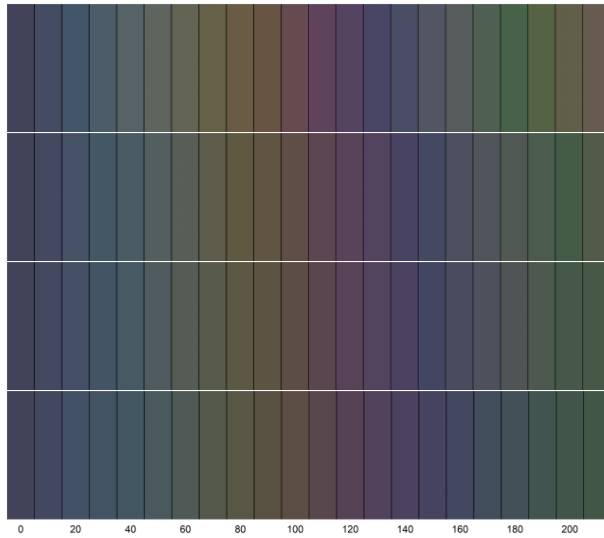


Figure 28. sRGB representation of tristimulus XYZ values for different thickness ITO's with different refractive indexes (from the bottom): ITO1, ITO2, ITO3 and ITO4. Note: all graphs are made a little lighter (25% transparent on white background) for a clearer view and comparison.

Subsequently, colors were further compared through the tristimulus parameter Y, also known as brightness. The graph illustrating various DLARC structures with varying thicknesses for different ITO layers is presented in Figure 29. A notable trend is visible, where color brightness undergoes periodic changes for all structures. Significantly ITO4, with the highest refractive index spectra values has the highest tristimulus parameter Y values and all other ITO's have decreasingly lower brightness with ITO1 being the lowest. This observed trend aligns with the reflectance spectra depicted in Figure 26, where the reflectance maxima height (and average reflectance) is the highest for ITO4 and the lowest for ITO1. Additionally, a small shift in peak position is discernible between the different data sets.

Similarly, as previously in section "4.", color purity was calculated for all of the samples. In Figure 30 this parameter is depicted from 0th order reflection maxima. When increasing ITO thickness in steps of 10 nm till 210 nm thickness color purity periodically changes for all of the curves, similarly as it can be seen in CIE diagram (Figure 27), were points of ellipse-like shape get nearer and further away from the white point (D65 illuminant). Purity values change from around 5 to around 90%. This change is wider compared to the experimental sample purity depicted in Figure 23, where the range was from approximately 10 to 60%. These deviations may rise because of complex morphology of multi-crystalline solar cells, which are made by acid etching.

While, for the simulations inverted pyramid structure was used. Besides, surface morphology could have also been modified after depositions of ITO.

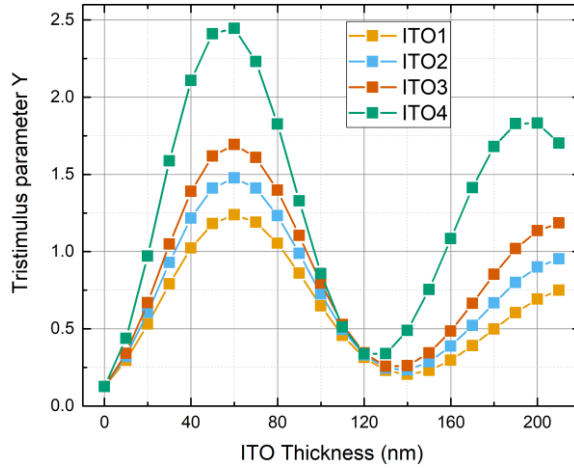


Figure 29. The dependence of tristimulus parameter Y from the DLARC thickness using different ITO refractive index spectra.

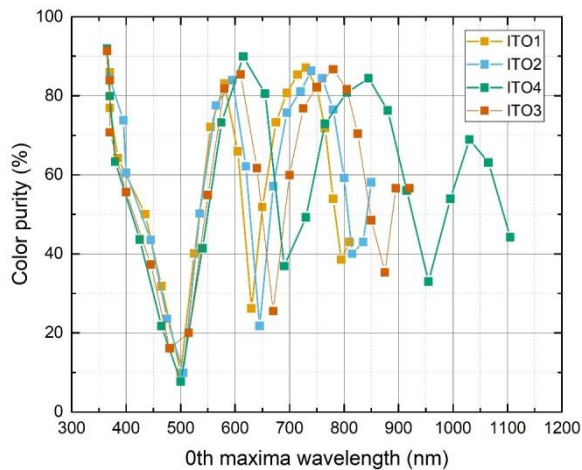


Figure 30. Color purity dependence on 0th order of reflectance maxima position for simulated reflectance spectra of SiN_x:H/ITO1 (orange), SiN_x:H/ITO2 (light blue), SiN_x:H/ITO3 (red) and SiN_x:H/ITO4 (green) DLARC's (a).

5.3 Summary (for ITO/SiN_x:H DLARCs)

In the latter section solar cell coloring technique employing double layer anti-reflective coatings formed on the commercial silicon solar cells was

extended using optical simulations. The effect of refractive index spectra on optical characteristics of photovoltaic device was analyzed. For this, 4 refractive index spectra of ITO were used.

It was determined that a lower refractive index (1.8 at 632 nm) contributes to narrower and blue-shifted reflection peaks in the reflectance spectra, as compared to ITO films with a higher refractive index (2.07 at 632nm). Nevertheless, these reflectance spectra yield similar available hues for different refractive indices of metal oxide, albeit with slight color shifts. For instance, a 210 nm thick ITO sample would exhibit a green color when the refractive index is lower (1.8 at 632 nm), while for the sample with a higher ITO refractive index (2.07 at 632 nm), it would result in a brownish color.

This allowed to form a second defensive statement.

Second defensive statement. Tuning the refractive index of ITO used in double layer anti-reflective coatings of silicon solar cells on the top of SiN_x:H produces lower, blue-shifted and narrower reflection peaks in the surface reflection spectrum when the ITO refractive index is lower (1.8 at 632 nm) compared to a higher refractive index (2.07 at 632 nm). This leads to comparable hues and color purity and a higher color brightness for higher ITO refractive index.

6. FUNCTIONAL METAL OXIDE COATINGS FOR THE FORMATION OF BRAGG REFLECTOR STRUCTURES FOR PHOTOVOLTAIC CELLS

In this section a different coloring technique will be presented using so-called Bragg reflectors. These structures consist of periodic stacks of high and low refractive index materials tuned to reflect or transmit certain wavelengths of incoming light spectrum. Compared to the previous coloring technique, this one could be deposited on glass, this way extending the colored area from solar cell to whole glass surface and making it more aesthetically pleasing. Besides, higher reflectance maxima and therefore higher brightness could be expected for these structures, this way improving their visual appearance.

Firstly, in this section, optical simulations using transfer matrix method were used to determine the optimal structure for the desired characteristics of the filter. Then, experimental implementation of the multilayered structure using dip coating technique from sol-gel solutions was implemented. Later, the applicability of the proposed structures for solar panels was demonstrated. Finally, colorimetric properties were calculated and compared, and a third defensive statement formed.

6.1 Simulation model

The multilayered structure of interest is depicted in the Figure 31, featuring varying number of $\text{TiO}_2/\text{SiO}_2$ periods. Here only lower u values are considered ($u = 1.5, 2, 2.5, 3$), for the experimental simplicity and scalability of the technology. TiO_2 here is considered as a high refractive index material and SiO_2 – as low. In order to find out the optimal structure, different numbers of layers must be compared.

Reflectivity at a maximum position is one of the most important parameters in filters of this nature. Boxuan et al. formulated an equation for the calculation of this parameter for the stack of thin films undergoing periodic changes, each characterized by a distinct refractive index. By replicating a few of these films within the periodic structure, the formula allows for the calculation of the reflection maximum [12]:



Figure 31. 1D photonic crystal structure on a glass substrate.

$$R = \left(\frac{1 - n_s/n_a (n_{hi}/n_{lo})^{2u}}{1 + n_s/n_a (n_{hi}/n_{lo})^{2u}} \right)^2, \quad (55)$$

here, u represents the number of films within the structure, while n_s , n_a , n_{hi} , and n_{lo} denote the refractive indexes for the substrate, surrounding substance (typically air, as in this case), high-index material, and low-index material, respectively. It is essential to note that this equation is applicable solely to structures with an even number of layers. Therefore, using (55) reflectivity was calculated for even number of periods ($u=2$, and $u=3$).

Reflection characteristics of the stacks with an uneven number of metal oxide layers were calculated using the Abeles transfer matrix method [76]. In the transfer matrix method, each layer and interface in the structure are represented as a 2×2 matrix, where electromagnetic wave amplitude and phase characteristics are included. For thick films, such as glass, the phase is omitted to account for the limited coherence length, typically less than $30 \mu\text{m}$ [44], as glass is a few mm thick. The implementation of this method involved the use of the Python programming language and the package developed by Steven J. Byrnes [63]. Using transfer matrix method reflectance spectra were calculated for the 3 and 5 layered structures (for $u=1.5$ and 2.5) on the glass substrate according to the classical Bragg 's condition:

$$\frac{\lambda_0}{4} = nd. \quad (56)$$

Where λ_0 – is the wavelength of the maxima position, n – refractive index, d – thickness. Each layer of the multilayered structure was tuned for the same λ_0 .

Using simulated light reflection characteristics, short circuit density could be calculated allowing to evaluate the effect of color on solar cell efficiency. In Figure 32 the IQE spectrum of a reference commercial silicon solar cell with 20.0% efficiency is shown. The short circuit density loss, derived from the reflectance spectra, was computed using a Python tool developed by P. Malhotra et al. [77]. J_{sc} was determined using the formula:

$$J_{sc} = -q \int_{\lambda_1}^{\lambda_2} R(\lambda) \cdot IQE(\lambda) \cdot \phi_{ph,\lambda} d\lambda, \quad (57)$$

$$\phi_{ph,\lambda} = S(\lambda)(AM1.5G) \frac{\lambda}{hc}, \quad (58)$$

where $\phi_{ph,\lambda}$ is the photon flux (photons/s·m²) (AM1.5G solar spectrum), $IQE(\lambda)$ – internal quantum efficiency, $R(\lambda)$ – reflectance, $S(\lambda)$ – power density (W/m²).

6.2 Simulation results

Digital simulation reflectance spectra are depicted in Figure 33 (a), alongside curves generated from equation (55) for u values of 1, 1.5, 2, 2.5, and 3. $u=1.5$ and $u=2.5$, represented by short dashes, are drawn to clearly illustrate the values in between integer u values. Notably, the reflectance maxima values for 5 layers vary from around 75 to 65% and for 3 layers – from 54 to 44%. Besides, it is observed that using only 3 layers yields a similar effect to having 4 layers, and similarly, the effect of 5 layers is comparable to 6. The difference is only from 2 to 4% (absolute). This suggests that an uneven number of layers could be preferred having in mind that it would be cheaper and easier to realize technologically, while resulting optical characteristics are almost identical. The trend of maxima position decreasing with increasing wavelength is associated with the ratio of low and high refractive index materials, as illustrated in Figure 33 (b).

In addition to optical parameters, the impact of modification of reflectance spectra (or color) on the electrical parameters of a model solar cell was evaluated within the digital model analysis. To achieve this, J_{SC} loss was computed for 3 and 5-layered structures using transfer matrix method with varying positions of reflectance maxima, employing equation (57) from the preceding section. The IQE spectrum of a reference commercial silicon solar cell with 20.0% efficiency, used in these calculations, is illustrated in Figure 32.

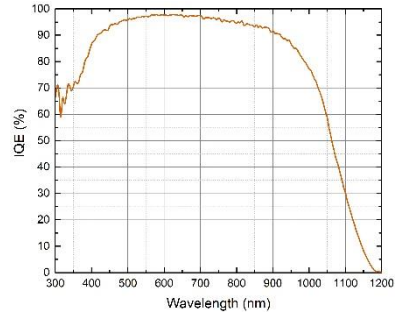


Figure 32. IQE spectra of REF mono cell used in calculations of J_{SC} with efficiency of 20.0%.

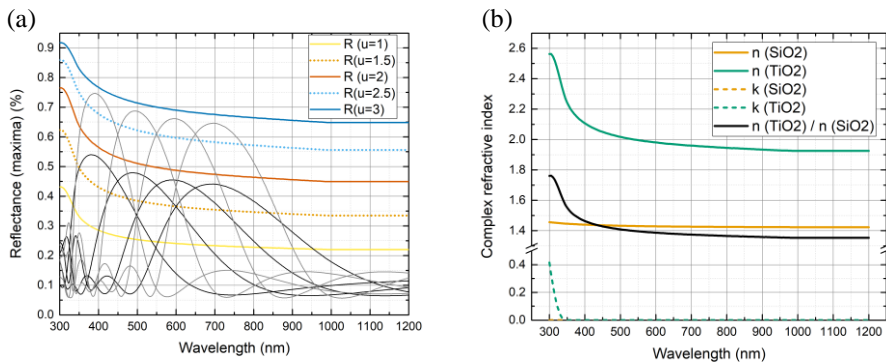


Figure 33. In section (a), the dependence of reflectance maxima values on wavelength is illustrated based on formula (55) with different u values, depicted by colored curves. Simulated reflectance curves using transfer matrix method for a 3 and 5 layered stack are represented by black and grey curves respectively. In section

(b), complex refractive index data measured with ellipsometry for both metal oxides is presented, with the black curve representing the ratio between the high (TiO₂) and low (SiO₂) refractive index materials.

Table 5. Calculated short-circuit current density values using the reflectance spectra of Bragg reflector structures having 3 or 5 layers of metal oxides. REF represents values calculated for blue solar cell with its IQE spectra shown in Figure 32. The percentage loss in J_{SC} is computed in relation to mono Si IQE J_{SC}.

Maxima wavelength (λ_0)	400 nm	500 nm	600 nm	700 nm	REF*
J_{SC} loss, mA/cm ² (3 layers)	6.31	8.98	10.67	12.35	39.06
J_{SC} loss, mA/cm ² (5 layers)	7.14	10.43	12.11	12.97	39.06
J_{SC} loss, % (3 layers)	-16.14	-22.99	-27.32	-31.62	-
J_{SC} loss, % (5 layers)	-18.29	-26.70	-31.00	-33.20	-

* - Mono Si IQE

It is evident that the overall loss in short-circuit current is notably high for both structures, ranging from 6.3 to 13 mA/cm². This results in a relative loss of J_{SC} for reference solar cells, varying from 16% to 33%. Such relative currents would correspond to an approximate 15.4% to 19.3% absolute efficiency for solar cells with a 23% efficiency, which is around the current market average. These values exhibit a higher upper limit compared to commercial colored solar cells, which typically range between 15.8% and 17.8% [78]. Besides, the difference in J_{SC} loss between 3 and 5-layered structures is comparatively moderate, ranging from 4% to 9.5% relative to the current density of the reference monocrystalline silicon cell.

The comprehensive analysis of the periodic structure of multilayer thin films indicates a simple solution for the technological implementation of the proposed method. It was determined that employing only three films of SiO₂ and TiO₂ (TiO₂/SiO₂/SiO₂) can be both sufficient and efficient for intentionally modifying the surface color of silicon solar cells. The conclusion significantly simplifies the sequence of the technological procedures required for experimental realization using sol-gel dip coating technique.

6.3 Sample production

The sol-gel solution for the TiO₂ material was prepared using a titanium butoxide (TBOT) precursor, HCl, H₂O, and ethanol in molar concentrations of 1:1:0.2:23 (respectively). The mixture was then stirred for 1 hour and left to age for 24 hours before application. Similarly, for the SiO₂ sol-gel solution, a tetraethyl orthosilicate (TEOS) precursor was used, HCl and ethanol in molar concentrations of 1:0.00022:12 (respectively). Concentration of the HCl used was 37%. The TEOS solution underwent mixing for 1 hour at 60 °C and was subsequently cooled to room temperature.

Bragg reflector structures were fabricated using 5x5 cm glass substrates and dip coating technique: a method where the glass substrate was dipped vertically into the solution at a constant speed. The back surface of the substrate was isolated with tape to prevent deposition on both sides. The layers were then deposited and dried at 45°C for 15 minutes (after each layer), followed by annealing at 110°C for 2 hours (only after all 3 layers are deposited), according to the results from Langlet et al. [79].

PERC mono silicon solar cells of size 2.5x2.5 cm were used for mini solar panels. The structure of the latter panels is like this (from the bottom): backsheet, EVA encapsulant, solar cell, EVA encapsulant, Bragg lattice structure, and glass.

6.4 Experimental realization of Bragg reflector structure

Based on the outcomes of the theoretical analysis in section 2, model samples of optical filters were produced and examined in this section using sol-gel dipping technique. In line with the model calculations, stacks consisting of only 3 layers were experimentally investigated with structure shown in Figure 34. Intentional change of deposition speed (and therefore layer thickness) allowed to obtain 6 different colors. Thicknesses were set according to the Bragg's condition in equation (56) for the primary reflectance maxima positions at wavelengths $\lambda_0 = 454, 534, 621, 701, 766,$ and 810. Each model sample was manufactured as a single rectangular glass plate with dimensions of 5x5 cm².

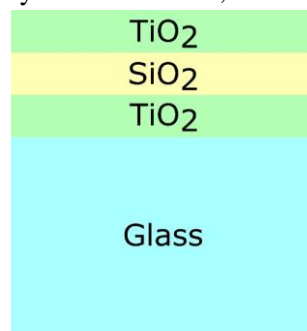


Figure 34. Optimized Bragg reflector structure on glass substrate: TiO₂, SiO₂, TiO₂.

A set of six experimental samples is depicted in Figure 35. It is evident through visual inspection that high color brightness and homogeneity across a relatively large surface area are present in the samples. The observed color sequence from blue to purple was obtained through an increase of layer thickness of the multilayered structure. This shift is visually traceable from left to right and from top to bottom in Figure 35. Different colors can be distinguished (from upper left row-wise): blue, greenish, yellowish, orange, peach and purple. In the corners of samples some inhomogeneities are visible, that are thought to be caused by different velocities of flowing sol-gel solutions.

It is worth noting that moiré patterns are slightly visible in some samples, however they are not considered significant for the research and are thus not analyzed in this work.

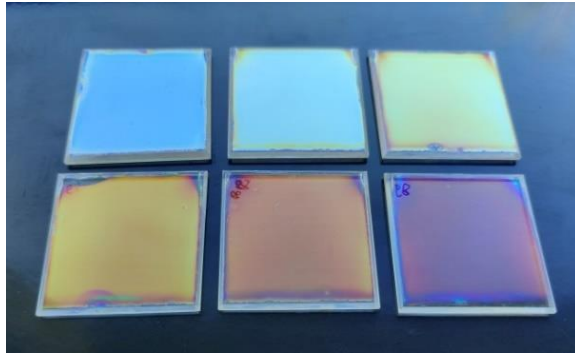


Figure 35. A set of 6 experimental samples with varying layer thicknesses according to the Bragg 's condition for the reflectance maxima positions at $\lambda_0 = 454, 534, 621, 701, 766, \text{ and } 810 \text{ nm}$.

Firstly, samples were characterized by optical spectrometer to illustrate the dependence of the optical characteristics on the thickness of the layers. Results are shown in the Figure 36. In the latter figure, the redshift of reflectance maxima (λ_0 values) is clearly visible for the different samples, transitioning from light blue to orange visual appearance perceived by an eye. Besides, a decrease in the height of this maxima with an increase in wavelength is also distinguishable in the samples. This trend can be associated to lowering of $\text{TiO}_2/\text{SiO}_2$ ratio with increasing wavelengths (Figure 33 (b)), what was also observed from simulation results shown in Figure 33 (b).

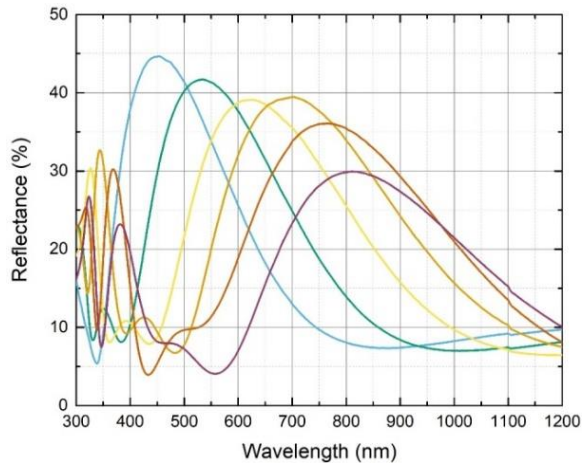


Figure 36. Experimentally measured reflectance spectra of 6 different colored 5x5 glass plates shown in Figure 35: light blue, greenish, yellowish, orange, peach, purple.

The feasibility of the technology to produce the intended structure was investigated through scanning electron microscopy (SEM) analysis. It also

allowed to examine the structure and morphology of the samples. A representative SEM photograph of the cross-section area is presented in Figure 37 for the sample optimized for the reflection maximum at $\lambda_0 = 621$ nm. It illustrates a three-layered structure with distinct interfaces and relatively high uniformity across the layer thickness. Granular structures were observed in the metal oxide layers, with brighter regions indicating the presence of elements with a higher atomic number (TiO_2), and vice versa (SiO_2).

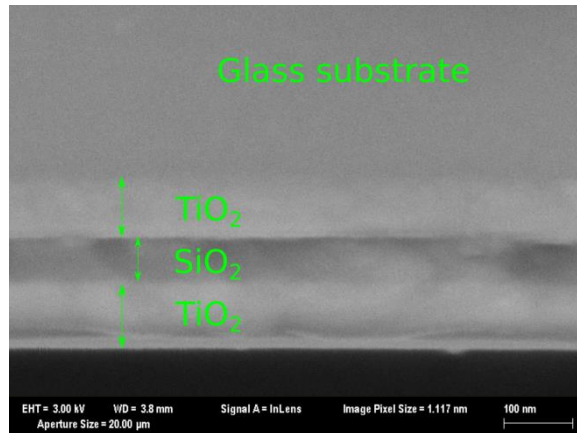


Figure 37. SEM photograph of the cross-section area for one of the colored glass samples (greenish) captured using a secondary electron detector. The glass substrate is depicted at the top, while the layered structure is visible in the bottom part of the photograph.

6.5 Feasibility of the technology for mini-PV panels

The feasibility of applying the method in PV module technology was demonstrated by making colored mini modules. Most common encapsulant material ethylene vinyl acetate (EVA) [80] was used for these PV panels. Bragg reflector structure was laminated in the inside part of the panel as it is shown in the Figure 38. It's important to note that the colored glass samples utilized for these mini panels have similar, though not identical, λ_0 values compared to those used in the section “6.4 Experimental realization of Bragg reflector structure”. The assembled panels from this study were compared to the modules

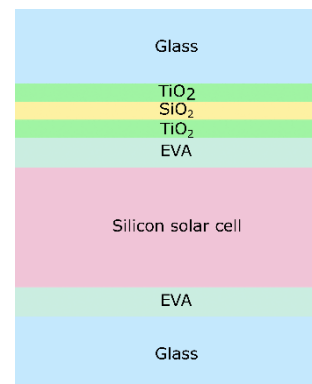


Figure 38. Structure of laminated colored mini panels.

produced using commercial-colored solar cells. Figure 39 illustrates the new panels (a) alongside solar panels made with colored commercial solar cells (b).

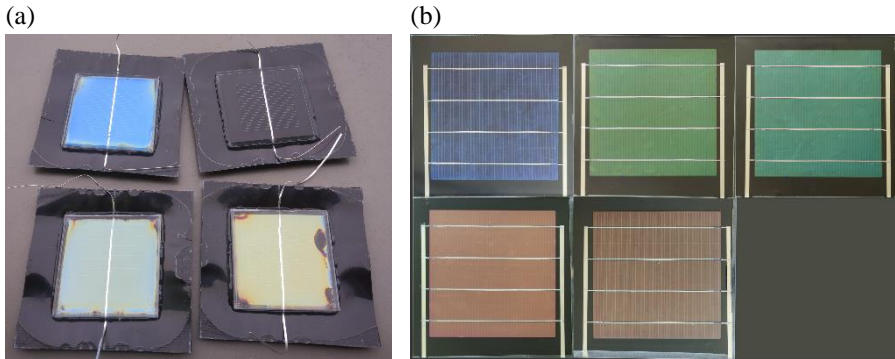


Figure 39. Visual comparison between two types of colored PV-cells: (a) mini panels made with Bragg reflector-coated colored glass plates (from left: black-REF, light blue, greenish, and yellowish) (counter-clockwise) and (b) panels made using commercial solar cells [78].

Samples were characterized using an A+ class solar simulator. The J-V characteristics for the modules are depicted in Figure 40, and the extracted parameters are listed in Table 6.

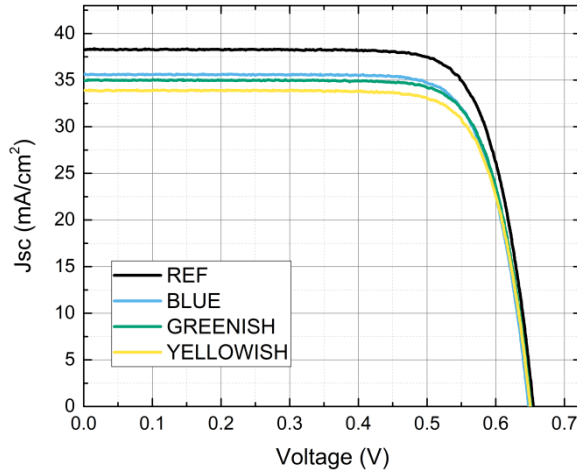


Figure 40. J-V characteristics of laminated colored PV mini panels.

The efficiencies of the mini panels were determined to be as follows: 18.75% (REF, black), 17.2% (light blue), 17.13% (greenish), and 16.52% (yellowish), with a relative difference in short circuit current density of 7.13%, 8.67%, and 11.47% (compared to the REF), respectively. In contrast, colored panels made with colored commercial solar cells exhibited efficiencies ranging from 13% to 18.4%. These are similar efficiencies, while Bragg

reflector ones being a little more effective. However it is important to note that the efficiencies of colored panels with the propose coloring technique could be higher, as any cells could be used for these panels and currently 23-25% efficient cells are mainstream in the market [11]. Replacement of REF solar cell from 18.75 to 24% would result in significant increase of efficiency (approximately 21.1-22%).

Table 6. Electrical characteristics of laminated colored PV mini panels obtained from J-V characteristics.

Parameters	REF, black	light blue	greenish	yellowish
J _{sc} , mA	38.28	35.55	34.96	33.89
V _{oc} , V	0.655	0.648	0.652	0.651
Efficiency, %	18.75	17.28	17.13	16.52
FF, %	77.09	77.21	77.46	77.27
P, W	0.198	0.182	0.181	0.174
ΔJ _{sc} (%)	-	-7.13	-8.67	-11.47

6.6 Colorimetric analysis: CIE diagrams

Quantitative assessment of the generated colors holds significance for the application of colored glass plates in the field of Building-Integrated Photovoltaics (BIPV). To achieve this, CIE colorimetry analysis was employed. Besides, for a meaningful colorimetric analysis, a comparison with competitive colored structures is essential, therefore same panels made with commercial colored solar cells were utilized [78].

Colorimetric parameters (x, y, Y, color excitation purity) were calculated for 3 groups of samples: (a) Bragg reflector structures on glass (not laminated), (b) in PV mini panels (laminated), and (c) the laminated commercial solar cells. The xy data is visually represented in the CIE color space, as illustrated in Figure 41, providing a basis for comparing color attributes between these structures.

The lowest thickness is indicated by the rectangular point, and each next point is connected with dashed lines until the thickest sample is reached. Yellow and cyan colored data represent samples for the non-laminated and laminated glasses with Bragg reflector structures, respectively. Notably, there is no apparent distinction between these datasets. However, in comparison to panels with commercial solar cells (white), purer colors are evident for the multilayered structures, as the points are farther from the white point (D65 illuminant – average midday light).

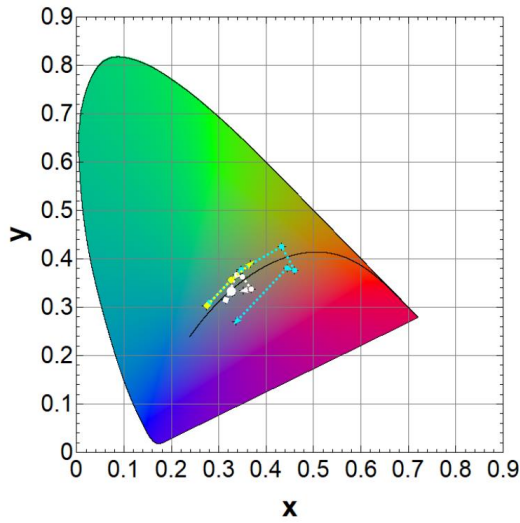


Figure 41. CIE diagrams of 3-layered Bragg reflector structures before lamination (cyan), after lamination with solar cells (yellow), and of panels made with commercial solar cells (white) [78].

For a quantitative comparison, Tristimulus parameter Y and color purity dependence on the 0th order reflectance maxima position for all 3 cases mentioned previously are presented in Figure 42 (a and b, respectively). A notable difference is observed for the Y parameter, which characterizes sample color brightness. The non-laminated Bragg reflector exhibits significantly higher values compared to both other cases. Moreover, after lamination, the brightness decreases, but it remains much higher (from 2 to 3 times) than for the panels with commercial solar cells.

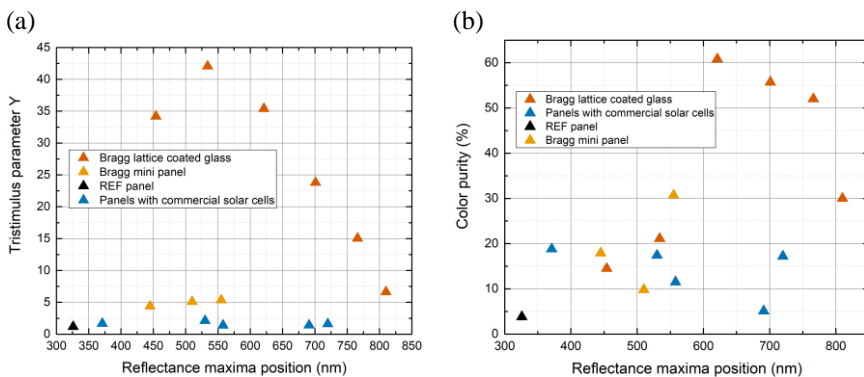


Figure 42. Dependence of tristimulus parameter Y (a) and color purity (b) on the 0th order reflectance maxima position. Non-laminated Bragg reflector-coated glass samples are represented in red, laminated ones in orange, and panels with colored commercial solar cells in blue. The REF sample is depicted in black.

The analysis of the colored model panels revealed no correlation between the color purity distribution and the reflectance maxima position in lower wavelengths (up to 600 nm). However, significantly higher color purity was observed for the non-laminated glass plates compared to the panels with commercial solar cells at higher wavelengths. A similar trend is visible in the CIE diagram in Figure 41.

6.7 Sensitivity of color to the deviations in refractive index and thickness

The sensitivity of the technological process to color is of high importance for the future scalability and commercial realization of the proposed technology. To address this, two essential parameters, namely thickness and refractive index, were selected, as their modification can be achieved intentionally through variations in experimental deposition conditions or randomly (deposition uncertainties). Color differences were calculated using a parameter defined by the CIE International Standard in CIELAB color space: ΔE [61], described in more detail in section 2.4.2

For the calculations, refractive index values of ± 0.05 and ± 0.1 were selected for both metal oxides (SiO_2 and TiO_2). Thickness values were chosen from $\pm 0.15\%$ to $\pm 0.01\%$ relative to the overall structure thickness for 3 different variations: 1) single outer TiO_2 layer thickness, 2) thickness of both TiO_2 layers, 3) and thickness of SiO_2 layer. ΔE was calculated for all the data for the color difference threshold detection. Along with the parameter ΔE , sRGB representation of XYZ was calculated for the visual comparison.

The calculated data for the variations in refractive index are presented in Table 7. ΔE values range approximately from 8.4 to 9.9 for deviations of ± 0.1 and from 4.3 to 5.3 for deviations of ± 0.05 . These results indicate that TiO_2 has a greater influence on ΔE compared to SiO_2 . Besides, the reduction in the difference between high and low refractive index materials also results in higher ΔE values. Based on the classification detailed at section 2.4.2, all of these deviations in refractive index result in colors which should be visually distinguishable. This observation is supported by the comparison of data in the sRGB in the same table. Consequently, it can be inferred that in order for these differences to be imperceptible to the observer, the discrepancies in refractive index spectra must be controlled to be less than ± 0.05 .

Table 7. Calculated ΔE data for the refractive index variations and representation of color differences in the sRGB colors.

Sample	ΔE (CIE2000)	Color TEST/REF (sRGB)
$n_{SiO_2}-0.1$	8.8612	
$n_{SiO_2}-0.05$	4.6292	
$n_{SiO_2}+0.1$	8.4435	
$n_{SiO_2}+0.05$	4.2791	
$n_{TiO_2}+0.1$	9.8243	
$n_{TiO_2}+0.05$	4.793	
$n_{TiO_2}-0.1$	9.876	
$n_{TiO_2}-0.05$	5.296	

Next, the impact of deviations in thickness on color was investigated from the optimal case of the Bragg condition. The results are presented in Table 8 and graphically represented in Figure 43.

Table 8. Calculated ΔE data dependency from thickness variations from the optimal case of the Bragg condition for three variables: SiO_2 , outer TiO_2 , both TiO_2 layers and color comparison in the sRGB.

Δd^*	Variable: outer TiO_2		Variable: SiO_2		Variable: both TiO_2	
	ΔE	Color TEST/REF (sRGB)	ΔE	Color TEST/REF (sRGB)	ΔE	Color TEST/REF (sRGB)
-15%	38.1		29.7		33.6	
-10%	27.3		21.2		24.1	
-5%	15.7		11.8		13.2	
-2%	7.6		5.7		6.2	
-1%	4.5		3.6		3.8	
1%	3.0		2.0		2.2	
2%	6.6		4.1		4.4	
5%	18.5		11.4		12.2	
10%	29.8		20.4		22.7	
15%	31.8		21.7		28.7	

Δd^* - deviations in thickness with respect to the overall thickness of the 3 layered structures.

The resulting ΔE varies from approximately 2 to 38, depending on changes in thickness relative to the overall structure thickness, denoted as

Δd . Notably, ΔE is lower for positive Δd than for negative Δd . Another noticeable trend is that sensitivity (across the entire range of Δd) is lowest for changes in the thickness of SiO_2 , somewhat higher for changes in the thickness of both TiO_2 layers, and the highest for the outer TiO_2 layer (similar trend observed with refractive index). Difficulty in distinguishing colors from the optimal case (referred to as REF) arises when Δd is $\leq 1\%$, resulting in ΔE ranging from 2 to 4.5. Therefore, it could be concluded that careful control of thickness must be kept for the technological process to keep undesired deviations in color invisible.

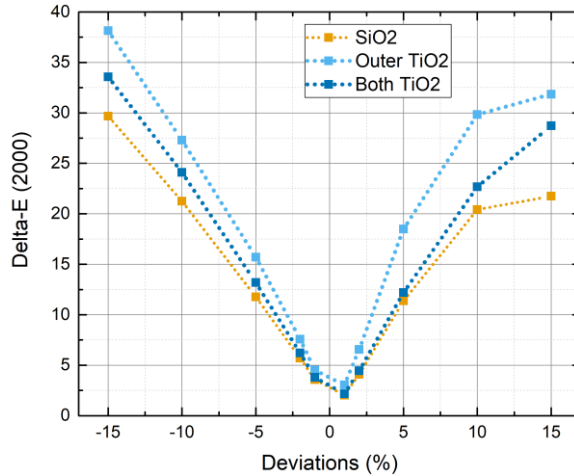


Figure 43. Calculated ΔE data dependency from thickness variations from the optimal case of the Bragg condition for three variables: SiO_2 (orange), outer TiO_2 (light blue), both TiO_2 (dark blue) layers.

6.8 Scalability of the technology

Fundamental and experimental results from this section allows to upscale the proposed technology. This continuation of this work will be shortly summarized in this sub-section.

To scale up the proposed technology, specialized equipment was created based on dipping technique. Samples of dimensions 20x20 cm were coated with triple-layered structures, similarly to the 5x5 samples detailed earlier in this section. Subsequently, the coated glass pieces were laminated with a membrane laminator, incorporating solar cells to construct mini-photovoltaic (PV) panels. The outcomes are depicted in Figure 44. The top three samples were laminated with flat glass (the uppermost being the reference, without coatings), while the bottom sample was made using textured glass (with coatings applied to the flat side and laminated internally within the panel). It is noteworthy that on

the bottommost sample, busbars were black coated to achieve a seamless result. Vivid colors and bright colors can be visible in the photograph, although some enhancement in homogeneity could be advantageous.

Obtained from J-V characteristics, the efficiency loss of such panels (from top, excluding REF) is: 14.47%, 15.22%, 7.28% relative to the reference.

Some details about commercial coloring technologies that were developed by several companies during the years of this PhD should be detailed here for the comparison. One of them involves colored sheets, from Solaxess [81]. These sheets can be laminated similarly as solar panels without them, just ethylene vinyl acetate (EVA) needs to be in both sides of this sheet. Power loss ranging from 10 to 45%, depending on the color, is declared by



Figure 44. Upscaled 20x20 cm size mini panels with multilayered 1D photonic structures (from the top): black (REF), greenish, purple, light blue (textured glass, painted busbars – a seamless solution).

the producers. Some other coloring technologies were developed on glass. Kromatix, for instance, has created colored glass with transmittance values ranging from 13 to 18% (only transmittance is stated) [82] and JSXQ developed colored glass solutions with power loss ranging from 15 to 35% for different colors [83].

The presented technologies have similar or higher loss compared to the results shown in this paragraph. Therefore, the proposed technology is considered competitive for BIPV market.

6.9 Summary

In the preceding section, another coloring technique was presented using the so-known Bragg reflectors. For this, TiO_2 and SiO_2 metal oxides were employed. Layer thicknesses were set according to the Bragg lattice condition to obtain highest reflectance maxima height.

In the initial phase, simulations were performed to optimize parameters for achieving the desired characteristics. Firstly, it was demonstrated that the reflectance spectra could be red shifted by increasing the thickness of metal oxides, allowing to obtain different colors. Additionally, it was revealed that an odd number of layers produces a similar effect, in terms of reflectance maxima height, as an even number of layers when glass serves as the substrate,

and a high refractive index material is the first layer on glass, following a high/low refractive index sequence. Consequently, further analysis focused on uneven structures comprising 3 and 5 layers. Simple simulations revealed loss ranging from 16% to 33% for such structures, with a difference of 4% to 9.5% between 3 and 5 layers. As a result, it was concluded that a 3-layered structure is both sufficient and efficient for deployment in the photovoltaic field, considering the associated technological challenges.

Subsequently, six 3-layered structures were fabricated on glass using a sol-gel dip coating technique, with various thicknesses to obtain six distinct colors. The suitability for solar panels was affirmed through lamination with solar cells, causing an efficiency loss ranging from approximately 7% to 11.5%. This is a bit lower, but similar to DLARC coating loss up to 8%, obtained earlier.

Next, a colorimetric analysis was performed, leading to 2-3 times higher color brightness compared to DLARC coatings shown in two previous sections.

Finally, susceptibility of color to refractive index and thickness was evaluated to be average. Values of refractive index and thickness must be kept below ± 0.05 and ± 2 (respectively) for color to be indistinguishable by eye. Therefore, careful attention should be taken for the technological process optimization.

These results allowed to formulate a third defensive statement.

Third defensive statement. Optimal design of Bragg reflector structure for coloring of solar panels using TiO_2 and SiO_2 metal oxides consists of only 3 layers formed on the glass substrate (glass/ TiO_2 / SiO_2 / TiO_2) and results in 2-3 times higher brightness compared to the panels with colored commercial solar cells. The tolerable technological deviations from the color related numbers to be indistinguishable by human eye are ± 0.05 for the refractive index spectrum and less than approximately $\pm 2\%$ for the thickness.

7. FUNCTIONAL COATINGS FOR COLORING OF TANDEM CELLS: DIGITAL MODEL CALCULATIONS

In line with the development of PV technologies in industry and lab research, coloring of a tandem solar cell seemed like an essential continuation of the previous results of this work. Therefore, in this section, the coloring of multi-junction solar cells is explored through simulations employing a kesterite-silicon monolithic tandem solar cell. It should be noted, that in the article, where these results were published, optimization of such tandem device was also investigated. For clarity and context, a summary of the optimization is presented at the beginning of this section and then attention will be focused to the variation of anti-reflective coating thickness of Al_2O_3 metal oxide and its consequential effects on the electrical and optical properties of the structure.

7.1 Simulation methodology

Simulations for such analysis were employed using a combination of the transfer matrix method (TMM) and SCAPS software. The former was employed for optical simulations, utilizing a Python package developed by Steven J. Byrnes [63] (similarly as in previous sections). Meanwhile, SCAPS is a freeware 1D solar cell electrical simulation software developed at the Department of Electronics and Information Systems (ELIS) of the University of Gent, Ghent, Belgium [64]. Detailed descriptions of both methodologies can be found in the respective sections: “3.1 Transfer matrix method (for 1D optical simulations)” and “3.2 SCAPS software (for 1D electrical simulations)”.

Tandem solar cell simulations in SCAPS are limited to 7 layers. Consequently, both sub-cells were simulated independently electrically using SCAPS, while optically, the entire structure was simulated simultaneously.

Simulation was performed in the following five steps:

1. Generation of a mesh file for TMM for both sub-cells using SCAPS script (for distance data points in x axis);
2. Calculation of reflectance and absorbance using TMM in each of the layers of the multilayered structure (using mesh file);
3. Calculation of carrier generation profile for each layer of sub-cells using python script written by the author of this work (described in section 3.5);
4. Generation of J–V curves by running SCAPS script for both sub-cells;

5. Combination of two J–V curves of kesterite and silicon sub-cells and calculation of characteristic parameters (eff, J_{SC} – short circuit current density, etc.) using special script written by the author of this work.

Assumptions used in simulations:

- No texture is present, layers are flat;
- Light is coming perpendicular to the surface;
- Each layer's properties are homogeneous inside and changing stepwise when moving from one layer to another;
- Carrier generation was calculated using eq. (48) from section 3.5 with exponential decay. However, in reality, light is transmitted and reflected multiple times in a multi-layered structure, therefore full absorption could be only ensured using the normalization of carrier generation profile integral to the absorption integral (described in 3.5 section and calculated using (51)). This assumption is thought to have minimal impact on the results.
- Tandem J-V was obtained by adding J-V curves of both sub-cells. However, in most cases this results in an incomplete J-V curve with the missing low voltages from J_{SC} and up, depending on the current mismatch level (except the current matching conditions). To obtain the full J-V curve, missing points of tandem J-V were obtained by linear approximation of 3% of the lowest data points.
- J_{SC} loss was calculated from the eq. (44) assuming an ideal EQE, because of the limitation in SCAPS (SCAPS does not provide EQE, when carrier generation profile is imported, not generated inside of the software);
- Thick layers like glass, EVA and Silicon were treated as incoherent (phase is dropped out) in TMM calculations as coherence length is usually less than 30 μm in films [44]. This is thought to be negligible to the results.
- Flat bands are assumed in SCAPS at interfaces with contacts.
- Calculation of carrier generation profile for silicon REF cell was performed using eq. (45) from section 3.5. Absorbance was obtained: $A(\lambda) = 1 - R(\lambda)$, where reflectance was taken from Maryam Valiei et al. [6] (transmittance is 0). This was the case, as silicon cells are already very well developed in the industry, and it is not possible to obtain good light trapping without the presence of the texture and precise replication of cell structure.

- Only SRH recombination was considered in this work (Auger and band-to-band not).
- Besides, it should be noted, that alternatively MoO₃ can be used as a tunnel junction for such a tandem device that also creates a blocking layer for atom diffusion during the sulfurization/selenization at 450-550 °C of the top sub-cell. However, due to the limitations in SCAPS of maximum of 7 layers, this was not realized. Therefore, an ideal junction was considered in this work.

7.2 Setting the tandem cell simulation parameters

Main material properties for the simulation were taken from the relevant literature and are listed in the Table 9.

Table 9. Parameters used for electrical simulation part with SCAPS. References: M. D. Haque et al. [84], S. Khelifi et al. [85], D. Mora-Herrera et al. [86], Muhammad Rashid et al. [87], F. Jafarzadeh et al. [88], A. Jimenez-Arguijo et al. [38].

Param.	MoSe ₂ ²⁴	CZGSe ¹⁴	CdS ¹⁴	ZnO _{0.2} S _{0.8} ²⁵	ZnO ¹⁴	ITO ²⁶	Si (bulk) ¹³
d (μm)	0.02	1.45	0.050	0.050	0.050	0.200	200
E _g (eV)	1.29	1.5	2.4	3.07 ¹²	3.3	3.65	1.12
χ (eV)	4.2	4.41 ^{**}	4.2	4.3 ¹²	4.4	4.8	4.5
ε (relative)	13.6	6.950 ¹²	8.28 ¹²	9	7.8 ¹²	8.9	11.9
μ _n (cm ² /V·s)	100	100	100	100	100	10	150
μ _p (cm ² /V·s)	25	20	25	25	25	10	45
N _d (cm ⁻³)	-	-	10 ¹⁷	3.93 · 10 ¹⁸	10 ¹⁸	10 ¹⁹	-
N _a (cm ⁻³)	2.25 · 10 ^{15*}	10 ^{14*}	-	-	-	-	3 · 10 ¹⁵
CB eDOS (1/cm ³)	2.2 · 10 ¹⁸	1.9 · 10 ¹⁸	3.1 · 10 ¹⁸	2.2 · 10 ¹⁸	3.6 · 10 ¹⁸	5.2 · 10 ¹⁸	2.8 · 10 ¹⁹
VB eDOS (1/cm ³)	1.8 · 10 ¹⁹	1.5 · 10 ¹⁹	1.4 · 10 ¹⁹	1.8 · 10 ¹⁹	1.1 · 10 ¹⁹	1.8 · 10 ¹⁸	1.04 · 10 ¹⁹
electron v _{th} (cm/s)	2.2 · 10 ⁷	(2.7 · 10 ⁷) ¹²	(2.3 · 10 ⁷) ¹²	10 ⁷	(2.2 · 10 ⁷) ¹²	10 ⁷	10 ⁷
hole v _{th} (cm/s)	1.5 · 10 ⁷	(1.3 · 10 ⁷) ¹²	(1.4 · 10 ⁷) ¹²	10 ⁷	(1.5 · 10 ⁷) ¹²	10 ⁷	10 ⁷

* - set during approximation of reference cell for the IV characteristics.

** - for CZGS_xSe_{1-x} band gap and electron affinities were changed according to the S. Khelifi et al. [85]: 1.52, 1.688, 1.86, 2.05 eV and 4.41, 4.242, 4.074, 3.91 eV (respectively). Other parameters kept the same as for CZGSe.

Refractive indexes for CZGS_xSe were taken from theoretical calculations (DFT) from Kesheng Shen et al. [36] and are depicted in Figure 45 (a), as no experimental data is yet available. Refractive index data of other layers is shown in Figure 45 (b).

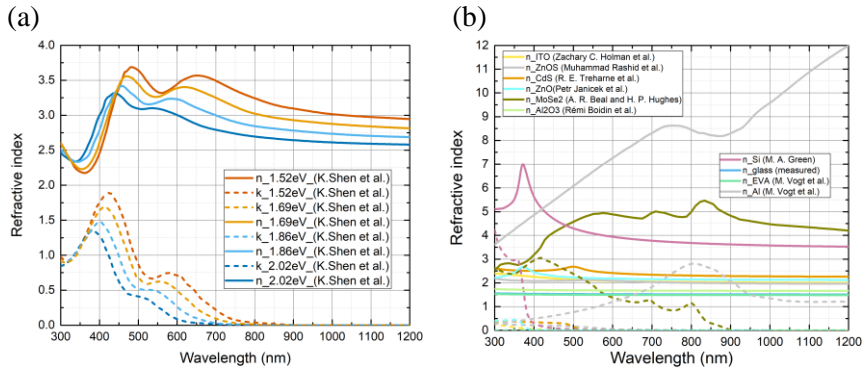


Figure 45. Refractive indexes of $\text{Cu}_2\text{ZnGe}(\text{S}_x\text{Se}_{1-x})_4$ solid solutions with different anions ratio (a) [36] and other layers that were used in simulations (b): ITO (yellow)(n conc: $2 \cdot 10^{20} \text{cm}^{-3}$) [72], $\text{ZnO}_{0.25}\text{S}_{0.75}$ (light grey) [89], CdS (orange) [90], ZnO (clear sky blue) [91], MoSe_2 (brown) [92], Si (purple) [93], glass (blue)(measured), EVA (green) [94], Al_2O_3 (aquamarine)[95], Al grey) [96].

The selection of the kesterite REF device was based on two main criteria: the highest efficiency achieved by previously reported pure germanium kesterite devices in the literature, and band gap compatibility with available refractive index spectra data ($\text{CZGSe } E_g = 1.45 \text{ eV}$). Consequently, a solar cell from I. Anefnaf et al. [97] with an efficiency of 6.5% and a band gap of 1.52 eV was chosen for this study (Figure 46a).

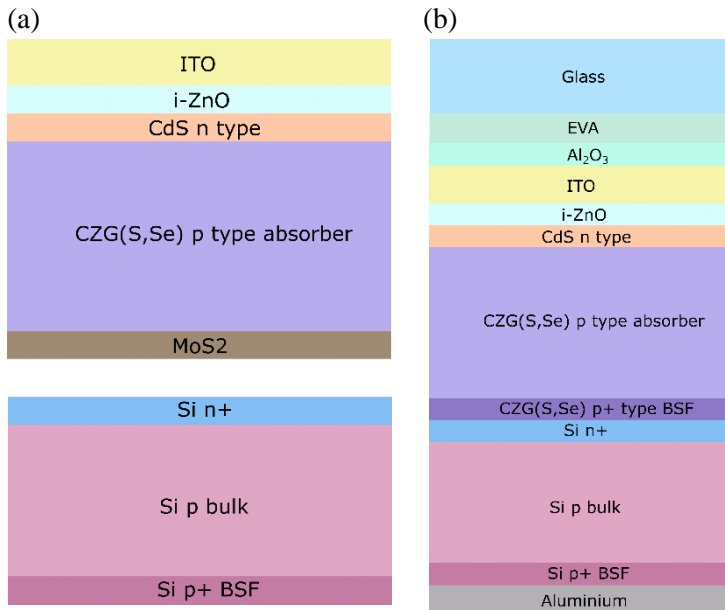


Figure 46. Simulated tandem solar cell structures: baseline REF cells (a) and the optimized 2T tandem structure (b).

For the silicon REF device, one of the top-performing high-area solar cells with a 24.0% efficiency was selected, manufactured by LONGi [37] (Figure 46a).

Optimized tandem device is shown in Figure 46b, to be detailed later in the text.

Parameters of both real and SCAPS devices are listed in the Table 10.

Table 10. Comparison of REF cell parameters to SCAPS cells (Simulated as separate cells, not in a tandem).

	J_{sc} , mA/cm ²	V_{oc} , mV	Eff., %	FF, %	τ , s*	Source:
REF CZGSe cell	17.8	606	6.5	60	?	[97]
My REF CZGSe cell in SCAPS	17.9	606	6.4	58.5	1.1×10^{-11}	
REF Silicon cell**	41.6	694	24.0	83.3	?	[98]
My REF Silicon cell in SCAPS	41.5	694	24.0	83.2	$1 \times 10^{-3***}$	

* - Effective minority carrier lifetime at absorber layer.

** - REF Silicon cell was taken from M. Green efficiency tables 61 from page 4, table 2 [37]: „LONGi, p-type PERC”,

*** - selected according to the silicon lifetimes in the literature [99].

To accurately mimic the J-V characteristics of the experimental reference devices with the virtual SCAPS devices, the parameters of both sub cells were adjusted to obtain the best curve fit (Figure 47). This was achieved with the following set of values: N_a (CZGSe) = 10^{14} cm⁻³, N_t (CZGSe) = $3.3 \cdot 10^{17}$ cm⁻³, N_a (MoSe₂) = $2 \cdot 10^{15}$ cm⁻³, N_t (MoSe₂) = 10^{18} cm⁻³, resulting in an effective lifetime (τ) of the kesterite absorber at $1.1 \cdot 10^{-11}$ s. Some other parameters were assigned to these values: the interface recombination velocity between the kesterite absorber and the buffer layer (CdS) was set to 10^5 cm/s and the electron and hole capture cross-sections were set at 10^{-14} cm². The energy level, relative to the reference, was fixed at 0.6, with the defect type considered neutral. These parameters were set as initial ones for the kesterite solar cell and remained unchanged throughout the optimization steps outlined below unless explicitly stated otherwise.

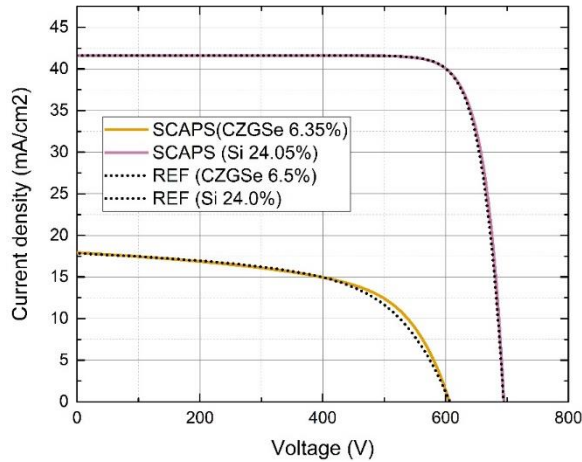


Figure 47. Experimental J-V curves of real references devices (black dotted lines) and simulated ones (colored continuous lines).

7.3 Monolithic Kesterite/Silicon tandem optimization (in brief)

The following steps were selected for the optimization of kesterite/silicon tandem device (detailed characteristics of stepwise improvement and J_{SC} loss are listed in

Table 11 and Table 12, respectively):

- 1) Encapsulation added (2 mm glass + 470 μm EVA) for the more realistic representation solar cell (mini solar panel). A slight increase in efficiency was obtained from 10.21 to 10.41%.
- 2) MoSe_2 was removed to reduce parasitic absorption (due to the low bandgap of MoSe_2) and p+ increased acceptor doping area (called “back surface field” (BSF)) was added to the kesterite absorber. A significant increase in efficiency was observed from 10.4 to 14.6%.
- 3) An attempt to change CdS by ZnOS was made to reduce parasitic light absorption due to the low bandgap of CdS. It resulted in a decline in efficiency from 14.6 to 14.46%. Consequently, for subsequent steps, CdS was retained as it outperformed ZnOS.
- 4) CZGSe’s base doping increased from 10^{14} to 10^{16} according to S. Khelifi [85] and interface recombination velocity (at CdS/CZGSe interface) decreased from 10^5 to 10^3 cm/s. This slightly increased solar cell efficiency from 14.6 to 15.09%.
- 5) Requirements for improvement of kesterite crystal quality were set at this step with the variation of CZGSe’s effective carrier lifetime. It should be noted that kesterite absorber was accessed by an effective carrier lifetime in the bulk, representing the complex

crystal quality of kesterite through a single parameter. This approach is supported by T. Unold's findings, which demonstrate a strong correlation between this parameter and the record efficiencies achieved in thin film solar cells [100]. Notably, the highest increase in efficiency was observed for lifetime increased till 11 ns, what is 1 order higher than in REF or in record devices in the literature [101–103]. Tandem efficiency increased from 15.09 to 16.91%.

- 6) CZGSe thickness and band gap (by partial substitution of Se with S) are varied to find current matching conditions. These conditions were found with CZG(S_xSe_{1-x}) (with x=0.5) having a band gap of 1.86 eV with kesterite thickness of 1.65 μm and resulting tandem efficiency of 28.05%. In the latter position efficiencies of each of sub-cells are as follows: 19.65% for kesterite and 8.72% for silicon. It is noteworthy that used values of the thickness and of the band gap can be easily obtained experimentally. Thus relatively good control of the layer thickness is feasible for any deposition techniques in the whole range of 0.5 – 2.0 μm, while increase of band gap can be easily achieved by partial substitution of Se by S, which was previously shown to be beneficial and led to record devices for kesterite technology [104,105].
- 7) Al₂O₃ anti-reflective coating was added, and its thickness was optimized. Color effect on current matching and efficiency on the tandem device was analyzed. Described in detail in the next section. Here final efficiency of 28.63 was obtained, 0.61% higher than in previous step.

Table 11. Main electrical characteristics calculated from J-V curve of stepwise improvement of monolithic Si/kesterite tandem device.

Step	CZGSSe				Silicon			
	Voc, V	Jsc, mA/cm ²	Eff, %	FF, %	Voc, V	Jsc, mA/cm ²	Eff, %	FF, %
0	0.606	17.56	6.17	58.0	0.655	9.7	5.14	80.91
1	0.608	18.38	6.46	57.8	0.655	9.86	5.22	80.97
2	0.842	19.74	11.44	68.82	0.659	11.12	5.9	80.62
3	0.842	18.38	10.61	68.6	0.659	11.07	5.88	80.6
4	0.877	19.19	13.56	80.61	0.659	11.12	5.9	80.62
5	1.037	22.09	20.23	88.34	0.659	11.12	5.9	80.62
6	1.293	16.69	19.09	88.49	0.671	16.82	8.97	79.47
7	1.293	17.09	19.56	88.54	0.671	17.07	9.11	79.52

Step	Tandem			
	V _{oc} , V	J _{sc} , mA/cm ²	Eff, %	FF, %
0	1.259	9.83	10.21	82.54
1	1.26	9.99	10.41	82.71
2	1.499	11.31	14.6	86.1
3	1.497	11.26	14.46	85.77
4	1.534	11.32	15.09	86.92
5	1.693	11.35	16.91	88.0
6	1.959	16.75	28.05	85.47
7	1.961	17.32	28.63	84.3

Table 12. Optical loss calculated for each layer of the monolithic tandem structure (in mA/cm²).

Step	Refl.	Glass	EVA	Al ₂ O ₃	ITO	ZnO-i	CdS	ZnO _x S _{1-x}	CZGSSe	MoSe ₂	Si	Al
1	10.29	-	-	-	1.59	0.25	1.92	-	21.19	0.71	9.74	0.78
2	7.86	0.78	0.28	-	1.64	0.25	2.06	-	22.21	0.71	9.90	0.78
3	7.47	0.77	0.28	-	1.64	0.25	2.06	-	22.05	-	11.16	0.78
4	8.67	0.78	0.29	-	1.67	0.25	-	2.29	20.64	-	11.11	0.78
5	7.47	0.77	0.28	-	1.64	0.25	2.06	-	22.05	-	11.16	0.78
6	7.47	0.77	0.28	-	1.64	0.25	2.06	-	22.05	-	11.16	0.78
7	7.27	0.77	0.28	-	1.64	0.25	1.93	-	16.70	-	16.84	0.78
8	6.60	0.76	0.28	0.00	1.66	0.25	1.96	-	17.08	-	17.09	0.79

In Figure 48 the absorbance spectra for each layer in the multilayered structure of the tandem cell is presented. It is worth noting that the highest parasitic loss is primarily attributed to the overall reflectance, as well as the ITO and CdS layers, with corresponding values of 7.29, 1.64, and 2 mA/cm², respectively. Integrated absorbance current for silicon and kesterite sub-cells is 16.7 and 16.84 mA/cm².

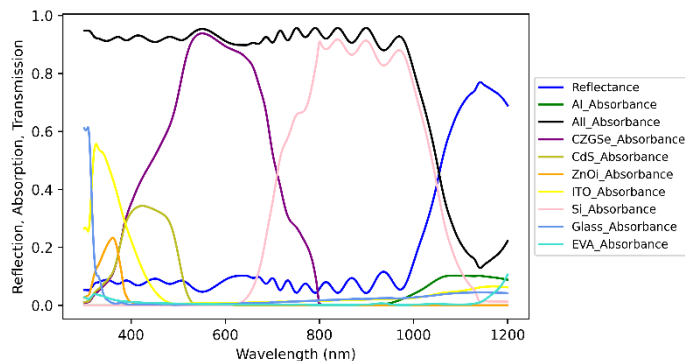


Figure 48. Absorbance in each of the layer of an optimized tandem cell calculated by transfer matrix method.

7.4 Sensitivity of tandem solar cell electrical characteristics to the variation of Al₂O₃ anti-reflective coating thickness

Various coloring techniques were detailed in the “1. INTRODUCTION” section, and two of these techniques, specifically Bragg reflectors and double-layer anti-reflective coatings applied to commercial solar cells, were employed in this study as prospective solutions. In this section, when only simulations are used, any technique could be implemented, restricted solely by simulation capabilities. Since tandem devices inherently consist of multi-layered structures, simpler coloring solutions should be favored by the market for economic reasons (not to make them even more complicated).

Hence, a simple single-layer anti-reflective coating (SLARC) comprising aluminum oxide (Al₂O₃) was introduced. In accordance with the principles outlined by E. Hecht (equation (7) from literature review section), the refractive index of such a layer should be the square root of the product of the refractive indices of the incoming medium and substrate medium [45]. In the simulated structure, this corresponds to the layer positioned between ethylene-vinyl acetate (EVA) (with a refractive index of 1.49 at 632 nm) and indium tin oxide (ITO) (with a refractive index of 2.07 at 632 nm) shown in Figure 46 (b). Consequently, the optimal SLARC is expected to have a refractive index of 1.76 at 632 nm. Aluminum oxide, with a refractive index of 1.68 at 632 nm, aligns closely with this criterion. It should be noted that any other metal oxide could be used here if a similar refractive index could be realized for such layer.

In this chapter, Al₂O₃ thickness was adjusted from 0 to 300 nm similarly as in section 4, where such intentional modification of thickness was proved as a successful method for variation of visual appearance of photovoltaic device.

Initially, dependence of electrical characteristics on Al₂O₃ thickness was analyzed. This dependence of J_{SC} (short-circuit current) of each of sub-cell and efficiency of the tandem device on the thickness of aluminum oxide is illustrated in Figure 49 (right and left axis, respectively). A periodic variation in both parameters is discernible in the latter figure. Notably, a relatively small variation in efficiency is observed, ranging from 28.05% to 28.63%. This corresponds to a relative change of approximately 2%. The maximum efficiency of 28.63% was attained with an aluminum oxide coating thickness of 100 nm. Short circuit current densities at this ARC thickness equals 17.07 and 17.09 mA/cm² for silicon and kesterite sub-cells respectively.

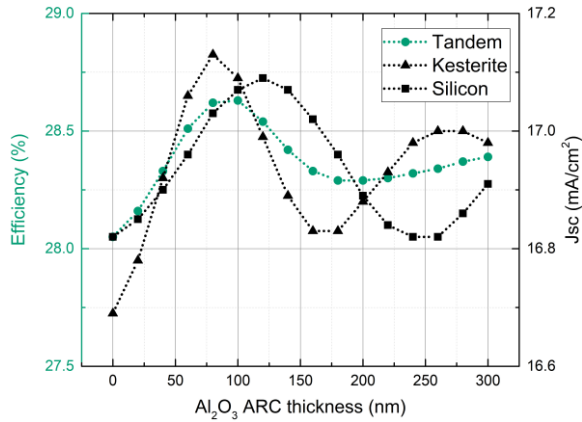


Figure 49. J_{sc} variation of each sub-cell (black, triangles – kesterite, rectangles - silicon) on the right Y axis and efficiency variation of tandem solar cell (green) on the left Y axis with changing thickness of Al_2O_3 anti-reflective coating.

7.5 Colorimetry and tandem viability for BIPV

Along with the electrical characteristics, optical characteristics (specifically reflectance spectra) were calculated for different thicknesses of SLARC of Al_2O_3 . This allowed evaluation of the acceptability of such layer for coloring of the tandem cells.

Characteristic color parameters are displayed in CIE color space in Figure 50 (a) and for better clarity (as values are very closely packed) zoomed version is also displayed in Figure 50 (b). In the latter figure, data points are located close to D65 illuminant (represented by the white point), indicating low color purity. The predominant hues are limited to brownish and purplish as most points are clustered in the lower-right part relative to the D65 point and relatively near it. In comparison with previous CIE analysis in this work, points do not strictly follow an ellipse-like shape. Only the last points indicate similar behavior. It should be noted that in this case laminated cells were simulated, while in section 5, non-laminated cell structures were used (due to the limitations of PV Lighthouse “OPAL 2” tool). Having in mind the results of section 4, a decrease in color purity could be expected after lamination. However, in real devices, lamination is necessary.

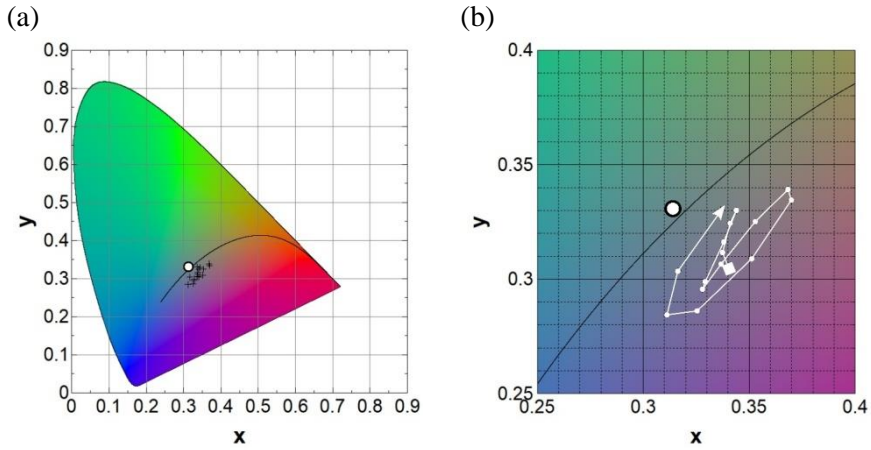


Figure 50. CIE diagram of tandem Silicon/kesterite solar cells with varying thickness of Al_2O_3 : full size diagram (a) and zoomed (b).

For the comparison, sRGB graph was also drawn with varying Al_2O_3 ARC thickness and is depicted in Figure 51. xyY characteristic parameters were converted using freeware online tool [106]. It should be noted that Origin Lab rounds RGB values to integers (error being ± 0.5 in each of RGB values). This figure confirms that available hues with such or similar kesterite/silicon tandem structure are very limited, and hues are brownish and purplish in whole ARC range from 0 to 300 nm.

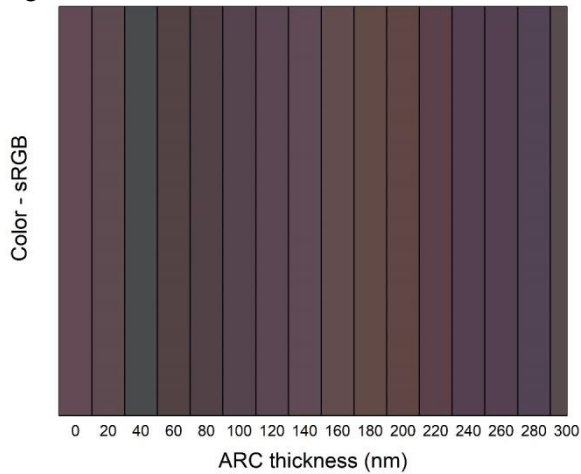


Figure 51. sRGB representation of kesterite/silicon tandem structures with varying Al_2O_3 ARC thickness.

For sensible colorimetric analysis, comparison with the competitive colored structures is important. Therefore, color purity of tandem photovoltaic devices is depicted in Figure 52, alongside experimental and simulated data for ITO/ SiN_x DLARC single junction solar cells taken from sections: 4 and

5. Notably, a clear distinction is observed among these data sets. The purity of tandem solar cells falls below 20% in whole ARC thickness range, while for the simulated single-junction ITO/SiNx DLARC solar cells purity is approximately 10% to 90% and for experimental from 10% to 60%. But for all of them this variation is periodical.

It can be concluded that such or similar tandem structures could be used in BIPV, however low color purity should be considered. Various practical scenarios may necessitate requirements for specific colors, requiring brighter and purer hues than those calculated in the present study. Conversely, non-pure colors such as brown may find preference in certain contexts, particularly in applications like roof tiles. Therefore, within the advantage of higher efficiency, such tandem structures can be an attractive option for BIPV for specific applications.

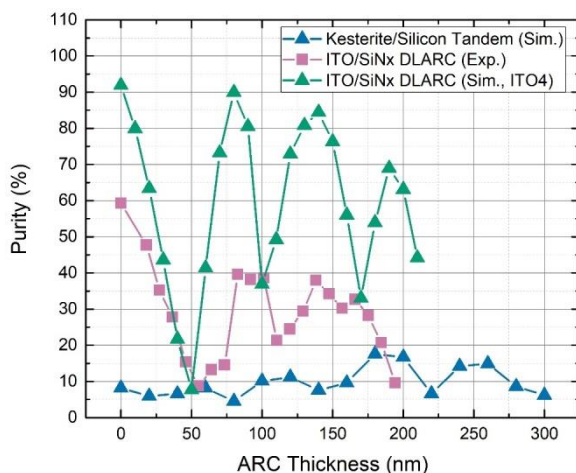


Figure 52. Comparison of color purity dependence on anti-reflective coating thickness for silicon single junction experimental (pink, rectangles) and simulated (green rectangles, using ITO4) and for kesterite/silicon tandem simulated (blue triangles) solar cells.

7.6 Summary

In this final section, an analysis of the coloring of tandem solar cells was performed, responding to the increasing demand for the replacement of single-junction silicon solar cells. The combined use of transfer matrix and SCAPS methods facilitated optical and electrical calculations, respectively. Initially, the tandem structure was optimized, revealing that an efficiency of 28.6% is achievable with an increase of 1 order of magnitude in the effective lifetime of kesterite (from 10 ns to 1 ns) and several other modifications. Considering

that texture was absent in simulated structure, efficiency could potentially be even higher.

Coloring was achieved through the variation of the thickness of a single anti-reflective coating, following a methodology from Sections 4 and 5 of this study. In this case, Al_2O_3 metal oxide was selected as being suitable, and its thickness modified from 0 to 300 nm. Consequently, a relatively low variation in efficiency, from 28.05% to 28.63%, was observed, resulting in a 2% relative change. The optimal thickness was determined to be 100 nm.

Colorimetric analysis revealed low color purity with color restricted to hues of brownish and purplish tones, as well as their combination. The assessment of color purity was compared with DLARC structures from Sections 4 and 5 of this study. Notably, the color purity of tandem solar cells remains below 20% across the entire anti-reflective coating (ARC) thickness range. In contrast, the simulated single-junction ITO/ SiN_x DLARC solar cells exhibit a broader range of color purity, spanning approximately 10% to 90%, whereas the experimental counterparts fall within the range of 10% to 60%.

This allowed to formulate fourth defensive statement.

Fourth defensive statement: ARC thickness variation of Al_2O_3 from 0 to 300 nm allows modification of reflectance spectra and therefore also color of kesterite/silicon monolithic tandem solar cells with efficiency loss of less than 2% (relative). Such modification is restricted by low color purity (compared to single junction solar cells) and hues are limited to brownish and purplish (and their mix).

8. SANTRAUKA

8.1 Įžanga

Fotovoltinis (PV) saulės elementas yra prietaisas, kuris verčia iš saulės ateinančią elektromagnetinę spinduliuotę į elektros energiją. Šiuo metu tai yra viena iš sparčiausiai augančių atsinaujinančių energijos rūšių [1]. Ši sritis turi didžiulį potencialą mažinant CO₂ emisijas, beisprenžiant vis didėjančio energijos poreikio problemą, nes gali suteikti daugiau energijos, nei mums reikia [2]. Tačiau, su laiku mažėjant žemės plotui saulės elektrinėms, bei siekiant pastatų energetinės nepriklausomybės atsiranda vis didėjantis poreikis į pastatus integruotai fotovoltikai (angl. BIPV). O šiuo metu šios srities augimas yra iš dalies ribojamas dėl rinkoje siūlomų mėlynų ir juodų saulės modulių, kurie dažnai sunkiai suderinami su architektūriniais sprendimais [107,108].

Apie 93-95% PV rinkos sudaro kristalinio silicio saulės elementai. Tokio saulės elemento spalvą lemia antirefleksinės dangos storis [5]. Keičiant šio sluoksnio storį, vieni bangos ilgiai sustiprinami kiti susilpninami dėl konstruktyvios ir destruktivos interferencijos ir taip gaunamas atspindžio spektras, kurį suvokiame kaip tam tikrą spalvą. Šioje technologijoje antirefleksinė danga dažniausiai būna suformuota iš hidrogenizuoto silicio nitrido (SiN_x:H) [4]. Paprastai jis optimizuojamas siekiant gauti mažiausią atspindį ir dėl to didžiausią saulės elemento našumą. To rezultate gaunami juodi arba mėlyni saulės elementai su SiN_x:H storiu apie 70-80 nm.

Yra ir kitų saulės elementų „spalvinimo“ metodų. Vienas iš jų yra dvigubos antirefleksinės dangos formavimas ant komercinio saulės elemento [8,10,109]. Taip galima modifikuoti atspindžio spektrą nepaveikiant pasyvacinių dangos SiN_x:H savybių, bei nedarant įtakos saulės elementų gamybos procesui. Kitaip nei viengubos antirefleksinės dangos atveju, kai reikalinga keisti lazerinės abliacijos sąlygas silicio nitrido dangai kontaktų formavimui. Kitas šios idėjos privalumas yra tas, kad formuojant dviejų sluoksnių antirefleksines dangas galima gauti mažesnę atspindžio koeficiento spektrą ir dėl to efektyvesnias fotovoltines struktūras nei naudojant vieną [6,110].

Esama ir labiau sofistikuotų spalvinimo metodikų, tokių kaip pavyzdžiui naudojant Bragg reflektorius [14–16]. Tai periodinės žemo ir aukšto lūžio rodiklių struktūros, kurios gali labiau stiprinti arba silpninti tam tikrus elektromagnetinės spinduliuotės dažnius [12,51]. Tai leidžia padidinti atspindžio koeficiento vertes reikiamoje srityje ir sumažinti kitose spektro dalyse. Ši metodika gali būti suformuota ir ant stiklo, kas leistų praplėsti

spalvos plotą nuo saulės elementų iki pilno modulio, taip visiškai atskiriant ir saulės elementų technologiją nuo spalvinimo.

Taip pat esama ir kitų technologijų saulės modulių spalvai modifikuoti: mica pigmentai [17], plazmoninės dangos [18], kvantinių taškų saulės elementai [19], skystieji kristalai [23], pusiau skaidrūs saulės elementai [21,22]. Tačiau dauguma jų dar labai ankstyvoje stadijoje, mažuose formatuose, sudėtingi arba turi mažus efektyvumus.

Dėl minėtų priežasčių, šiame darbe pirmiausia pasirinktas vienas paprasčiausių saulės elementų spalvinimo metodas, paremtas dvigubomis antirefleksinėmis dangomis suformuotomis ant komercinio silicio saulės elemento. Kitaip nei kituose darbuose, kaip antroji anti-atspindinti danga buvo naudotas indžio alavo oksidas (angl. ITO), kuris yra stabilus, bei jo lūžio rodiklį galima tiksliai keisti keičiant sluoksnio stechiometriją bei kristališkumą [24]. Taip pat galima tikėtis, jog šis oksidas sumažins varžos nuostolius kontaktuose. Galiausiai, taip pat svarbu pastebėti jog ITO dangų formavimas yra nenaujas industrijoje, jos pavyzdžiui naudojamos formuoti infraruoduosius spindulius atspindinčius stiklus.

Toliau šiame darbe buvo tiriamos galimybės panaudoti Bragg reflektorių struktūras spalvai keisti. Dėl savo prigimties šios daugiasluoksnės struktūros leidžia lanksčiau manipuluoti šviesos srautu, siekiant reikiamą jo dalį atspindėti, o kitą praleisti į fotovoltinį prietaisą [13,110]. Kitaip nei ankstesniuose darbuose, šiame darbe ši struktūra buvo optimizuota nedideliame, bei nelyginiame metalo oksidų skaičiui. Taip pat ji buvo realizuojama eksperimentiškai naudojant potencialiai pigią įmerkimo metodiką iš zolių gelių tirpalų.

Paskutinė darbo dalis buvo skirta tandeminių saulės elementų tyrimui, akcentuojant jų spalvinimo galimybes. Toks tyrimas dar nebuvo atliktas naudojant silicio saulės elementus. Šiai analizei buvo pasirinkta kesterito/silicio monolitinio tandemo struktūra, kuri buvo pažingsniui tobulinama bei optimizuojama. Gryno germanio kesteritas su kintančia anijono S,Se sudėtimi buvo naudojamas kaip viršutinė sub-celė, o silicis kaip apatinė. Buvo pademonstruotos šios struktūros spalvinimo galimybės keičiant Al_2O_3 antirefleksinės dangos storį ir jos įtaka elektrinėms bei optinėms fotovoltinio prietaiso charakteristikoms.

8.1.1 Darbo tikslas

Naudojant modeliavimus bei eksperimentinius tyrimus, iširti efektyvias metodikas komercinių saulės elementų spalvai keisti tam tikslui pritaikant funkcinius metalų oksidus.

8.1.2 Darbo uždaviniai

1. Teorinė analizė ir eksperimentinis funkcinių dangų įgyvendinimas, suformuojant papildomą ITO sluoksnį virš komercinių silicio saulės elementų, siekiant sukurti dvigubą antirefleksinį sluoksnį. Išnagrinėti dviejų kritinių parametrų - storio ir lūžio rodiklio - poveikį saulės elementų optinėms ir elektrinėms charakteristikoms, ypatingą dėmesį skiriant spalvos aspektui. Įvertinti pasiūlytos technologijos tinkamumą ir priimtumą panaudojimui saulės moduluose.
2. Surasti optimalią funkcinių metalo oksidų dangų architektūrą Bragg reflektoriaus struktūrai, skirtai taikymams fotovoltikoje. Eksperimentiškai realizuoti pasiūlytą struktūrą ant stiklo padėklų, naudojant įmerkimo metodiką iš zolių-gelių tirpalų, bei charakterizuoti jos optines (įskaitant spalvą) ir elektrines savybes. Vėliau pademonstruoti jos tinkamumą PV moduliams. Galiausiai iširti technologijos tinkamumą industrijai įvertinant spalvų charakteristikų jautrumą lūžio rodiklio ir storio nuokrypiams nuo optimalios Bragg sąlygos.
3. Iširti tandeminių saulės elementų potencialą apatinei sub celei naudojant silicio saulės elementą. Išanalizuoti tokio įrenginio spalvinimo galimybes ir jų poveikį jo elektrinėms savybėms. Palyginti šias charakteristikas su su kitais darbe naudotais spalvinimo būdais ir įvertinti tokių tandemų tinkamumą į pastatus integruotai fotovoltikai (angl BIPV).

8.1.3 Darbo naujumas

Mūsų grupė pirmoji naudojo ITO kaip dvigubos antirefleksinės dangos dalį suformuotą ant komercinių silicio saulės elementų viršaus. Šiame tyrime naudojant modeliavimus, pirma kartą buvo analizuotas dvigubos antirefleksinės dangos sluoksnio lūžio rodiklio poveikis optinėms charakteristikoms ir spalvai. Nauji saulės elementai buvo pagaminti naudojant magnetrono dulkinimo metodiką keičiant ITO dangos storį. Vėliau tokie elementai buvo pirmą kartą panaudoti gaminant PV mini modulius. Galiausiai, lyginant su kitais darbais, buvo atlikta gerokai platesnė spalvinė analizė, pabrėžiant skirtumus tarp laminuotų ir nelaminuotų saulės elementų.

Kitame šio darbo skyriuje pristatoma inovatyvi Bragg'o reflektoriaus struktūra, kuri buvo optimizuota mažesniai ir nelyginiai aukšto ir žemo lūžio rodiklio medžiagų sluoksnių skaičiui lyginant su kitais darbais. Naudojant modeliavimus, buvo įrodyta, kad nelyginių ir lyginių metalo oksidų dangų skaičių struktūros turi panašias charakteristikas, todėl buvo pasirinkta paprastesnė struktūra lengvesniai eksperimentiniam įgyvendinimui. Pirmą kartą tokia struktūra buvo eksperimentiškai realizuota fotovoltikoje naudojant

potencialiai pigią zolių gelių įmerkimo techniką. Be to, lyginant su kitais darbais, šiame darbe buvo atlikta išsamesnė spalvinė analizė ir Brago reflektoriaus technologija buvo palyginta su kitomis spalvinėmis technologijomis, naudojant charakteristinius parametrus iš CIE spalvų erdvės: xyY ir spalvos grynumo parametras. Galiausiai, buvo pademonstruota kaip spalva priklauso nuo sluoksnio lūžio rodiklio bei storio nuokrypių nuo optimalios Bragg'o sąlygos, ko nebuvo ankstesniuose darbuose.

Trečioje darbo dalyje buvo pirmą kartą analizuojamos monolitinio tandeminio saulės elemento spalvos keitimo galimybės, naudojant skaitmeninius modeliavimus, kuriuose kesterito saulės elementas buvo naudojamas viršutinėje dalyje, o silicis – apatinėje. Šio skyriaus pirmoje dalyje buvo atlikta dalinė kesterito saulės elemento optimizacija. Šiam tikslui pasiekti buvo panaudoti tokio elemento sugerties sluoksnio lūžio rodiklio spektrai su draustinės juostos tarpu nuo 1.52 iki 2.02 eV ($\text{Cu}_2\text{ZnGe}(\text{S}_x\text{Se}_{1-x})_4$ arba CZGSSe) [36] The electronic structure, elastic and optical properties, siekiant nustatyti optimalų kesterito storį ir draustinės juostos tarpą. Tai platesnis intervalas lyginant su ankstesniuose darbuose naudotu didžiausiu 1,6 eV draustinės juostos tarpu [35]. Be to, vietoj apatinės sub celės buvo naudojamas šiulaikinis PERC silicio saulės elementas su 24% efektyvumu [32], tuo tarpu dauguma kitų darbų naudojo senesnius silicio prietaisus [38,39]. Galiausiai, buvo ištirtos tokio tandeminio fotovoltinio elemento spalvos keitimo galimybės keičiant Al_2O_3 funkcinio metalo oksido storį nuo 0 iki 300 nm ir analizuojant kaip tai lemia jo optines bei elektrines charakteristikas. Taip pat buvo palyginti charakteringi spalviniai parametrai su kitų spalvotų elementų technologijų parametrais ir įvertinta galimybė juos naudoti į pastatus integruotoje fotovoltikoje.

8.1.4 Ginamieji teiginiai

Pirmasis ginamasis teiginys. Indžio alavo oksido (ITO) arba kito panašaus metalo oksido sluoksnio storio keitimas nuo 0 iki 240 nm, suformuojant dvigubą antirefleksinį sluoksnį ant komercinio silicio saulės elemento viršaus, leidžia modifikuoti saulės elemento spalvų paletę nuo mėlynos iki rudos. Šis pakeitimas siejamas su santykinai mažu trumpojo jungimo srovės tankio nuostoliu iki 8%, o po laminavimo mėlynam ir žaliajam fotovoltiniams moduliams spalvos grynumas sumažėja 82% ir 71% (atitinkamai).

Antrasis ginamasis teiginys. ITO metalo oksido, naudojamo dvigubo sluoksnio antirefleksinėms silicio saulės elementų dangoms suformuotoms ant $\text{SiN}_x\text{:H}$ viršaus, lūžio rodiklio derinimas leidžia sukurti žemesnes, mėlynai

pasislinkusias ir siauresnes smailes paviršiaus atspindžio spektre, kai ITO lūžio rodiklis yra mažesnis (1,8 ties 632 nm), lyginant su didesniu lūžio rodikliu (2,07 ties 632 nm). Tai lemia aukštesnę spalvos ryškumą, esant didesniam ITO lūžio rodikliui, tačiau atspalviai ir spalvos grynumas išlieka panašūs.

Trečiasis ginamasis teiginys. Optimali Bragg reflektoriaus struktūra, skirta saulės elementų spalvinimui naudojant TiO_2 ir SiO_2 metalo oksidus, susideda tik iš 3 sluoksnių, suformuotų ant stiklo padėklo (stiklas/ $TiO_2/SiO_2/TiO_2$), ir leidžia pasiekti 2-3 kartus didesnę spalvos ryškumą palyginti su moduliais, pagamintais naudojant komercinius spalvotus saulės elementus. Toleruoti technologiniai nuokrypiai nuo kolorimetrinių parametų, kad šių skirtumų mūsų akis neatskirtų, yra mažiau nei +/- 0,05 lūžio rodiklio spektrui ir mažiau nei apie +/- 2% sluoksnio storiui.

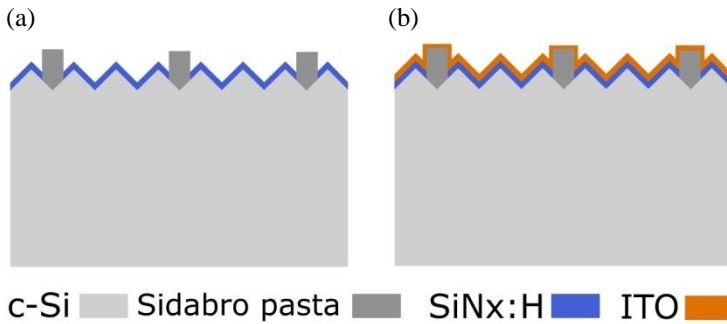
Ketvirtasis ginamasis teiginys. Antirefleksinio Al_2O_3 sluoksnio storio keitimas nuo 0 iki 300 nm leidžia modifikuoti atspindžio spektrą ir taip pat spalvą kesterito/silicio monolitiniams tandeminiams saulės elementams, su mažesniais nei 2% efektyvumo nuostoliais. Tokie saulės elementai pasižymi gana žemu spalvos grynumu, o galimi atspalviai yra riboti rudais ir violetiniais (ir jų mišiniu).

8.2 Funkciniai skaidrūs oksidai dviguboms anti-atspindinčioms dangoms fotovoltinėse struktūrose formuoti – sluoksnio storio įtaka

Šiame skyriuje aprašyti rezultatai analizuojant kaip su dvigubomis antirefleksinėmis dangomis suformuotomis ant multi-kristalinio komercinio saulės elemento uždengiant papildomą indžio alavo oksido sluoksnį galima keisti saulės elemento spalvą. Pirmiausia, optiniais modeliavimais pademonstruotas sluoksnio storio poveikis saulės elemento optinėms savybėms ir spalvai. Vėliau magnetroniniu dulkinimu eksperimentiškai buvo realizuotos šios struktūros. Sulaminavus tokius saulės elementus, buvo patvirtintas technologijos tinkamumas fotovoltiniams moduliams. Visos gautos struktūros buvo charakterizuotos ir palyginti jų kolorimetriniai parametrai. Tai leido suformuoti pirmąjį ginamąjį teiginį.

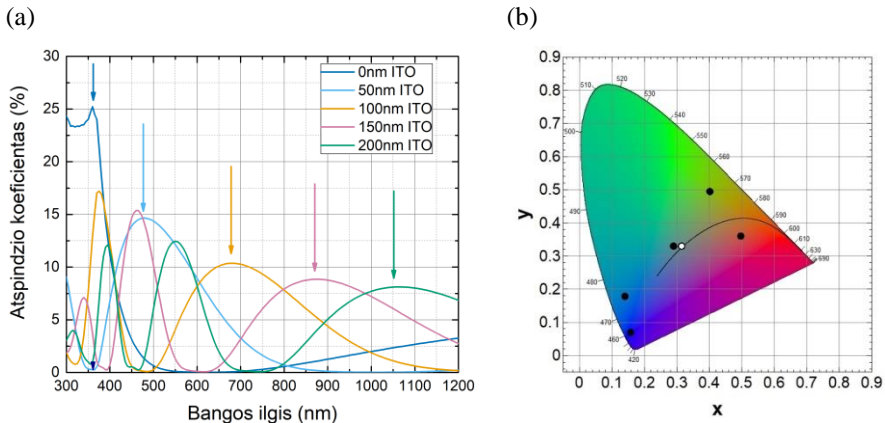
8.2.1 Optinis modeliavimas (ITO/ $SiN_x:H$ dviguboms antirefleksinėms dangoms)

Optiniai modeliavimai buvo atlikti naudojant nemokamą įrankį pavadinimu „OPAL 2“, sukurtą „PV Lighthouse“ [41,70]. Programinė įranga yra išsamiau aprašyta skyriuje: 3.3, o modeliavimo parametrai pateikti skyriuje 4.1. Dominančios struktūros vaizdas pateiktas Pav. 1.



Pav. 1. Dvigubos antirefleksinės dangos struktūra suformuota (b) ant komercinio silicio saulės elemento (a) Double anti-reflective coating structure formed on the top (a) of the commercial silicon solar cell (b).

Šiame skyriuje atliktos simuliacijos skirtos įvertinti storio įtaką saulės elemento atspindžio charakteristikoms. ITO storis buvo keičiamas nuo 0 iki 200 nm, 50 nm žingsniu. Rezultatai pateikti Pav. 2.



Pav. 2 Sumodeliuotos saulės elemento su dvigubam antirefleksine danga atspindžio charakteristikos keičiant ITO storį nuo 0 iki 200 su 50 nm žingsniu (a). Paveiksle (b) CIE spalvų gamos koordinatės suskaičiuotos iš atspindžio spektrų su skirtingu ITO storiumi (juodi taškai). Baltas taškas atitinka D65 šviesos šaltinį [69].

Gana aiškiai galima matyti maksimumo raudonąjį poslinkį bei papildomų maksimumų smailių atsiradimą didinant ITO sluoksnio storį. Taip pat pastebėtina, kad šie maksimumai žemėja didėjant storiui.

Atspindžio spektrų kitimas gali būti tiesiogiai susietas su spalvos pokyčiais. Šiam tikslui buvo suskaičiuoti CIE parametrai (xyY) ir atvaizduoti CIE spalvų gamoje (Pav. 2b). 5 juodi taškai atitinka gautus 5 atspindžio spektrus, o baltas taškas yra šviesos šaltinis (D65 [73]). Matome, jog taškai pasiskirstę skirtingose šios gamos vietose, kur matomos skirtingos spalvos: mėlyna, žalsvai mėlyna, žalia, žalsvai geltona, raudona. Taigi, aišku, jog tikslingas dvigubo sluoksnio dangos storio kitimas leidžia modifikuoti

fotovoltinių elementų spalvą. Toliau, šiame darbe šios struktūros bus realizuojamos eksperimentiškai.

8.2.2 Bandinių ruošimas (magnetroninis dulkinimas)

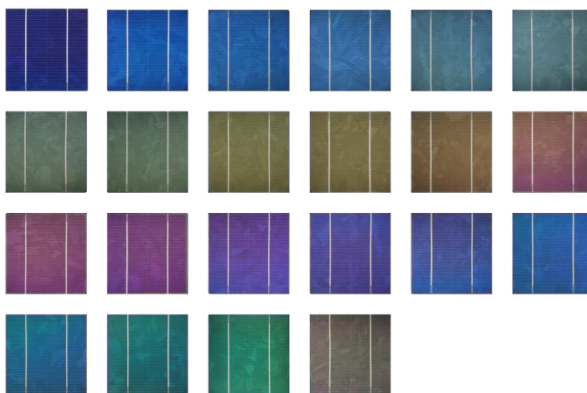
ITO dangų formavimui buvo naudojamas radijo dažniu keičiamo elektrinio lauko magnetroninis dulkinimas. Dengimo parametrai buvo tokie: kambario temperatūra, $P=100$ W, $p=5 \cdot 10^{-3}$ mbar, ITO taikinio diametras – 10 cm.

Sluoksniai buvo formuojami ant komercinių multi-kristalinių saulės elementų. Tam tikslui M1 dydžio (157.5x157.5 mm) 18.4% efektyvumo saulės elemento plokštelė lazeriu buvo pjaunama į keturias lygias dalis (78.38 mm x 78.38 mm).

Dangos buvo formuojamos dengimo trukmę keičiant vienodais intervalais nuo 225s iki 2362.5 s su 112.5 s žingsniu, siekiant gauti vienodo skirtumo dangų storius. Apart saulės elementų sluoksniai buvo uždengti ir ant stiklo, ant kurio su profilometru buvo matuojamas jų storis (ant stiklo buvo suformuotos ne visų ITO storių dangos). Gauti storiai buvo aproksimuoti tiese (kuri pateikta skyriuje 4.3kad nustatyti trukmės ir sluoksnio storio ryšį).

8.2.3 Bandiniai su dvigubomis ITO/SiN_x:H antirefleksinėmis dangomis

Tipiniai bandiniai su kintamu ITO dangos storiu suformuoti ant multi-kristalinių silicio saulės elementų viršuje esančio SiN_x:H sluoksnio pavaizduoti Pav. 3. ITO dangų storiai bandiniuose yra nuo 18.5 iki 194.25 su 9.25 nm žingsniu (nuo viršutinio kairio kampo eilėmis žemyn). Pirmasis bandinys yra kontrolinis – be ITO dangos (mėlynas), o rudas yra išskirtinis su 240.5 nm danga.

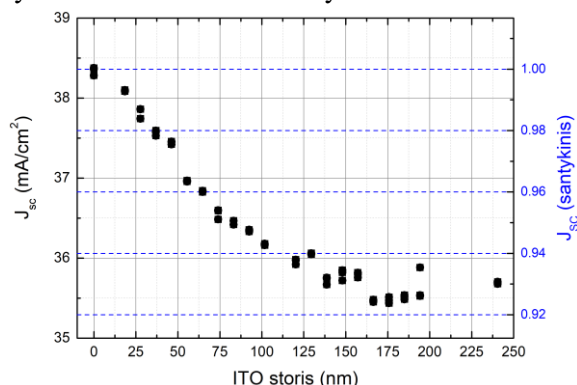


Pav. 3 Spalvoti multi-kristaliniai saulės elementai su kintamu dvigubos antirefleksinės dangos viršutinio sluoksnio (ITO) storiu nuo 18.5 iki 194.25 su 9.25 nm žingsniu (nuo viršutinio kairio kampo eilėmis žemyn).

Pirmasis bandinys yra kontrolinis – be ITO dangos, o rudas yra išskirtinis su 240.5 nm danga.

Gana ryški ir plati spalvų paletė matoma šiame paveiksle. Spalva tolygiai kinta keičiantis sluoksnio storiui (kas 9.25 nm). Taip pat pastebėtina, jog sluoksnio tolygumas yra gana aukštas, nes matomas tik vienas atspalvis tame pačiame saulės elemente.

Toliau šiems bandiniams buvo išmatuotos elektrinės charakteristikos su impulsiniu saulės imitatoriumi. Trumpojo jungimo srovės tankio vertės nuo ITO storio pavaizduotos Pav. 4. Kairėje ašyje pateiktos absoliutinės vertės, dešinėje – santykinės. Kiekvienas bandinys buvo matuotas tris kartus.

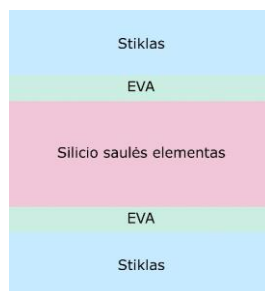


Pav. 4. Absoliutinis (a) ir santykinis (b) trumpojo jungimo srovės tankio pasiskirstymas nuo ITO dangos storio (a).

Grafikuose matomas trumpojo jungimo srovės tankio mažėjimas iki maždaug 175 nm, kai jis pradeda šiek tiek kilti. Toks kitimas koreliuoja su kitais moksliniais darbais [5,8–10]. Maksimalūs nuostoliai ties 175 nm beveik siekia 8%. Šie rezultatai pakliūna į įžangoje pristatytų kitų mokslinių grupių rezultatų intervalą.

8.2.4 Technologijos su dvigubomis ITO/SiN_x:H antirefleksinėmis dangomis tinkamumas saulės moduliams

Tolesniame etape, šie moduliai buvo laminuojami, kas yra būtinas žingsnis galvojant apie technologijos komercializavimą. Šis žingsnis dar svarbus ir siekiant palyginti jų charakteristikas prieš ir po laminavimo. Šiam tikslui buvo parinktos dvi skirtingos spalvos: mėlyna (kontrolinis bandinys) ir žalia (su 184.5 nm ITO danga). Po 6 celes buvo sujungta nuosekliai jas sulituojuojant ir vėliau jos buvo sulaminuotos. „Išskępti“ fotovoltiniai moduliai



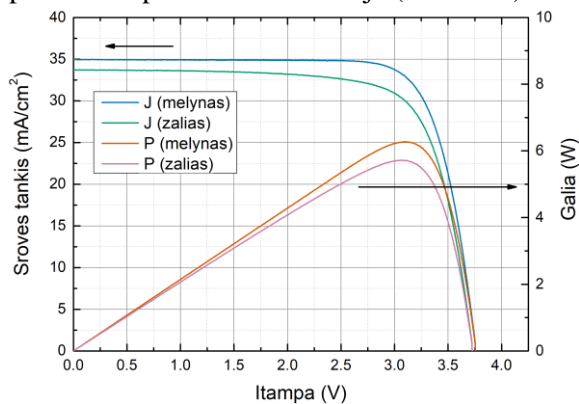
Pav. 5. Sluoksniuota saulės modulio laminavimo struktūra.

pavaizduoti Pav. 6. Laminavimui naudota struktūra pavaizduota Pav. 5: stiklas, etileno vinilo acetatas (EVA), saulės elementai, EVA, stiklas.



Pav. 6. Dvi saulės panelės naudojant mėlynus (kontrolinis, be ITO) ir žalius (su 194.5 nm ITO danga) saulės elementus.

Sulaminuoti moduliukai buvo charakterizuoti saulės imitatoriumi, gautos J-V charakteristikos pavaizduotos Pav. 7, o iš jų paimti ir suskaičiuoti charakteringi parametrai pavaizduoti lentelėje (Lentelė 1).



Pav. 7. Žalio ir mėlyno saulės modulio J-V charakteristikos.

Lentelėje matomas 8.83% galios skirtumas tarp šių dviejų modulių. Galios nuostoliai šiuo atveju susideda iš trumpojo jungimo srovės nuostolių (-3.54%), fill faktoriaus sumažėjimo (-4.73%), bei nedidelio atviros grandinės įtampos sumažėjimo (-0.74%). Trumpojo jungimo srovės nuostoliai yra sąlygoti pasikeitusių atspindžio charakteristikų, kurie sumažina patenkančios

šviesos kiekį į fotovoltinį elementą. Tuo tarpu V_{oc} nuo šviesos priklauso nestipriai dėl to šis nuostolis gerokai mažesnis.

Lentelė 1. Mėlyno (kontrolinio) ir žalio mini saulės modulių elektriniai parametrai paimti/suskaičiuoti iš J-V charakteristikų.

	V_{OC} , V	I_{SC} , A	V_{MAX} , V	I_{MAX} , A	P_{MAX} , W	FF, %	R_S , Ω	R_{SH} , Ω	Eff, %
Mėlynas	3.77	2.15	3.10	2.03	6.27	77.6	0.18	345.6	17.19
Žalias	3.74	2.07	3.06	1.87	5.72	73.9	0.20	287.8	15.68
Δ , %	-0.74	-3.54	-1.10	-7.79	-8.83	-4.73	11.0	-16.72	-8.78

Fill faktorius yra parametras nusakantis voltamperinės charakteristikos „stačiakampiškumą“ [42]. Jis stipriai priklauso nuo nuoseklios bei šunto varžų. FF nuostoliai šiuo atveju labiausiai nulemti 17% sumažėjusia šunto varža. Šis sumažėjimas gali būti siejamas su ITO sąlygotu srovės aptekėjimu saulės elemento kraštuose. Dėl to būtų tikslinga naudoti rėmelį kraštų izoliavimui prieš formuojant laidžias dangas. Taip pat lentelėje pastebimas ir nuoseklios varžos padidėjimas, kuris parodo, kad uždengtas ITO sluoksnis nepagerina krūvio surinkimo. Tai galėtų būti nulemta laidumo skirtumo tarp sidabro pasta dengto varinio kontakto, bei šio laidaus skaidraus oksido. Svarbu pastebėti, jog FF bei R_S ir R_{SH} priklauso ir nuo litavimo kokybės, tačiau manome, kad tai yra mažiau reikšminga nei matavimuose registruoti pokyčiai.

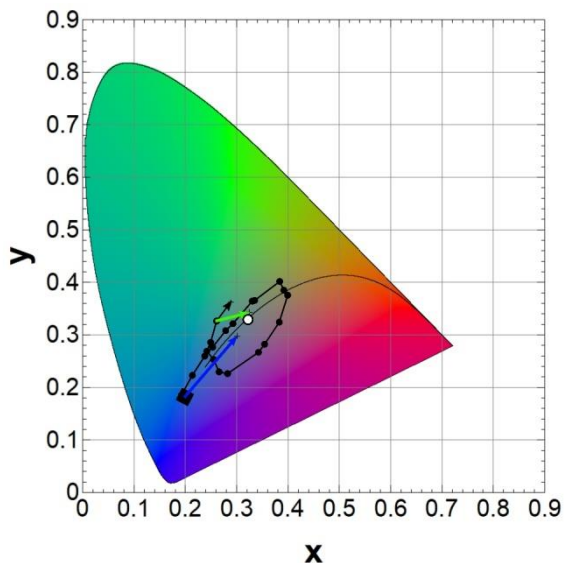
8.2.5 Dvigubų ITO/SiN_x:H antirefleksinių dangų kolorimetrinė analizė

Siekiant įvertinti spalvos kiekybinius parametrus, iš bandinių atspindžio spektrų buvo suskaičiuoti kolorimetriniai parametrai ir atvaizduoti CIE spalvų erdvėje (Pav. 8). Juodu kvadratu pažymėtas kontrolinis bandinys su 0 nm ITO ir jungiant tiese juodi taškai atitinka bandinius su vis didėjančiu ITO storiu, kol pasiekiamas rodykle pažymėtas paskutinis bandinys (su storiausia ITO danga). Baltas taškas atitinka šviesos šaltinį (D65).

Svarbu pastebėti, kad CIE diagrama yra sukurta taip, jog kraštuose (išskyrus apatinį) yra taškai atitinkantys monochromatinę spinduliuotę ir švaresnes spalvas (Pav. 2 b), o esantys arčiau šviesos šaltinio (vidutinę dienos šviesą atitinkantis šviesos šaltinis - D65, 6500K) yra taškai apibūdinantys purvinesnę spalvą, kurios spektras plokštesnis, turintis daug bangos ilgių.

Pav. 8 matome, jog juodi taškai judėdami nuo stačiakampo iki rodyklės didėjant ITO sluoksnio storiui, piešia elipsei panašias formas ir spalvos atspalviai keičiasi nuo mėlyno iki purpurinio, o vėliau vėl iš naujo (tik šiek tiek keičiasi spalvos grynumas). Taškai artėja ir tolsta nuo balto taško, kas reiškia, kad spalvos grynumas kinta periodiškai. Angliškoje darbo versijoje

buvo suskaičiuotas ir atidėtas spalvos grynumas nuo antirefleksinės dangos storio skyriuje 4.6, nubraižius spalvos grynumo parametro [74] priklausomybę nuo nulinės eilės maksimo padėties. Buvo gauta, kad grynumas kinta nuo 10 iki 60% (Figure 23). Sulaminavus bandinius spalvos grynumas sumažėjo 82% mėlynam ir 71% žaliai fotovoltiniam moduliui.



Pav. 8. Eksperimentinių multi-kristalinių saulės elementų su dvigubomis ITO/SiN_x:H anirefleksinėmis dangomis CIE diagrama (juodi taškai). Didėjančio storio bandinių serija sujungta linijomis pirmą tašką žymint kvadratu ir pabaigiant juoda rodykle. Žalia ir mėlyna rodykle pavaizduotas pokytis tarp nelaminuotų ir laminuotų bandinių (rodyklė rodo į moduliukus).

8.2.6 Skyriaus apibendrinimas

Šiame skyriuje buvo pristatyti rezultatai ant silicio multi-kristalinių saulės elementų formuojant papildomą ITO dangą (nuo 0 iki 240 nm) ir taip suformuojant dvigubą antirefleksinį sluoksnį. Buvo tiriama sluoksnio storio įtaka optinėms ir elektrinėms charakteristikoms naudojant modeliavimus ir realizuojant struktūras eksperimentiškai. Gauta plati spalvų paletė nuo mėlynos iki purpurinės su trumpojo jungimo srovės tankio nuostoliais iki 8%. Idėjos tinkamumas fotovoltikai buvo įrodytas sulaminavus dviejų spalvų saulės elementus į modulių. Atlikus kolorimetrinę analizę gauta, jog spalvos grynumas kinta periodiškai nuo 10 iki 60% keičiantis ITO dangos storiui, o po laminavimo mėlynam (kontroliniam) moduliui jis sumažėjo 82%, žaliai (su 194.5 nm ITO) - 71%.

Šie rezultatai leido suformuoti pirmąjį ginamąjį teiginį.

Indžio alavo oksido (ITO) arba kito panašaus metalo oksido sluoksnio storio keitimas nuo 0 iki 240 nm, suformuojant dvigubą antirefleksinį sluoksnį ant komercinio silicio saulės elemento viršaus, leidžia modifikuoti saulės elemento spalvų paletę nuo mėlynos iki rudos. Šis pakeitimas siejamas su santykinai mažu trumpojo jungimo srovės tankio nuostoliu iki 8%, o po laminavimo mėlynam ir žaliaam fotovoltiniams moduliams spalvos grynumas sumažėja 82% ir 71% (atitinkamai).

8.3 Funkciniai skaidrūs oksidai dviguboms anti-atspindinčioms dangoms fotovoltinėse struktūrose formuoti – sluoksnio lūžio rodiklio įtaka

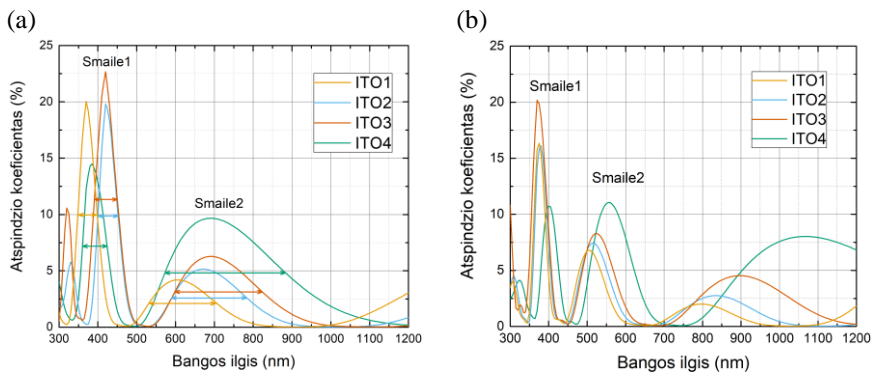
Šiame skyriuje buvo pratęsti tyrimai su dvigubomis antirefleksinėmis dangomis, įvertinant lūžio rodiklio įtaką tokių dangų optinėms charakteristikoms ir spalvai. Tai leido suformuoti antrąjį ginamąjį teiginį.

8.3.1 Optiniai modeliavimai (for ITO/SiN_x:H DLARCs)

Skaitmeniniai modeliavimai buvo aliekami analogiškai kaip ir ankstesniame skyriuje, tik šiame skyriuje buvo naudojami 4 ITO lūžio rodiklio spektrai (pavaizduoti angliškoje versijoje: Figure 23). Šie spektrai buvo pasirenkami remiantis Pour ir Shafai darbu, kuriame mokslininkai parodė, kad kryptingai keičiant dengimo sąlygas, galima keisti šio skaidraus laidaus oksido lūžio rodiklį nuo $n=1.69$ iki $n=2.1$ prie 632 nm bangos ilgio [24]. Renkantis spektrus, buvo stengiamasi perdengti šį intervalą: ITO1 (1.73 at 632 nm) [72], ITO2 (1.8 at 632 nm) [72], ITO3 (1.87 at 632 nm) [75], ITO4 (2.07 at 632nm) [72].

Du skirtingi ITO sluoksnių storiai buvo pasirinkti optinių charakteristikų analizei: 100 ir 200 nm. Gauti spektrai pavaizduoti Pav. 9.

Pastarajame paveikslėlyje galima pastebėti, jog atspindžio smailė2 yra pasislinkusi bei skirtingo maksimumo pločio ir aukščio skirtingiems ITO spektrams. Kiekybiniam įvertinimui buvo suskaičiuoti smailių pločiai pusės maksimumo aukštyje (angl full width at half maxima – FWHM) (Lentelė 2). Matome, jog aukštesniam ITO lūžio rodiklio spektrui maksimumo plotis bei aukštis yra didesni ir atvirščiau. Taip pat aukštesniam ITO spektrui smailės yra pasislinkusios į raudonąją pusę. Toliau darbe bus tiriamas šių poslinkių efektas spalvai.



Pav. 9. Skaitmeninių modeliavimų būdu gauti saulės elementų su dvigubomis ITO dangomis atspindžio spektrai esant skirtingiems šių dangų storiams: 100 (a) ir 200 nm (b).

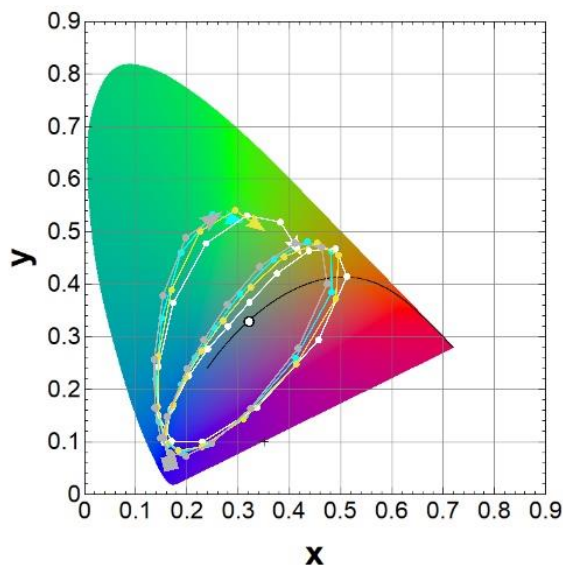
Lentelė 2. Atspindžio smailių plotis pusės aukštyje (FWHM) fotovoltiniams elementams su dviguba antirefleksine danga, kur ITO storis 100 ir 200 nm.

	ITO storis: 100 nm		ITO storis: 200 nm	
	FWHM (Smailė 1)	FWHM (Smailė 2)	FWHM (Smailė1)	FWHM (Smailė2)
SiN _x :H/ITO1	49.9	175.5	33.6	81.3
SiN _x :H/ITO2	51.15	185.12	35.7	86.38
SiN _x :H/ITO3	59.13	225.05	42.27	92.13
SiN _x :H/ITO4	63.22	309.27	45.15	110.6

8.3.2 Kolorimetrinė analizė (dviguboms antirefleksinėms dangoms su ITO/SiN_x:H)

Kolorimetriniai analizei ITO dangos storis buvo keičiamas nuo 0 iki 210 su 10 nm žingsniu skirtingiems ITO lūžio rodiklio spektrams ir iš gautų atspindžio spektrų buvo skaičiuojami charakteringi parametrai: xyY bei spalvos grynumas.

Gauta CIE diagrama pavaizduota Pav. 10. Pastarajame paveikslėlyje matome, jog didėjant storiui nuo 0 iki 210 brėžiama į elipsę panaši kreivė, panašiai kaip ir iš eksperimentinių rezultatų praeitime skyriuje. Atspalvių atžvilgiu visos keivės panašios, tik didėjant lūžio rodiklio spektrui nuo ITO1 iki ITO4 matomas nedidelis postūmis į raudonąją pusę. Taip pat pastebėtina, jog yra tam tikras atspalvio postūmis priklausomai nuo dangos storio: ITO1 rodykle pasibaigia ties maždaug žalia spalva, o ITO1 ties gelsva (rodyklė rodo į paskutinį tašką su 210 nm ITO danga). Atspindžio spektre toks postūmis atitinka 300 nm smailės postūmį.



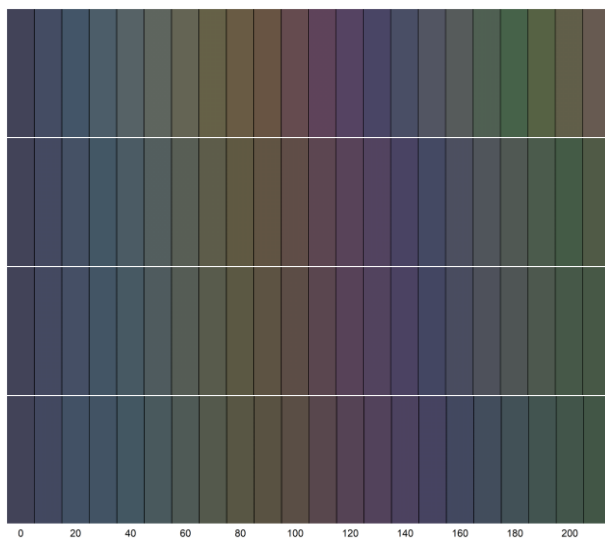
Pav. 10. CIE diagrama simuliuotiems saulės elementams su skirtingais ITO lūžio rodiklio spektrais: ITO1 (pilka), ITO2 (žydra), ITO3 (geltona) ir ITO4 (balta). D65 šviesos šaltinis pažymėtas baltu tašku.

Siekiant palyginti spalvas vizualiai, CIE parametrai xyY buvo paversti į sRGB (RGB gama naudojama monitoriuose) gamą ir yra pavaizduoti Pav. 11. Kaip ir CIE diagramoje, gretimi taškai skiriasi per 10 nm. Dėl to pavaizduotas sRGB spektras diskretinis. Pav. 11 skirtingos spalvų gamos skirtingiems ITO atidėtos didėjančia tvarka apačioje esant ITO1, o viršuje ITO4.

Spalvos visuose 4 rinkiniuose labai panašios, kaip jau buvo minėta ir lyginant CIE diagramas. Šiek tiek aiškesnės ir ryškesnės spalvos pastebimos viršutiniame spektre lyginant su žemesniais. Taip pat pastebimas ir anksčiau minėtas atspalvio postūmis nuo dangos storio, kuris atitinka apie 20-30 nm tarp ITO1 ir ITO4 lyginant žalią spalvą. Kitaip nei minėta prieš tai, ITO4 prie 210 nm atitinka rudą, bet ne gelsvą spalvą.

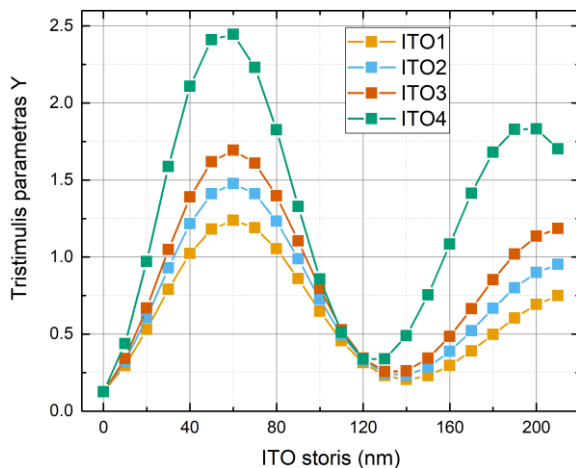
Tolesniu žingsniu buvo palygintas CIE parametras Y apibūdinantis šviesos ryškumą. Toks grafikas atidėtas Pav. 12.

Šiame paveikselyje gana ryškiai išsiskiria tendencija, kad didėjant ITO lūžio rodikliui didėja spalvos ryškumas. Čia taip pat pastebėtinas ir periodinis šio parametro kitimas, bei nedidelis postūmis (matomas antrojeje smailėje). Šie rezultatai sutinka su anksčiau atvaizduotomis atspindžio charakteristikomis, kur didesnės atspindžio smailės užfiksuotos dviguboms antirefleksinėms dangoms suformuotoms naudojant didesnio lūžio rodiklio ITO dangas (Pav. 9).



Pav. 11. sRGB skalėje atvaizduoti 4 skirtingi taškų rinkiniai su skirtingais ITO lūžio rodikliais, priklausomai nuo dangos storio (atidėti nuo apačios didėjančia tvarka: ITO1 < ITO2 < ITO3 < ITO4).

Paskutinis lyginamas kolorimetrinis parametras yra spalvos grynumas. Šis parametras nuo ITO storio atidėtas angliškoje šio darbo versijoje (Figure 30). Lyginant šio spalvos grynumo vertes, modeliuotoms struktūroms jis periodiškai keičiasi nuo 5 iki 90% (plačiau nei eksperimentiniuose: 10-60%). Šie skirtumai gali būti, dėl antirefleksinių dangų paviršiaus morfologijos skirtumų modeliuotoms ir eksperimentinėms fotovoltinėms struktūroms. Multi-kristalinių saulės elementų atveju paviršiaus tekstūra yra sudėtinga, dėl naudojamo rūgštinio ėsdinimo, priešingai nei monokristaliniams, kur ėsdinimas (tekstūravimas) yra daromas naudojant šarmus ir taip suformuojant piramidinę tekstūrą. Dėl šių skirtumų, galėjo atsirasti nuokrypiai tarp eksperimentinių ir modeliuotų spektrų. Kita vertus, aiškaus skirtumo tarp skirtingų ITO lūžio rodiklių spektrų nematyti (lyginant modeliuotus spektrus tarpusavyje).



Pav. 12. CIE parametro Y priklausomybė nuo ITO dangos storio skirtingiems ITO spektrams.

8.3.3 Skyriaus apibendrinimas

Šiame skyriuje naudojant optinius skaitmeninius modeliavimus buvo analizuojamas lūžio rodiklio poveikis saulės elementų su dvigubomis antirefleksinėmis dangomis suformuotomis ant komercinio silicio saulės elemento pridėjus papildomą ITO dangą optinėms savybėms. Tam buvo panaudoti 4 skirtingi ITO lūžio rodiklio spektrai.

Buvo gauta, jog mažesnis ITO lūžio rodiklis (1.8 prie 632 nm) lemia siauresnius, mėlynai paslinktus ir žemesnius atspindžio maksimumus, lyginant su aukštesniu ITO lūžio rodikliu (2.07 prie 632nm). Kita vertus buvo parodyta, jog šie skirtingi spektrai leidžia gauti panašius atspalvius, su nedideliais atspalvio postūmiais priklausomai nuo antirefleksinės dangos storio. Didinant ITO dangos storį CIE spalvų erdvėje taškai brėžia į elipsę panašias kreives, nulemiančias periodinį kolorimetrinių parametru kitimą nuo storio.

Šio skyriaus rezultatai leido suformuoti antrąjį ginamąjį teiginį.

Antrasis ginamasis teiginys. ITO metalo oksido, naudojamo dvigubo sluoksnio antirefleksinėms silicio saulės elementų dangoms suformuotoms ant $\text{SiN}_x\text{:H}$ viršaus, lūžio rodiklio derinimas leidžia sukurti žemesnes, mėlynai pasislinkusias ir siauresnes smailes paviršiaus atspindžio spektre, kai ITO lūžio rodiklis yra mažesnis (1,8 ties 632 nm), lyginant su didesniu lūžio rodikliu (2,07 ties 632 nm). Tai lemia aukštesnę spalvos ryškumą, esant didesniam ITO lūžio rodikliui, tačiau atspalviai ir spalvos grynumas išlieka panašūs.

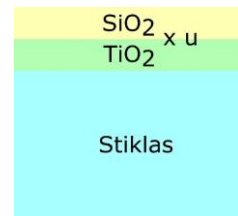
8.4 Funkciniai skaidrūs oksidai Bragg reflektorių struktūroms fotovoltiniams saulės elementams formuoti

Šiame skyriuje bus pristatytas kitas saulės elementų „spalvinimo“ metodas, naudojant taip vadinamus Bragg reflektorius [111]. Tokias struktūras galima formuoti nebūtinai ant saulės elemento, tačiau taip pat ir ant stiklo, taip išplečiant spalvos plotą nuo saulės elemento (lyginant su antirefleksinėmis dangomis) iki viso modulio ploto. Taip pat galima tikėtis aukštesnių atspindžio smailių norimoje spektro srityje ir mažesnių kitose.

Taigi, šiame skyriuje pirmiausia naudojant skaitmeninius modeliavimus su pernašos matricos metodu buvo surasta optimali Bragg reflektoriaus struktūra fotovoltiniams saulės elementams spalvinti. Vėliau dangos buvo eksperimentiškai realizuotos ant stiklo padėklų iš zolių gelių tirpalų su įmerkimo metodika. Technologijos tinkamumas moduliams buvo įrodytas pagaminant keletą mini moduliukų ir juos charakterizavus. Galiausiai buvo atliekama kolorimetrinė analizė ir palyginama su komerciniais spalvotais saulės elementais bei šio darbo pirmuosiuose dviejuose skyriuose aprašytais dvigubomis antirefleksinėmis dangomis. Iš šio skyriaus rezultatų buvo suformuotas trečiasis ginamasis teiginys.

8.4.1 Modeliavimo metodika

Tiriamąjį Bragg reflektoriaus schema pavaizduota Pav. 13. u – tai aukšto ir žemo lūžio rodiklių sluoksnių periodų skaičius. Šiame darbe tirsime $u = 1.5, 2, 2.5, 3$ vertes, siekiant kompromiso tarp struktūros savybių ir eksperimentinio paprastumo bei mastelio didinimo galimybių. TiO_2 čia yra aukšto lūžio rodiklio oksidas, o SiO_2 yra žemo lūžio rodiklio metalo oksidas.



Pav. 13. Bragg reflektoriaus struktūra.

Atspindžio maksimumo vertė yra vienas iš pagrindinių tokio tipo filtrų parametras. Siekiant palyginti šio parametro vertes prie pasirinktų u verčių buvo pasinaudota Boxuan ir kolegų suformuluota lygtimi [12]:

$$R = \left(\frac{1 - n_s/n_a (n_{hi}/n_{lo})^{2u}}{1 + n_s/n_a (n_{hi}/n_{lo})^{2u}} \right)^2, \quad (59)$$

Čia n_s , n_a , n_{hi} , and n_{lo} yra padėklo, aplinkos, aukšto ir žemo lūžio rodiklio medžiagų lūžio rodiklio vertės. Tačiau ši lygtis tinkama tik sveikoms u vertėms. Esant realioms u vertėms: $u=1.5$ ir $u=2.5$ buvo pasinaudota pernašos matricos metodu [76] ir skaičiuoti tokių struktūrų atspindžio spektrai. Šis metodas buvo realizuotas naudojant Steven J. Byrnes sukurtą python

programavimo paketą [63]. Modeliuojant pernašos matricos metodu dangų storiai buvo suderinti pagal Bragg'o sąlygą:

$$\frac{\lambda_0}{4} = nd. \quad (60)$$

kur λ_0 – yra maksimumo bangos ilgis, n – lūžio rodiklis, d – storis.

Siekiant įvertinti padidėjusius nuostolius dėl atspindžio buvo skaičiuojami trumpojo jungimo srovės tankio nuostoliai pagal formulę:

$$J_{sc} = -q \int_{\lambda_1}^{\lambda_2} R(\lambda) \cdot IQE(\lambda) \cdot \phi_{ph,\lambda} d\lambda, \quad (61)$$

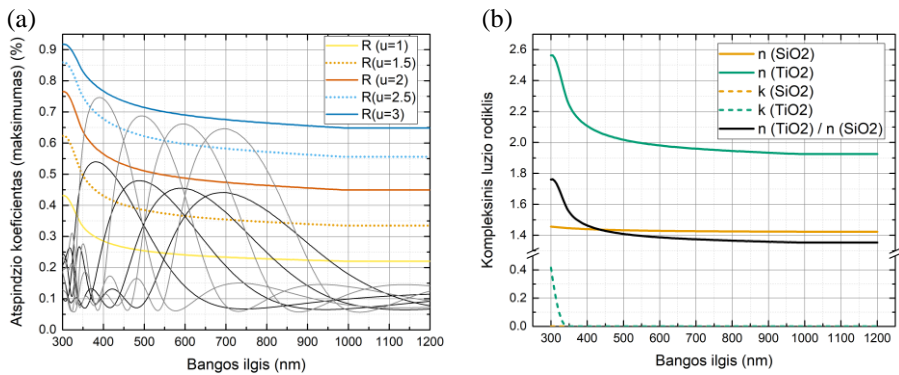
$$\phi_{ph,\lambda} = S(\lambda)(AM1.5G) \frac{\lambda}{hc}, \quad (62)$$

kur $\phi_{ph,\lambda}$ yra fotonų srautas (fotonų skaičius/s·m²) (AM1.5G saulės spektras), $IQE(\lambda)$ – vidinis kvantinis našumas, $R(\lambda)$ – atspindžio koeficientas, $S(\lambda)$ – galios tankis (W/m²).

8.4.2 Simuliacijos rezultatai

Modeliavimų metu gauti atspindžio spektrai bei pagal (55) formulę skaičiuoti atspindžio maksimumo pasiskirstymai nuo bangos ilgio pavaizduoti Pav. 14. Brūkšnine linija pavaizduotos kreivės yra su realiomis parametro u vertėmis pagal tą pačią lygtį, jos atidėtos tam, kad matyti tarpines vertes.

Grafike matome, jog atspindžio spektrai su nelyginiu skaičiumi dangų (nesveikomis parametro u vertėmis), turi beveik tokio pat aukščio maksimumą, kaip ir su lyginėmis u vertėmis. Ši tendencija, leidžia apsiriboti nelyginiu metalų oksidų skaičiumi, nes technologiškai tai paprasčiau ir pigiau, o efektyvumo prasme, skirtumas yra nežymus. Atspindžio maksimumo mažėjimas didėjant bangos ilgiui gali būti paaškinamas metalo oksidų lūžio rodiklių santykio mažėjimu (didėjant bangos ilgiui). Šie santykiai tiesiogiai proporcingai atspindžio maksimumo vertėmis pagal (55) formulę.



Pav. 14. Paveikslėlio (a) dalyje pavaizduotas atspindžio koeficiento nuo bangos ilgio pasiskirstymas su pernašos matrica modeliuotoms struktūroms kai parametras $u=1.5$ ir $u=2.5$, bei pagal (55) lygtį skaičiuota atspindžio maksimumo priklausomybė nuo bangos ilgio kai $u=1$, $u=2$ ir $u=3$. Paveikslėlyje (b) pavaizduoti TiO_2 ir SiO_2 lūžio rodiklių pasiskirstymai gauti iš elipsometrijos skaičiavimų pagamintiems bandiniams su šių oksidų dangomis.

Tolesniu žingsniu buvo įvertinamas šių atspindžio charakteristikų poveikis saulės elemento elektrinėms charakteristikoms pagal (57) lygtį. Atlikus šiuos skaičiavimus gauta, jog J_{SC} nuostoliai varijuoja nuo 16 iki 33% skirtingiems λ_0 , o skirtumas tarp penkiasluoksnės ir trisluoksnės struktūros yra nuo 4 iki 9.5% (detaliau angliškoje versijoje).

Remiantis šio skyriaus rezultatais buvo nuspręsta, jog trijų sluoksnių struktūra sudaryta iš $\text{TiO}_2/\text{SiO}_2/\text{SiO}_2$ ir suformuota ant stiklo padėklo yra pakankama ir efektyvi siekiant tikslingai keisti saulės elemento optines charakteristikas bei spalvą.

8.4.3 Bandinių ruošimas

TiO_2 zolių gelių tirpalas buvo ruošiamas iš titano butoksido pirmtako (angl. titanium butoxide - TBOT), HCl, H_2O ir etanolio 1:1:0.2:23 moliniais santykiais (atitinkamai). Tuomet jis maišomas valandą ir paliekamas 24 val. sendinimui. Panašiai SiO_2 zolių gelių tirpalas buvo gaminamas naudojant tetraetil ortosilikatą (angl. tetraethyl orthosilicate - TEOS), HCl ir etanolį 1:0.00022:12 moliniais santykiais (atitinkamai). Jis buvo maišomas 60°C temperatūroje 1 val., o paskui atvėsinaamas kambario temperatūroje.

Bragg reflektorių struktūros buvo formuojamos ant 5×5 cm dydžio stiklo padėklų naudojant įmerkimo metodiką. Po kiekvieno sluoksnio bandinys buvo dedamas į 45°C krosnelę 15 min. Uždengus visas 3 dangas, jos buvo atkaitinamos 110°C dvi val., pagal Langlet ir kolegų rezultatus [79].

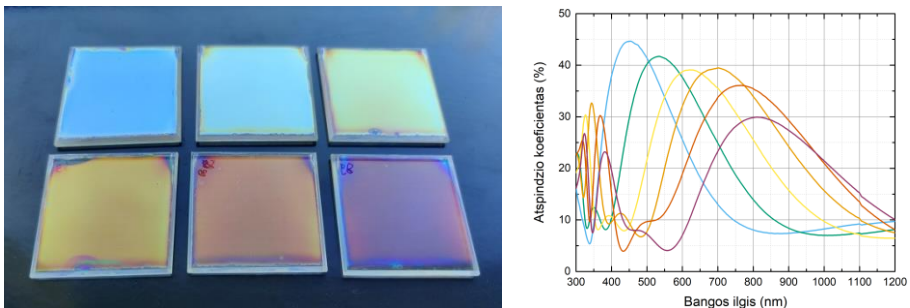
Saulės moduliam buvo naudojami 2.5×2.5 cm dydžio PERC (passivated emitter and rear contact) technologijos saulės elementai.

8.4.4 Eksperimentinis fotovoltinių struktūrų su Bragg reflektoriais realizavimas

Naudojantis Bragg sąlyga buvo parinkti technologinio proceso parametrai, tam kad gauti dangas su atspindžio maksimumo bangos ilgiais: $\lambda_0 = 454, 534, 621, 701, 766$ ir 810 nm. Tuomet remiantis modeliavimų rezultatais iš zolių gelių tirpalų įmerkimo metodika buvo suformuotos 3 sluoksnių dangos. Gauti bandiniai pavaizduoti Pav. 15 (a).

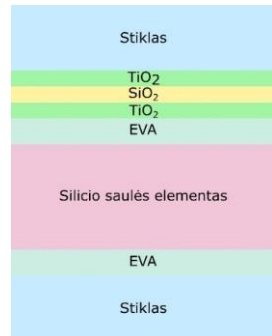
Paveikslėlyje matomos 6 gana ryškios skirtingos spalvos: mėlyna, žalsva, gelsva, oranžinė, persikinė, violetinė. Suformuoti sluoksniai gana homogeniški, netolygumai matomi tik kraštuose. Tikėtina, kad kraštuose atsirandantys nehomogeniškumai yra dėl skirtingų zolių gelių tirpalo tekėjimo greičių skirtumo centre ir prie padėklo krašto.

Paveikslėlyje (b) matome šių bandinių atspindžio spektrus, su smailės maksimumo aukščiais nuo maždaug 45 iki 30%, kurie mažėja didėjant bangos ilgiui. Matome, jog atspindžio maksimumo raudonasis postūmis leidžia tikslingai keisti šios struktūros spalvą, panašiai kaip su antirefleksinėmis dangomis pirmuosiuose skyriuose. Maksimumo aukščio mažėjimas sietinas su $\text{TiO}_2/\text{SiO}_2$ lūžių rodiklių santykio mažėjimu (Pav. 14 (b)).



Pav. 15. Paveikslėlyje (a) šeši 5x5 cm dydžio bandiniai su Bragg reflektorių struktūromis ($\lambda_0 = 454, 534, 621, 701, 766$ ir 810 nm). Paveikslėlyje (b) jų atspindžio spektrai.

Tolesniu žingsniu buto patikrintas šios idėjos tinkamumas saulės moduliams. Todėl spalvoti stiklai buvo sulaminuoti pagal schemą parodytą Pav. 16. Gauti mini moduliai pavaizduoti Pav. 17a. Svarbu pastebėti, kad moduliams buvo naudoti panašūs bet neidentiški λ_0 bandiniai. Palyginimui taip pat buvo sulaminuoti moduliukai su komerciniais spalvotais saulės elementais ir pavaizduoti Pav. 17b.

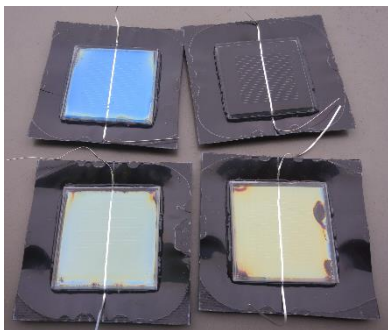


Pav. 16. Laminuoto saulės elemento su Bragg reflektoriais struktūra.

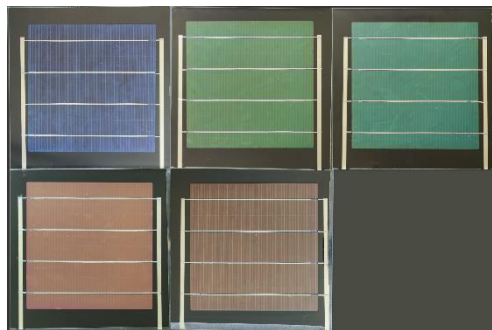
Laminuoti moduliukai buvo charakterizuoti su saulės imitatoriumi ir jų J-V charakteristikos pavaizduotos Pav. 18.

Išmatuoti šių mini saulės moduliukų efektyvumai: 18.75% (kontrolinis, juodas), 17.2% (mėlynas), 17.13 (žalsvas) ir 16.52 (gelsvas), tai reikštų efektyvumo nuostolius iki 12% reliatyvios vertės. Tuo tarpu moduliai su spalvotais komerciniais saulės elementais turi panašius, bet šiek tiek mažesnius efektyvumus: nuo 13 iki 18.4%. Svarbu pastebėti, jog Bragg reflektorių struktūros gali būti naudojamos su bet kokiais saulės elementais. Dėl to pakeičiant 18.4% efektyvumo fotovoltinius elementus pavyzdžiui 24%, kas šiuo metu yra rinkos vidurkis [11], galima būtų tikėtis didesnių nei 21% našumų.

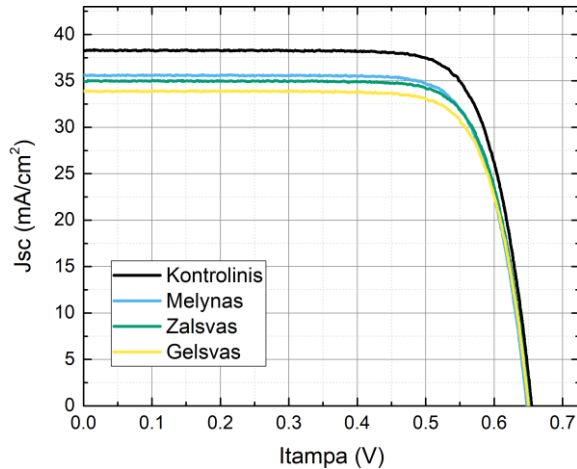
(a)



(b)



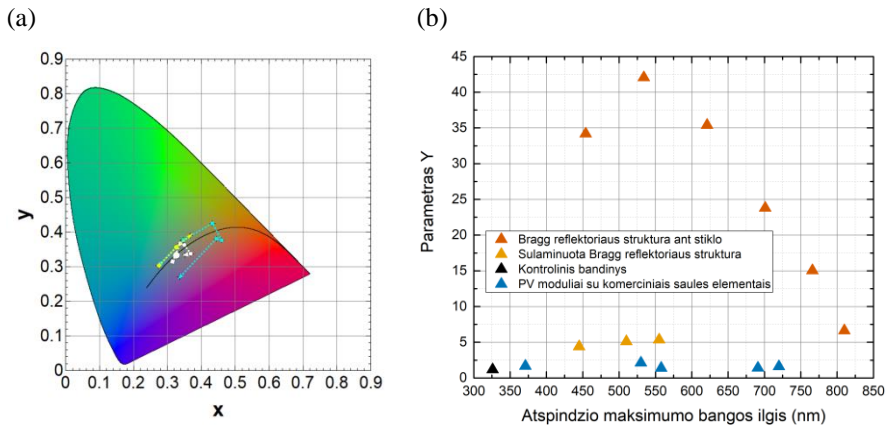
Pav. 17. Laminuotos Bragg reflektorių struktūros, bei moduliukai su komerciniais spalvotais saulės elementais [78].



Pav. 18. Sulaminuotų fotovoltinių moduliukų su Bragg reflektorių struktūromis J-V charakteristikos.

8.4.5 Fotovoltinių struktūrų su Bragg reflektoriais kolorimetrinė analizė

Toliau šiame skyriuje buvo atliekama kolorimetrinė analizė, tam kad palyginti spalvas kiekybiškai. Tam buvo nubraižyti du grafikai: CIE koordinatės CIE erdvėje (Pav. 19 (a)), bei parametro Y priklausomybė nuo atspindžio maksimumo bangos ilgio (Pav. 19 (b)). Kairiajame paveiksle atidėtos Bragg reflektorių struktūros prieš laminavimą (žydra) ir po laminavimo (geltona) bei sulaminuoti saulės moduliai su spalvotomis komercinėmis saulės celėmis (balta).



Pav. 19. Paveikslėlyje (a) pavaizduotos Bragg reflektorių struktūrų CIE koordinatės prieš laminavimą (žydra) ir po laminavimo (geltona) bei sulaminuoti saulės moduliai su spalvotomis komercinėmis saulės celėmis (balta) [78]. Paveikslėlyje (b) atidėta spalvos ryškumą apibūdinančio parametro Y priklausomybė nuo atspindžio maksimumo bangos ilgio.

Analizuojant Pav. 19 (a) tarp laminuotų ir nelaminuotų Bragg reflektorių struktūrų aiškaus skirtumo nesimato, taškai persikloja. Tačiau galima pastebėti, jog laminuoti moduliai su komerciniais saulės elementais yra arčiau D65 šviesos šaltinio ir dėl to pasižymi mažesniu spalvos grynumu.

Tuo tarpu paveikslėlio (b) dalyje matome, gana aiškia tendencija. Nelaminuotos Bragg reflektorių struktūros turi aukščiausias šio parametro vertes, kurios gerokai sumažėja po laminavimo, tačiau vistiek išlieka 2-3 kartus didesnės nei moduliukams su spalvotais komerciniais saulės elementais.

8.4.6 Spalvos jautrumas funkcinių oksidų lūžio rodiklio ir storio nuokrypiams

Šiame skyriuje buvo siekiama įvertinti kokią įtaką siūlomos technologijos funkcinių oksidų parametrai daro spalvai. Tam tikslui buvo įvedami lūžio rodiklio bei sluoksnių storių nuokrypiai nuo optimalios Bragg sąlygos (60). Įtaka spalvai buvo vertinama pasinaudojant ΔE parametru, apibrėžtų tarptautinės apšvietumo komisijos (International Commission on Illumination – CIE) [61]. Buvo lyginama šio parametro vertė, bei sRGB gamos spalvos struktūroms su ir be inicijuotų nuokrypių nuo Bragg sąlygos (lyginama su kontroliniu bandiniu, be minėtų nuokrypių). Sluoksnio storis buvo varijuojamas trim skirtingais būdais (nuo bendro visų oksidų sluoksnio): išoriniam TiO_2 , SiO_2 ir abiem TiO_2 sluoksniams. Rezultatai su lūžio rodiklio nuokrypiais pavaizduoti lentelėje (Lentelė 3).

Keičiant funkcinių oksidų lūžio rodiklius $n=\pm 0.1$, ΔE vertės yra tarp 8.4 ir 9.9, o kai $n=\pm 0.05$, tai šios vertės kinta nuo 4.3 iki 5.3. Šie rezultatai rodo, jog TiO_2 turi stipresnę įtaką šiam parametrai. Be to, lūžio rodiklių sumažėjimas tarp šių metalo oksidų taip pat lemia didesnius ΔE . Lyginant šių nuokrypių įtaką spalvai sRGB skalėje, nesunku atskirti šiuos atspalvius nuo kontrolinio. Todėl galima daryti išvadą, jog siekiant kad spalva nesiskirtų reikalinga, kad lūžio rodiklio pokyčiai neviršytų ± 0.05 .

Lentelė 3. Suskaičiuotos ir palygintos ΔE (CIE2000) vertės ir sRGB skirtingiems lūžio rodiklių nuokrypiams.

Bandinys	ΔE (CIE2000)	Spalvos: bandomoji/kontrolinė (sRGB)	
nSiO ₂ -0.1	8.8612		
nSiO ₂ -0.05	4.6292		
nSiO ₂ +0.1	8.4435		
nSiO ₂ +0.05	4.2791		
nTiO ₂ +0.1	9.8243		
nTiO ₂ +0.05	4.793		
nTiO ₂ -0.1	9.876		
nTiO ₂ -0.05	5.296		

Toliau bus pristatyti sluoksnio storio nuokrypių įtaka spalvai (Lentelė 4). Matome, kad ΔE kinta nuo maždaug 2 iki 38, priklausomai nuo Δd . Spalvą sunkiausia atskirti kai $\Delta d = \pm 1\%$, o ΔE kinta nuo 2 iki 4.5. Šio parametro vertės didžiausios kai kinta vieno išorinio TiO₂ storis, mažesnės, kai kinta abiejų TiO₂ storių ir mažiausios kintant SiO₂ dangos storiui. Iš šių rezultatų galima daryti išvadą, kad galimi storio nuokrypiai turi būti mažesni nei 1% nuo bendro funkcinių oksidų sluoksnių storių sumos.

Lentelė 4 Suskaičiuotos ir palygintos ΔE (CIE2000) vertės ir sRGB skirtingiems sluoksnio storių nuokrypiams.

Δd^*	Kintamasis: išorinis TiO ₂		Kintamasis: SiO ₂		Kintamasis: abu TiO ₂	
	ΔE	Spalvos: bandomoji/kontrolinė (sRGB)	ΔE	Spalvos: bandomoji/kontrolinė (sRGB)	ΔE	Spalvos: bandomoji/kontrolinė (sRGB)
-15%	38.1		29.7		33.6	
-10%	27.3		21.2		24.1	
-5%	15.7		11.8		13.2	
-2%	7.6		5.7		6.2	
-1%	4.5		3.6		3.8	
1%	3.0		2.0		2.2	
2%	6.6		4.1		4.4	
5%	18.5		11.4		12.2	
10%	29.8		20.4		22.7	
15%	31.8		21.7		28.7	

Δd^* - sluoksnio storio nuokrypiai visos struktūros funkcinių oksidų sluoksnių storių sumos atžvilgiu.

8.4.7 Apibendrinimas

Šiame skyriuje buvo pristatytas saulės elementų spalvos keitimo metodas, naudojant Bragg reflektorius. Skyriaus pradžioje naudojant pernašos matricos metodą, buvo optimizuota šių filtrų struktūra. Buvo nustatyta, jog trisluoksnė $\text{TiO}_2/\text{SiO}_2/\text{TiO}_2$ struktūra suformuota ant stiklo yra pakankama ir efektyvi siekiant tikslingai keisti saulės elemento optines charakteristikas bei spalvą. Vėliau ši struktūra buvo eksperimentiškai realizuota iš zolių gelių tirpalų, naudojant įmerkimo metodiką. Gautas 6 gana ryškios spalvos su gana aukštu tolygumu. Tokių struktūrų tinkamumas saulės moduliams buvo įrodytas sulaminuojant juos su saulės elementais. Atlikus kolorimetrinę analizę nustatyta, kad šios struktūros turi 2-3 kartus didesnę šviesos ryškumą lyginant su PV moduliais pagamintus naudojant spalvotus komercinius saulės elementus. Tiriant technologinių parametų įtaką spalvai, buvo gauta jog leistini funkcinų metalų oksidų lūžio rodiklio bei storio nuokrypiai yra mažiau nei ± 0.05 and $\pm 1\%$ (atitinkamai).

Šio skyriaus rezultatai leido suformuoti trečiąjį ginamąjį teiginį. *Trečiasis ginamasis teiginys. Optimali Bragg reflektoriaus struktūra, skirta saulės elementų spalvinimui naudojant TiO_2 ir SiO_2 metalo oksidus, susideda tik iš 3 sluoksnių, suformuotų ant stiklo padėklo (stiklas/ $\text{TiO}_2/\text{SiO}_2/\text{TiO}_2$), ir leidžia pasiekti 2-3 kartus didesnę spalvos ryškumą palyginti su moduliais, pagamintais naudojant komercinius spalvotus saulės elementus. Toleruotini technologiniai nuokrypiai nuo kolorimetrinių parametų, kad šių skirtumų mūsų akis neatskirty, yra mažiau nei $\pm 0,05$ lūžio rodiklio spektrui ir mažiau nei apie $\pm 2\%$ sluoksnio storiui.*

8.5 Funkciniai skaidrūs oksidai tandeminiams saulės elementams spalvoti: skaitmeniniai modeliavimai

Paskutiniame šio darbo skyriuje naudojant skaitmeninius modeliavimus buvo tiriamos spalvinimo galimybės tandeminiuose saulės elementuose. Dviejų sandūrų fotovoltinis elementas buvo suformuotas iš germanio kesterito viršutinės sub-celės ir silicio apatinės sub-celės. Išspausdintame straipsnyje buvo taip pat optimizuojama tokio saulės elemento struktūra, ji trumpai pristatyta angliškoje versijoje, santraukoje ją praleisime.

Šiame skyriuje tandeminio saulės elemento spalvinimas buvo atliekamas keičiant funkcinio Al_2O_3 antirefleksinės dangos storį. Buvo analizuojamas spalvos grynumas, ryškumas bei galimi atspalviai keičiant šios dangos storį nuo 0 iki 300 nm. Šio skyriaus rezultatai leido suformuoti darbo ketvirtąjį ginamąjį teiginį.

8.5.1 Modeliavimo metodika

Tandeminio saulės elemento modeliavimai buvo atliekami naudojantis pernašos matricos metodu, bei programa SCAPS (aprašytos angliškoje darbo versijoje skyriuose 3.1 ir 3.2 bei modeliavimo metodika 7.1 ir 7.2 skyriuose). Pirmoji buvo naudojama optiniams modeliavimams, o antroji elektriniams.

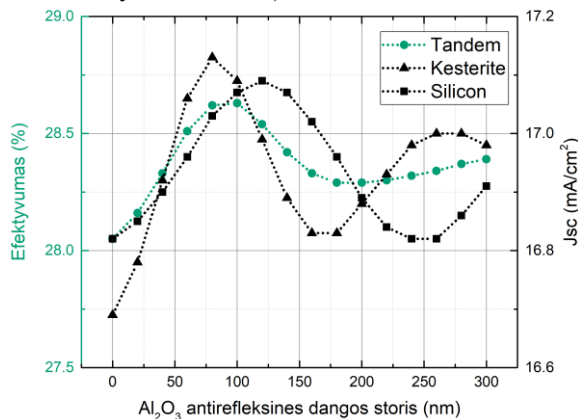
Pirmiausia buvo optimizuojamas CuZnGe(S,Se)/ silicio tandeminis saulės elementas pažingsniui (detaliau angliškoje versijoje). Paskutiniu žingsniu buvo pridėta Al_2O_3 antirefleksinė danga, siekiant sumažinti atspindžius bei ištirti galimybes keisti tokių fotovoltinių prietaisų spalvines charakteristikas.

8.5.2 Tandeminio saulės elemento elektrinių charakteristikų jautrumas antirefleksinės Al_2O_3 dangos storio kitimui

Pav. 20 pavaizduota CZG(S,Se)/Si tandeminio saulės elemento elektrinių parametų (efektyvumo bei trumpojo jungimo srovės tankio) priklausomybė nuo antirefleksinės Al_2O_3 dangos storio.

Matome, kad ši priklausomybė yra periodinė, o efektyvumo maksimumas pasiekiamas kai aliuminio oksido storis yra apie 100 nm. Šiame taške abiejų sub-celių trumpojo jungimo srovės tampa lygios, dėl to nėra srovės ribojimo. Ties 100 nm storiu tandeminio tokio fotovoltinio elemento efektyvumas būtų 28.63%, kas yra 2.5-3.5% daugiau nei geriausi šiuo metu rinkoje esantys saulės elementai (25-26% [32]). Tai nėra didelis laimėjimas, tačiau turint omenyje, jog modeliuota netekstūruota tandeminio saulės elemento struktūra, šis procentas gali būti didesnis.

Taip pat verta pastebėti, kad keičiant antirefleksinės dangos storį nuo 0 iki 300 nm tandeminio elemento efektyvumas kinta gana nedaug: nuo 28.05% iki 28.63% (iki 2% santykinės vertės).



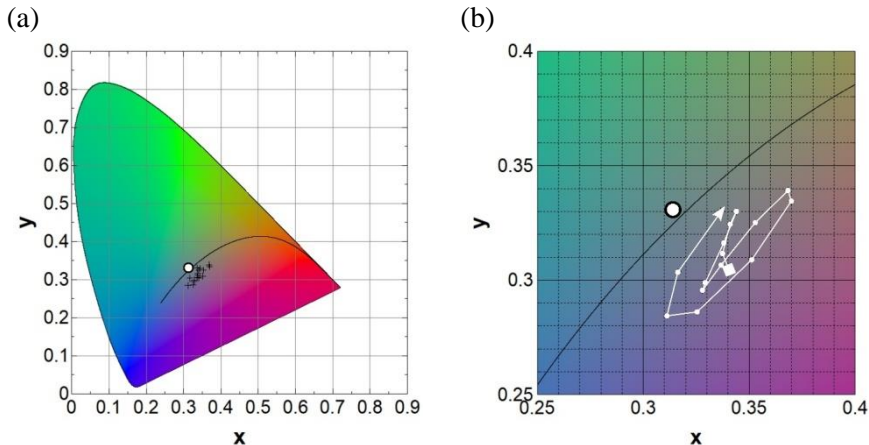
Pav. 20. Tandeminio kesterito/silicio saulės elemento trumpojo jungimo srovės tankio (dešinė Y ašis, juoda)

ir efektyvumo (kairė Y ašis, žalsva) priklausomybės nuo antirefleksinės dangos storio.

8.5.3 Kolorimetrinė analizė ir tinkamumas į pastatus integruotai fotovoltikai

Šalia elektrinių charakteristikų buvo suskaičiuotos ir optinės, bei kolorimetriniai parametrai (xyY ir spalvos grynumas). CIE diagrama pavaizduota Pav. 21. Paveiksėlyje (b) priartinta aktuali sritis su gautais taškais.

Nesunku pastebėti, jog visi taškai sukonzentruoti gana mažoje šios CIE diagramos srityje, netoli taško D65 (šviesos šaltinis [73]). Tai reiškia, kad atspalviai yra riboti, o spalvos grynumas gana mažas. Taip pat galima pastebėti, jog taškai tik tam tikroje funkcinio Al_2O_3 storių srityje brėžia elipsės formos kreivę (kontrastuojant su ankstesniais šio darbo rezultatais), kitose vietose forma netaisyklinga.

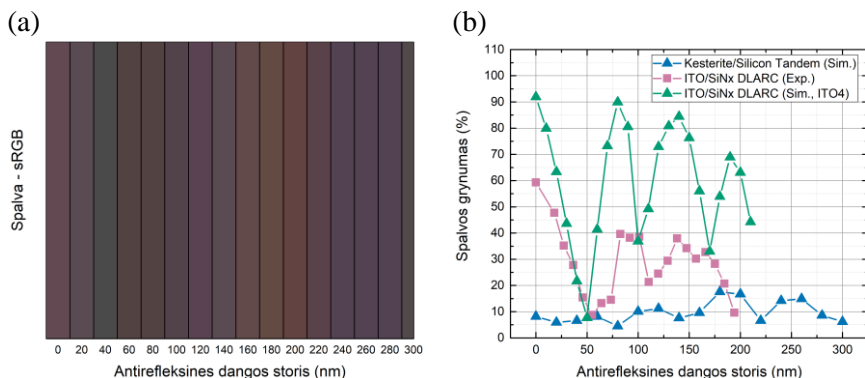


Pav. 21 CIE diagrama, kurioje atidėtos kesterito/silicio tandemo xy koordinatės (a). Paveikslėlyje (b) yra priartinta šio paveikslėlio versija.

Analogiškai kaip ir ankstesniuose skyriuose, xy koordinatės buvo paverstos į sRGB gamą vizualiam atspalvio palyginimui (Pav. 22 (a)), bei suskaičiuotos spalvos grynumo vertės. Jos buvo atvaizduotos nuo antirefleksinės dangos storio Pav. 22 (b).

Kairiajame paveikslėlyje išsiskiria gana ribotas spalvų spektras: gauti rudi bei violetiniai atspalviai, kas koreliuoja su rezultatais aprašytais aukščiau lyginant xy koordinatėjų pozicijas CIE diagramoje. Tuo tarpu dešiniajame paveikslėlyje matome, kad grynumo vertės kinta nuo maždaug 5 iki 20%. Lyginant šias vertes su spalvos grynumu gautu su dvigubomis antirefleksinėmis dangomis, gaunamas gana ryškus skirtumas. Tiek eksperimentiniai tiek teoriniai grynumai naudojant antirefleksines

ITO/SiN_x:H dangas buvo gerokai didesni: teoriniai iki 90%, eksperimentiniai iki 60%.



Pav. 22. Dalyje (a) pavaizduota sRGB gama, o dalyje (b) spalvos grynumas nuo Al₂O₃ antirefleksinės dangos storio (žalia spalva pažymėti modeliuoti, rožine - eksperimentiniai rezultatai su dvigubomis antirefleksinėmis dangomis naudojant ITO, o mėlyna – tandeminių saulės elementų modeliavimo rezultatai).

Apibendrinant galima pasakyti, kad tokiuose ir panašiuose tandeminiuose saulės elementuose spalvos modifikavimas yra apribotas ruda ir violetiniais atspalviais ir gana nedideliu spalvos grynumu iki 20%. Tačiau, svarbu pastebėti, jog tokie saulės moduliai gali surasti savo taikymą pavyzdžiui į pastatus integruotos fotovoltikos srityje, kur šie rudi atspalviai gali puikiai derėti šalia arba vietoj stogo čerpių arba rudų fasadų.

8.5.4 Apibendrinimas

Šiame skyriuje buvo pateikta CuZnGe(S,Se)/silicio tandeminio saulės elemento spalvinimo galimybės bei poveikis elektrinėms charakteristikoms keičiant antirefleksinės Al₂O₃ dangos storį. Didžiausias tokios struktūros efektyvumas (28.63%) buvo gautas naudojant 100 nm storio šio funkcinio metalo oksido sluoksnį. Tai yra maždaug 2.5-3.5% daugiau nei geriausi šiuo metu rinkoje esantys saulės elementai (25-26% [32]). Bendru atveju tai nėra didelis laimėjimas, tačiau turint omenyje, jog modeliuota netekstūruota tandeminio saulės elemento struktūra, šis procentas gali būti didesnis. Taip pat verta pastebėti, jog keičiant Al₂O₃ storį nuo 0 iki 300 nm efektyvumas kinta gana nedaug: nuo 28.05 iki 28.63%. Kas atitinka iki 2% santykinės vertės.

Atlikus kolorimetrinę analizę, nustatyta, jog tokiose ir panašiose tandeminėse struktūrose atspalviai yra riboti ruda ir violetiniais, o spalvos grynumas yra nedidelis (iki 20%). Tai yra gerokai mažiau nei dvigubose antirefleksinėse struktūrose pristatytose pirmuose dviejuose darbo skyriuose (eksperimentiniams bandiniams iki 60%, modeliuotiems iki 90%).

Šio skyriaus rezultatai leido suformuoti ketvirtąjį ginamąjį teiginį.

Ketvirtasis ginamasis teiginys. Antirefleksinio Al_2O_3 sluoksnio storio keitimas nuo 0 iki 300 nm leidžia modifikuoti atspindžio spektrą ir taip pat spalvą kesterito/silicio monolitiniams tandeminiams saulės elementams, su mažesniais nei 2% efektyvumo nuostoliais. Tokie saulės elementai pasižymi gana žemu spalvos grynumu (iki 20%), o galimi atspalviai yra riboti rudais ir violetiniais (ir jų mišiniu).

9. CV OF THE DISSERTATION CANDIDATE



Matas Rudzikas

Gimimo data: 1989 09 09 | Pilietybė: lietuvis, -ė | Lytis: Vyras

Telefono numeris: (+370) 61592859 (Mobilusis telefonas) | El. pašto adresas:

matas.rudzikas@gmail.com

Adresas: Baltupio g. 63-9, LT-08322, Vilnius, Lietuva (Namų)

DARBO PATIRTIS

2013 03 01 – 2014 06 30 Vilnius, Lietuva

INŽINIERIUS FIZINIŲ IR TECHNOLOGIJOS MOKSLŲ CENTRAS (FTMC)

Ištin plonų metalo ir metalo oksido sluoksnių nusodinimas ir tyrimai. Paviršiaus morfologija buvo charakterizuota atominės jėgos mikroskopu (su pažangiu programinės įrangos paketu mikroskopijos vaizdams apdoroti ir analizuoti - SPIP), Ramano spektroskopijos ir rentgeno difrakcijos metodais.

2014 03 01 – DABARTINIS Vilnius, Lietuva

MOKSLO DARBUOTOJAS PERSPEKTYVINIŲ TECHNOLOGIJŲ TAIKOMŲJŲ TYRIMŲ INSTITUTAS (PROTECH)

Taikomieji fotovoltiniai moksliniai tyrimai: spalvotų saulės modulių technologijų kūrimas ir tyrimai, skaitmeniniai modeliavimai, dirbtinio intelekto panaudojimas saulės modulių defektų nustatymui, PV technologijų sandarinimo plėvelių tyrimai, charakterizavimas (spektrometras, profilometras, saulės imitatorius).

Kiti darbai: projektų rašymas, vykdymas.

2014 03 01 – DABARTINIS Vilnius, Lietuva

TECHNOLOGAS-TYRĖJAS UAB "MODERNIOS E-TECHNOLOGIJOS"

Fotovoltinių technologijų tyrimai ir vystymas, projektų rašymas, vykdymas.

IŠSILAVINIMAS IR MOKYMASIS

1996 – 2008 Druskininkai, Lietuva

VIDURINIS IŠSILAVINIMAS Durskininkų senamiesčio vidurinė mokykla

2008 – 2012 Vilnius, Lietuva

BENDROJI FIZIKA (BAKALAURAS) Vilniaus Universitetas

2012 – 2014 Vilnius, Lietuva

MEDŽIAGOTYRA IR PUSLAIDININKIŲ FIZIKA (MAGISTRAS) Vilniaus Universitetas

2017 10 01 – DABARTINIS Vilnius, Lietuva

FIZIKOS DOKTORANTŪRA (STUDENTAS) Fizinių ir technologijos mokslų centras (FTMC)

KALBŲ ŽINIOS

Gimtoji kalba (-os): **LIETUVIŲ KALBA**

Kita (-os) kalba (-os):

	SUPRATIMAS		KALBĖJIMAS		RAŠYMAS
	Klausymas	Skaitymas	Informacijos pateikimas žodžiu	Bendravimas žodžiu	
ANGLŲ KALBA	B2	B2	B2	B2	B2
RUSŲ KALBA	A2	B1	A2	A2	A2

Lygiai: A1 ir A2: pradedantysis vartotojas B1 ir B2: pažengęs vartotojas C1 ir C2: įgudęs vartotojas

SKAITMENINIAI ĮGŪDŽIAI

Duomenų analizės ir atvaizdavimo programinė įranga OriginLab | Microsoft Office | Python | C | C++ | |
HTML LaTeX | Skaitmeniniai modeliavimai | pc3d | Sentaurus TCAD

SU DARBU SUSIJĘ ĮGŪDŽIAI

Patirtis PV srityje: Saulės elementų/modulių IV matavimai, elektroluminescenciniai matavimai, IEC 61215 modulių bandymai, optinis charakterizavimas (atspindžio, perleidimo, kvantinė efektyvumas), profilometrija, sluoksnio važros matavimai, magnetroninis dulkinimas, sol-gel, įmerkimo technologija (angl. dipping), pūškimo pirolizė, Bragg reflektorių formavimas ir tyrimai, nanodalelių lazerinė abliacija, saulės modulių galios prognozės bei defektų aptikimo modeliavimai, skaičiavimai.

Projektinės išvykos: 1 mėnuo in SINTEF (Oslos, Norvegija) 2018, 3 mėnesiai IREC (Barselona, Ispanija) 2019-2020, 1 mėnuo IAP-ASM (Kišiniovas, Moldova) 2022, 2 mėnesiai HZB (Berlynas, Vokietija), 1 mėnuo IREC (Barselona, Ispanija).

10. BIBLIOGRAPHY

- [1] Ourworldindata, (n.d.). <https://ourworldindata.org/grapher/energy-consumption-by-source-and-country> (accessed January 16, 2024).
- [2] M. Perez, R. Perez, Update 2022 – A fundamental look at supply side energy reserves for the planet, *Sol. Energy Adv.* 2 (2022) 100014. <https://doi.org/10.1016/j.seja.2022.100014>.
- [3] Fraunhofer ISE, PHOTOVOLTAICS REPORT, 2023. <https://www.statista.com/statistics/483609/solar-pv-installations-cumulative-share-worldwide-by-region/>.
- [4] J.F. Lelièvre, B. Kafle, P. Saint-Cast, P. Brunet, R. Magnan, E. Hernandez, S. Pouliquen, F. Massines, Efficient silicon nitride SiNx:H antireflective and passivation layers deposited by atmospheric pressure PECVD for silicon solar cells, *Prog. Photovoltaics Res. Appl.* 27 (2019) 1007–1019. <https://doi.org/10.1002/pip.3141>.
- [5] I. Tobías, A. El Moussaoui, A. Luque, Colored Solar Cells with Minimal Current Mismatch, 1999. <https://doi.org/10.1109/16.784185>.
- [6] M. Valiei, P.M. Shaibani, H. Abdizadeh, M. Kolahdouz, E. Asl Soleimani, J. Poursafar, Design and optimization of single, double and multilayer anti-reflection coatings on planar and textured surface of silicon solar cells, *Mater. Today Commun.* 32 (2022) 104144. <https://doi.org/10.1016/j.mtcomm.2022.104144>.
- [7] K.W.A. Chee, Z. Tang, H. Lü, F. Huang, Anti-reflective structures for photovoltaics: Numerical and experimental design, *Energy Reports.* 4 (2018) 266–273. <https://doi.org/10.1016/j.egy.2018.02.002>.
- [8] Y. Chen, Y. Yang, Z. Feng, P.P. Altermatt, H. Shen, Color modulation of c-Si solar cells without significant current-loss by means of a double-Layer anti-reflective coating, in: *27th Eur. Photovolt. Sol. Energy Conf. Exhib.*, 2012: pp. 2014–2016. <https://doi.org/10.4229/27thEUPVSEC2012-2CV.7.12>.
- [9] M. Li, L. Zeng, Y. Chen, L. Zhuang, X. Wang, H. Shen, Realization of colored multicrystalline silicon solar cells with SiO₂/SiNx:H double layer antireflection coatings, *Int. J. Photoenergy.* 2013 (2013). <https://doi.org/10.1155/2013/352473>.
- [10] L. Zeng, M. Li, Y. Chen, H. Shen, A simplified method to modulate colors on industrial multicrystalline silicon solar cells with reduced current losses, *Sol. Energy.* 103 (2014) 343–349. <https://doi.org/10.1016/j.solener.2014.02.012>.
- [11] ITPRV, International Technology Roadmap for Photovoltaic, 2022. <https://itprv.vdma.org/en/ueber-uns>.
- [12] B. Gao, J.P. George, J. Beckman, K. Neyts, Design, fabrication and characterization of a distributed Bragg reflector for reducing the étendue of a wavelength converting system, *Opt. Express.* 28 (2020) 12837. <https://doi.org/10.1364/oe.391080>.
- [13] A. Fu, H. Gao, P. Petrov, P. Yang, Widely Tunable Distributed Bragg Reflectors Integrated into Nanowire Waveguides, *Nano Lett.* 15

- (2015) 6909–6913. <https://doi.org/10.1021/acs.nanolett.5b02839>.
- [14] B. Blasi, T. Kroyer, T. Kuhn, O. Hohn, The MorphoColor Concept for Colored Photovoltaic Modules, *IEEE J. Photovoltaics*. 11 (2021) 1305–1311. <https://doi.org/10.1109/JPHOTOV.2021.3090158>.
- [15] A. Soman, A. Antony, Colored solar cells with spectrally selective photonic crystal reflectors for application in building integrated photovoltaics, *Sol. Energy*. 181 (2019) 1–8. <https://doi.org/10.1016/j.solener.2019.01.058>.
- [16] Z. Xu, T. Matsui, K. Matsubara, H. Sai, Tunable and angle-insensitive structural coloring of solar cell modules for high performance building-integrated photovoltaic application, *Sol. Energy Mater. Sol. Cells*. 247 (2022) 111952. <https://doi.org/10.1016/j.solmat.2022.111952>.
- [17] T. Masuda, Y. Kudo, D. Banerjee, Visually attractive and high-power-retention solar modules by coloring with automotive paints, *Coatings*. 8 (2018) 1–7. <https://doi.org/10.3390/coatings8080282>.
- [18] G. Peharz, K. Berger, B. Kubicek, M. Aichinger, M. Grobbauer, J. Gratzler, W. Nemitz, B. Großschädl, C. Auer, C. Prietl, W. Waldhauser, G.C. Eder, Application of plasmonic coloring for making building integrated PV modules comprising of green solar cells, *Renew. Energy*. 109 (2017) 542–550. <https://doi.org/10.1016/j.renene.2017.03.068>.
- [19] E.S. Arinze, B. Qiu, N. Palmquist, Y. Cheng, Y. Lin, G. Nyirjesy, G. Qian, S.M. Thon, Color-tuned and transparent colloidal quantum dot solar cells via optimized multilayer interference, *Opt. Express*. 25 (2017) A101. <https://doi.org/10.1364/oe.25.00a101>.
- [20] H. Agha, Y.-S. Zhang, Y. Geng, J.P.F. Lagerwall, Pixelating Structural Color with Cholesteric Spherical Reflectors, *Adv. Photonics Res.* 4 (2023). <https://doi.org/10.1002/adpr.202200363>.
- [21] K. Sharma, V. Sharma, S.S. Sharma, Dye-Sensitized Solar Cells: Fundamentals and Current Status, *Nanoscale Res. Lett.* 13 (2018). <https://doi.org/10.1186/s11671-018-2760-6>.
- [22] J.H. Lee, Y. Song, K. Jung, M.J. Lee, Colored MAPbI₃ perovskite solar cells based on SnO₂–SiO₂ distributed Bragg reflectors, *Mater. Lett.* 282 (2021) 128828. <https://doi.org/10.1016/J.MATLET.2020.128828>.
- [23] Y. Geng, R. Kizhakidathazhath, J.P.F. Lagerwall, Encoding Hidden Information onto Surfaces Using Polymerized Cholesteric Spherical Reflectors, *Adv. Funct. Mater.* 31 (2021). <https://doi.org/10.1002/adfm.202100399>.
- [24] E. Afshari Pour, C. Shafai, Tailoring the refractive index of ITO thin films by genetic algorithm optimization of the reactive DC-sputtering parameters, in: *Oxide-Based Mater. Devices VIII*, SPIE, 2017: p. 101050I. <https://doi.org/10.1117/12.2251562>.
- [25] H. Lee, H.J. Song, Current status and perspective of colored

- photovoltaic modules, *Wiley Interdiscip. Rev. Energy Environ.* 2020 (2021) 1–31. <https://doi.org/10.1002/wene.403>.
- [26] C. Gao, D. Du, D. Ding, F. Qiao, W. Shen, A review on monolithic perovskite/c-Si tandem solar cells: progress, challenges, and opportunities, *J. Mater. Chem. A.* 10 (2022) 10811–10828. <https://doi.org/10.1039/D2TA01470J>.
- [27] W. Shockley, H.J. Queisser, Detailed Balance Limit of Efficiency of p-n Junction Solar Cells, *J. Appl. Phys.* 32 (1961) 510–519. <https://doi.org/10.1063/1.1736034>.
- [28] K. Yoshikawa, H. Kawasaki, W. Yoshida, T. Irie, K. Konishi, K. Nakano, T. Uto, D. Adachi, M. Kanematsu, H. Uzu, K. Yamamoto, Silicon heterojunction solar cell with interdigitated back contacts for a photoconversion efficiency over 26%, *Nat. Energy* 2017 25. 2 (2017) 1–8. <https://doi.org/10.1038/nenergy.2017.32>.
- [29] Research and Markets, Building Integrated Photovoltaics (BIPV) Market - Global Outlook and Forecast 2021-2026, (2021).
- [30] n-tech Research, BIPV Technologies and Markets: 2015-2022, 2015.
- [31] The PVSITES Consortium, BIPV market and stakeholder analysis and needs Project report, (2016) 52. <file:///C:/Users/xcybe/Downloads/report-bipv-market-and-stakeholder-analysis-and-ne.pdf%0Ahttps://www.pvsites.eu/>.
- [32] M.A. Green, E.D. Dunlop, M. Yoshita, N. Kopidakis, K. Bothe, G. Siefer, X. Hao, Solar cell efficiency tables (Version 63) Martin, *Prog. Photovoltaics Res. Appl.* (2023). <https://doi.org/10.1002/pip.3750> SHOR.
- [33] J. Zhuang, J. Wang, F. Yan, Review on Chemical Stability of Lead Halide Perovskite Solar Cells, Springer Nature Singapore, 2023. <https://doi.org/10.1007/s40820-023-01046-0>.
- [34] The European Commission, Communication from the Commission to the European Parliament, the Council, the European Economic and Social Committee and the Committee of the Regions on the 2017 list of Critical Raw Materials for the EU, (n.d.). <https://eur-lex.europa.eu/legal-content/EN/ALL/?uri=COM:2017:0490:FIN> (accessed May 25, 2023).
- [35] S. Giraldo, Z. Jehl, M. Placidi, V. Izquierdo-Roca, A. Pérez-Rodríguez, E. Saucedo, Progress and Perspectives of Thin Film Kesterite Photovoltaic Technology: A Critical Review, *Adv. Mater.* 31 (2019). <https://doi.org/10.1002/adma.201806692>.
- [36] K. Shen, G. Jia, X. Zhang, Z. Jiao, The electronic structure, elastic and optical properties of $\text{Cu}_2\text{ZnGe}(\text{SexS}_{1-x})_4$ alloys: density functional calculations, *Mol. Phys.* 114 (2016) 2948–2957. <https://doi.org/10.1080/00268976.2016.1211326>.
- [37] M.A. Green, E.D. Dunlop, G. Siefer, M. Yoshita, N. Kopidakis, K. Bothe, X. Hao, Solar cell efficiency tables (Version 61), *Prog. Photovoltaics Res. Appl.* 31 (2023) 3–16.

- <https://doi.org/10.1002/pip.3646>.
- [38] Z.J.L.-K. Alex Jimenez-Arguijo, Axel Gon Medaille, Alejandro Navarro-Güell, Maykel Jimenez-Guerra, Kunal J. Tiwari, Marcel Placidi, Moleko Samuel Mkehlane, Emmanuel Iwuoha, Alejandro Perez-Rodriguez c, e, Edgardo Saucedo, Sergio Giraldo, Setting the Baseline for the Modelling of Kesterite Solar Cells: The Case Study of Tandem Application, *Sol. Energy Mater. Sol. Cells.* (2023). <https://doi.org/10.2139/ssrn.4240797>.
- [39] V. Sivathanu, R. Thangavel, T.R. Lenka, Modeling and performance optimization of two-terminal Cu₂ZnSnS₄–silicon tandem solar cells, *Int. J. Energy Res.* 45 (2021) 10527–10537. <https://doi.org/10.1002/er.6540>.
- [40] Elsevier, Contributor Roles Taxonomy, (n.d.). <https://www.elsevier.com/researcher/author/policies-and-guidelines/credit-author-statement> (accessed January 18, 2024).
- [41] K.R. McIntosh, S.C. Baker-Finch, OPAL 2: Rapid optical simulation of silicon solar cells, *Conf. Rec. IEEE Photovolt. Spec. Conf.* (2012) 265–271. <https://doi.org/10.1109/PVSC.2012.6317616>.
- [42] A. Luque, S. Hegedus, *Handbook of Photovoltaic Science and Engineering*, John Wiley & Sons: Hoboken, NJ, USA, 2011. <https://doi.org/10.1002/9780470974704>.
- [43] W. van Sark, A. Reinders, P. Verlinden, A. Freundlich, Photovoltaic Solar Energy FROM FUNDAMENTALS TO APPLICATIONS, *Technol. Learn. Energy Sect.* 5 (2017) 733. <http://www.elgaronline.com/view/9781848448346.00017.xml>.
- [44] H.A. Macleod, *Thin film optical filters*, 5th editio, CRC Press Taylor & Francis Group: Boca Raton, FL, USA, 2018. [https://doi.org/10.1016/0040-6090\(69\)90094-7](https://doi.org/10.1016/0040-6090(69)90094-7).
- [45] E. Hecht, *Optics*, 2017. <https://doi.org/10.1119/1.3274347>.
- [46] M. Rudzikas, A. Šetkus, M. Stange, J. Ulbikas, A. Ulyashin, Simple interference based colorization of Si based solar cells and panels with ITO/SiN_x:H double layer antireflective coatings, *Sol. Energy.* 207 (2020) 218–227. <https://doi.org/10.1016/j.solener.2020.06.091>.
- [47] H.K. Raut, V.A. Ganesh, A.S. Nair, S. Ramakrishna, Anti-reflective coatings: A critical, in-depth review, *Energy Environ. Sci.* 4 (2011) 3779–3804. <https://doi.org/10.1039/c1ee01297e>.
- [48] H.K. Raut, V.A. Ganesh, A.S. Nair, S. Ramakrishna, Anti-reflective coatings: A critical, in-depth review, *Energy Environ. Sci.* 4 (2011) 3779–3804. <https://doi.org/10.1039/c1ee01297e>.
- [49] A.E. Danks, S.R. Hall, Z. Schnepf, The evolution of “sol-gel” chemistry as a technique for materials synthesis, *Mater. Horizons.* 3 (2016) 91–112. <https://doi.org/10.1039/c5mh00260e>.
- [50] K. Han, J.H. Kim, Reflectance modulation of transparent multilayer thin films for energy efficient window applications, *Mater. Lett.* 65 (2011) 2466–2469. <https://doi.org/10.1016/j.matlet.2011.05.006>.

- [51] M. Anaya, A. Rubino, M.E. Calvo, H. Míguez, Solution processed high refractive index contrast distributed Bragg reflectors, *J. Mater. Chem. C* 4 (2016) 4532–4537. <https://doi.org/10.1039/c6tc00663a>.
- [52] A.C. Pierre, *Introduction to Sol-Gel Processing*, 2020. <https://doi.org/10.1007/978-3-030-38144-8>.
- [53] D. Levy, M. Zayat, *The Sol-Gel Handbook*, 2015. <https://doi.org/10.1002/9783527670819>.
- [54] C.J. Brinker, A.J. Hurd, P.R. Schunk, G.C. Frye, C.S. Ashley, Review of sol-gel thin film formation, *J. Non. Cryst. Solids*. 147–148 (1992) 424–436. [https://doi.org/10.1016/S0022-3093\(05\)80653-2](https://doi.org/10.1016/S0022-3093(05)80653-2).
- [55] C. Glynn, C. O’Dwyer, Solution Processable Metal Oxide Thin Film Deposition and Material Growth for Electronic and Photonic Devices, *Adv. Mater. Interfaces*. 4 (2017). <https://doi.org/10.1002/admi.201600610>.
- [56] O. Milton, *The Materials Science of Thin Films*, Academic Press, 1992.
- [57] D.M. Mattox, *HANDBOOK OF PHYSICAL VAPOR DEPOSITION (PVD) Film Formation , Adhesion , Surface*, Noyes Publications, 1998.
- [58] R.F.M. Lange, Y. Luo, R. Polo, J. Zahnd, The lamination of (multi)crystalline and thin film based photovoltaic modules, *Prog. Photovoltaics Res. Appl.* 19 (2011) 127–133. <https://doi.org/10.1002/pip.993>.
- [59] D. Wu, Investigation of the reliability of the encapsulation system of photovoltaic modules, 2015. <https://dspace.lboro.ac.uk/2134/18051>.
- [60] A.K.R. Choudhury, Principles of colour perception, in: *Princ. Colour Appear. Meas.*, Elsevier, 2014: pp. 144–184. <https://doi.org/10.1533/9780857099242.144>.
- [61] CIE, Part 6: CIEDE2000 Colour-difference formula, in: *Part 6 CIEDE2000 Colour-Difference Formula*, the International Organization for Standardization, 2014.
- [62] W. Mokrzycki, M. Tatol, Color difference Delta E - A survey., *Mach. Graph. Vis.* 20 (2011) 383–411.
- [63] S.J. Byrnes, Multilayer optical calculations, (2016) 1–20. <http://arxiv.org/abs/1603.02720>.
- [64] M. Burgelman, K. Decock, S. Khelifi, A. Abass, Advanced electrical simulation of thin film solar cells, in: *Thin Solid Films*, Elsevier, 2013: pp. 296–301. <https://doi.org/10.1016/j.tsf.2012.10.032>.
- [65] M.A. Green, Lambertian light trapping in textured solar cells and light-emitting diodes: Analytical solutions, *Prog. Photovoltaics Res. Appl.* 10 (2002) 235–241. <https://doi.org/10.1002/pip.404>.
- [66] NREL, Reference Air Mass 1.5 Spectra, (n.d.). <https://www.nrel.gov/grid/solar-resource/assets/data/astmg173.xls> (accessed September 5, 2023).
- [67] BENTHAM INSTRUMENTS LTD, *Bentham PVE 300 Manual*, n.d.

- [68] ASTM, Standard Classification for Solar Simulators for Electrical Performance Testing of Photovoltaic Devices, Astm E927. i (2019) 18–23. <https://www.astm.org/e0927-19.html> (accessed January 19, 2024).
- [69] C.T. Sah, R.N. Noyce, W. Shockley, Carrier Generation and Recombination in P-N Junctions and P-N Junction Characteristics, Proc. IRE. 45 (1957) 1228–1243. <https://doi.org/10.1109/JRPROC.1957.278528>.
- [70] B.S. Keith McIntosh, Malcolm Abbott, PV Lighthouse website, (n.d.). <https://www.pvlighthouse.com.au/> (accessed August 3, 2023).
- [71] S. Duttagupta, F. Ma, B. Hoex, T. Mueller, A.G. Aberle, Optimised antireflection coatings using silicon nitride on textured silicon surfaces based on measurements and multidimensional modelling, in: Energy Procedia, 2012: pp. 78–83. <https://doi.org/10.1016/j.egypro.2012.02.009>.
- [72] Z.C. Holman, M. Filipič, A. Descoedres, S. De Wolf, F. Smole, M. Topič, C. Ballif, Infrared light management in high-efficiency silicon heterojunction and rear-passivated solar cells, J. Appl. Phys. 113 (2013). <https://doi.org/10.1063/1.4772975>.
- [73] International Commission on Illumination, D65 Illuminant, (n.d.). <https://cie.co.at/datatable/cie-standard-illuminant-d65> (accessed December 19, 2023).
- [74] Cie, CIE technical report, 2004. [https://doi.org/ISBN 3 901 906 33 9](https://doi.org/ISBN%203%20901%20906%2033%209).
- [75] R.J. Moerland, J.P. Hoogenboom, Subnanometer-accuracy optical distance ruler based on fluorescence quenching by transparent conductors, Optica. 3 (2016) 112. <https://doi.org/10.1364/optica.3.000112>.
- [76] O.S. HEAVENS, Optical properties of thin films, Reports Prog. Phys. 23 (1960).
- [77] P. Malhotra, D.S. Biswas, G.D. Sharma, Calculating short circuit current density (Jsc) from external quantum efficiency (EQE), (2021). <https://doi.org/10.21981/XY24-RV08>.
- [78] LOF SOLAR, Colored commercial solar cells, (n.d.). <http://www.lofsolar.com/Standard-series#4> (accessed December 1, 2022).
- [79] M. Langlet, M. Burgos, C. Coutier, C. Jimenez, C. Morant, M. Manso, Low temperature preparation of high refractive index and mechanically resistant sol-gel TiO₂ films for multilayer Antireflective Coating Applications, J. Sol-Gel Sci. Technol. 22 (2001) 139–150. <https://doi.org/10.1023/A:1011232807842>.
- [80] S.K. Gaddam, R. Pothu, R. Boddula, Advanced polymer encapsulates for photovoltaic devices – A review, J. Mater. 7 (2021) 920–928. <https://doi.org/10.1016/j.jmat.2021.04.004>.
- [81] Solaxess, Solaxess colored sheet for PV, (n.d.). <https://www.solaxess.ch/wp->

- content/uploads/2023/10/brochure_A4_2022_EN.pdf (accessed January 8, 2024).
- [82] Kromatix, (n.d.). <https://kromatix.com/kromatix-glass> (accessed January 6, 2024).
- [83] JSXQ, JSXQ colored glasses, (n.d.). <http://www.jsxq.com/en/home> (accessed January 17, 2024).
- [84] M.D. Haque, M.H. Ali, M.F. Rahman, A.Z.M.T. Islam, Numerical analysis for the efficiency enhancement of MoS₂ solar cell: A simulation approach by SCAP-1D, *Opt. Mater. (Amst)*. 131 (2022) 112678. <https://doi.org/10.1016/j.optmat.2022.112678>.
- [85] S. Khelifi, G. Brammertz, L. Choubrac, M. Batuk, S. Yang, M. Meuris, N. Barreau, J. Hadermann, H. Vrielinck, D. Poelman, K. Neyts, B. Vermang, J. Lauwaert, The path towards efficient wide band gap thin-film kesterite solar cells with transparent back contact for viable tandem application, *Sol. Energy Mater. Sol. Cells*. 219 (2021). <https://doi.org/10.1016/j.solmat.2020.110824>.
- [86] D. Mora-Herrera, M. Pal, J. Santos-Cruz, Theoretical modelling and device structure engineering of kesterite solar cells to boost the conversion efficiency over 20%, *Sol. Energy*. 220 (2021) 316–330. <https://doi.org/10.1016/j.solener.2021.03.056>.
- [87] M. Rashid, N.A. Noor, B. Sabir, S. Ali, M. Sajjad, F. Hussain, N.U. Khan, B. Amin, R. Khenata, Ab-initio study of fundamental properties of ternary ZnO_{1-x}S_x alloys by using special quasi-random structures, *Comput. Mater. Sci.* 91 (2014) 285–291. <https://doi.org/10.1016/j.commatsci.2014.04.032>.
- [88] F. Jafarzadeh, H. Aghili, H. Nikbakht, S. Javadpour, Design and optimization of highly efficient perovskite/homojunction SnS tandem solar cells using SCAPS-1D, *Sol. Energy*. 236 (2022) 195–205. <https://doi.org/10.1016/j.solener.2022.01.046>.
- [89] S.Y. Yu, M.A. Hassan, M.A. Johar, S.W. Ryu, Optical and Structural Analysis of Zinc Oxysulfide Digital Alloys Grown by Atomic Layer Deposition, *J. Korean Phys. Soc.* 73 (2018) 649–655. <https://doi.org/10.3938/jkps.73.649>.
- [90] U. Thi Dieu Thuy, N. Quang Liem -, T. Hoa Nguyen, T. Dieu Thuy Ung, T. Hien Vu, R.E. Treharne, A. Seymour-Pierce, K. Durose, K. Hutchings, S. Roncallo, D. Lane, Optical Design and Fabrication of Fully Sputtered CdTe/CdS Solar Cells, *J. Phys. Conf. Ser.* 286 (2011) 012038. <https://doi.org/10.1088/1742-6596/286/1/012038>.
- [91] O. Aguilar, S. de Castro, M.P.F. Godoy, M. Rebello Sousa Dias, Optoelectronic characterization of Zn_{1-x}Cd_xO thin films as an alternative to photonic crystals in organic solar cells, *Opt. Mater. Express*. 9 (2019) 3638. <https://doi.org/10.1364/ome.9.003638>.
- [92] A.R. Beal, H.P. Hughes, Kramers-Kronig analysis of the reflectivity spectra of 2H-MoS₂, 2H-MoSe₂ and 2H-MoTe₂, *J. Phys. C Solid State Phys.* 12 (1979) 881. [125](https://doi.org/10.1088/0022-</p>
</div>
<div data-bbox=)

3719/12/5/017.

- [93] M.A. Green, Improved silicon optical parameters at 25°C, 295 K and 300 K including temperature coefficients, *Prog. Photovoltaics Res. Appl.* 30 (2022) 164–179. <https://doi.org/10.1002/pip.3474>.
- [94] M.R. Vogt, H. Holst, H. Schulte-Huxel, S. Blankemeyer, R. Witteck, D. Hinken, M. Winter, B. Min, C. Schinke, I. Ahrens, M. Köntges, K. Bothe, R. Brendel, Optical Constants of UV Transparent EVA and the Impact on the PV Module Output Power under Realistic Irradiation, *Energy Procedia*. 92 (2016) 523–530. <https://doi.org/10.1016/J.EGYPRO.2016.07.136>.
- [95] R. Boidin, T. Halenkovič, V. Nazabal, L. Beneš, P. Němec, Pulsed laser deposited alumina thin films, *Ceram. Int.* 42 (2016) 1177–1182. <https://doi.org/10.1016/j.ceramint.2015.09.048>.
- [96] E.D. Palik, *Handbook of optical constants of solids*, Elsevier Inc., 2012. <https://doi.org/10.1016/C2009-0-20920-2>.
- [97] I. Anefnaf, S. Aazou, Y. Sánchez, P. Vidal-Fuentes, R. Fonoll-Rubio, K.J. Tiwari, S. Giraldo, Z.J. Li-Kao, J. Andrade-Arvizu, M. Guc, E. Saucedo, Z. Sekkat, Insights on the limiting factors of Cu₂ZnGeSe₄ based solar cells, *Sol. Energy Mater. Sol. Cells*. 227 (2021). <https://doi.org/10.1016/j.solmat.2021.111106>.
- [98] M.A. Green, E.D. Dunlop, J. Hohl-Ebinger, M. Yoshita, N. Kopidakis, K. Bothe, D. Hinken, M. Rauer, X. Hao, Solar cell efficiency tables (Version 60), *Prog. Photovoltaics Res. Appl.* 30 (2022) 687–701. <https://doi.org/10.1002/pip.3595>.
- [99] C. Ballif, F.J. Haug, M. Boccard, P.J. Verlinden, G. Hahn, Status and perspectives of crystalline silicon photovoltaics in research and industry, *Nat. Rev. Mater.* 2022 78. 7 (2022) 597–616. <https://doi.org/10.1038/s41578-022-00423-2>.
- [100] T. Unold, Accelerating research on novel photovoltaic materials, *Faraday Discuss.* (2022). <https://doi.org/10.1039/d2fd00085g>.
- [101] Y.S. Lee, T. Gershon, O. Gunawan, T.K. Todorov, T. Gokmen, Y. Virgus, S. Guha, Cu₂ZnSnSe₄ thin-film solar cells by thermal co-evaporation with 11.6% efficiency and improved minority carrier diffusion length, *Adv. Energy Mater.* 5 (2015) 2–5. <https://doi.org/10.1002/aenm.201401372>.
- [102] T. Gokmen, O. Gunawan, T.K. Todorov, D.B. Mitzi, Band tailing and efficiency limitation in kesterite solar cells, *Appl. Phys. Lett.* 103 (2013). <https://doi.org/10.1063/1.4820250>.
- [103] I.L. Repins, H. Moutinho, S.G. Choi, A. Kanevce, D. Kuciauskas, P. Dippo, C.L. Beall, J. Carapella, C. Dehart, B. Huang, S.H. Wei, Indications of short minority-carrier lifetime in kesterite solar cells, *J. Appl. Phys.* 114 (2013). <https://doi.org/10.1063/1.4819849>.
- [104] J. Zhou, X. Xu, H. Wu, J. Wang, L. Lou, K. Yin, Y. Gong, J. Shi, Y. Luo, D. Li, H. Xin, Q. Meng, Control of the phase evolution of kesterite by tuning of the selenium partial pressure for solar cells with

- 13.8% certified efficiency, *Nat. Energy* 2023 85. 8 (2023) 526–535. <https://doi.org/10.1038/s41560-023-01251-6>.
- [105] A. Wang, M. He, M.A. Green, K. Sun, X. Hao, A Critical Review on the Progress of Kesterite Solar Cells: Current Strategies and Insights, *Adv. Energy Mater.* 13 (2023). <https://doi.org/10.1002/aenm.202203046>.
- [106] EasyRGB, (n.d.). <https://www.easyrgb.com/en/convert.php> (accessed January 5, 2024).
- [107] S.L. Hille, H.C. Curtius, R. Wüstenhagen, Red is the new blue – The role of color, building integration and country-of-origin in homeowners’ preferences for residential photovoltaics, *Energy Build.* 162 (2018) 21–31. <https://doi.org/10.1016/j.enbuild.2017.11.070>.
- [108] BCC Publishing, *Building-Integrated Photovoltaics (BIPV): Technologies and Global Markets*, 2021.
- [109] J.H. Selj, T.T. Mongstad, R. Søndena, E.S. Marstein, Reduction of optical losses in colored solar cells with multilayer antireflection coatings, *Sol. Energy Mater. Sol. Cells.* 95 (2011) 2576–2582. <https://doi.org/10.1016/j.solmat.2011.03.005>.
- [110] A. Soman, A. Antony, Broad range refractive index engineering of SixNy and SiOxNy thin films and exploring their potential applications in crystalline silicon solar cells, *Mater. Chem. Phys.* 197 (2017) 181–191. <https://doi.org/10.1016/j.matchemphys.2017.05.035>.
- [111] O. Isabella, S. Dobrovolskiy, G. Kroon, M. Zeman, Design and application of dielectric distributed Bragg back reflector in thin-film silicon solar cells, in: *J. Non. Cryst. Solids, Journal of Non-Crystalline Solids*, 2012: pp. 2295–2298. <https://doi.org/10.1016/j.jnoncrysol.2011.11.025>.

Vilniaus universiteto leidykla
Saulėtekio al. 9, III rūmai, LT-10222 Vilnius
El. p. info@leidykla.vu.lt, www.leidykla.vu.lt
bookshop.vu.lt, journals.vu.lt
Tiražas 16 egz.